

AD _____

Award Number: W81XWH-FEFE Î Î

TITLE: Úæç ^!•@ Á!æ ð * Á! [*!æ KÛc â^ ð * Áæ^c âÄ! ~ * Ä^|æ^ Áæ ð * Ä
Pæ [] ææ/^•Ä Ä!^æ Äæ &! Äæ } [• ä Äæ äÄ@!æ ^ Ä

PRINCIPAL INVESTIGATOR: T! Äæ | Ä æ *

CONTRACTING ORGANIZATION: P[, æâÄæ æ^!•æ
Y æ @ * ç } ÄÖÄÄGEÍ JÁ

REPORT DATE: U&ç à^! ÄFF

TYPE OF REPORT: Annual Û~ { { æ^

PREPARED FOR: U.S. Army Medical Research and Materiel Command
Fort Detrick, Maryland 21702-5012

DISTRIBUTION STATEMENT: Approved for public release; distribution unlimited

The views, opinions and/or findings contained in this report are those of the author(s) and should not be construed as an official Department of the Army position, policy or decision unless so designated by other documentation.

REPORT DOCUMENTATION PAGE				Form Approved OMB No. 0704-0188	
Public reporting burden for this collection of information is estimated to average 1 hour per response, including the time for reviewing instructions, searching existing data sources, gathering and maintaining the data needed, and completing and reviewing this collection of information. Send comments regarding this burden estimate or any other aspect of this collection of information, including suggestions for reducing this burden to Department of Defense, Washington Headquarters Services, Directorate for Information Operations and Reports (0704-0188), 1215 Jefferson Davis Highway, Suite 1204, Arlington, VA 22202-4302. Respondents should be aware that notwithstanding any other provision of law, no person shall be subject to any penalty for failing to comply with a collection of information if it does not display a currently valid OMB control number. PLEASE DO NOT RETURN YOUR FORM TO THE ABOVE ADDRESS.					
1. REPORT DATE (DD-MM-YYYY) 01-10-2011		2. REPORT TYPE Annual Summary		3. DATES COVERED (From - To) 15 Sep 2010 - 14 Sep 2011	
4. TITLE AND SUBTITLE A Partnership Training Program: Studying Targeted Drug Delivery Using Nanoparticles In Breast Cancer Diagnosis and Therapy				5a. CONTRACT NUMBER	
				5b. GRANT NUMBER W81XWH-10-1-0767	
				5c. PROGRAM ELEMENT NUMBER	
6. AUTHOR(S) Mr. Paul Wang E-Mail: pwang@howard.edu				5d. PROJECT NUMBER	
				5e. TASK NUMBER	
				5f. WORK UNIT NUMBER	
7. PERFORMING ORGANIZATION NAME(S) AND ADDRESS(ES) Howard University Washington, DC 20059				8. PERFORMING ORGANIZATION REPORT NUMBER	
9. SPONSORING / MONITORING AGENCY NAME(S) AND ADDRESS(ES) U.S. Army Medical Research and Materiel Command Fort Detrick, Maryland 21702-5012				10. SPONSOR/MONITOR'S ACRONYM(S)	
				11. SPONSOR/MONITOR'S REPORT NUMBER(S)	
12. DISTRIBUTION / AVAILABILITY STATEMENT Approved for Public Release; Distribution Unlimited					
13. SUPPLEMENTARY NOTES					
14. ABSTRACT In the first year of this training grant, 10 faculty members, and 7 graduate and 1 undergraduate students from 6 departments at the Howard University have been trained using nanoparticles as targeted drug delivery vehicles for cancer diagnosis and therapy. A total of 16 seminars and webinars, plus 6 workshops and symposia in cancer, molecular imaging and nanomedicine have been offered. The trainees have also received hands-on training in imaging and analytical instrumentations. The two research projects have started and progressed well. We have constructed and characterized cationic liposomes encapsulated MRI contrast agents for improving the sensitivity and specificity of breast cancer imaging. We studied the stability of nanoparticles in light of potential toxicity of nanoparticles used in humans. We have also used A-dmDT(390)-scfDb(PSMA), a single chain Fv fragments of antibody with diphtheria toxin, to demonstrate that a nano sized immunotoxin can be used for targeted delivery of toxin to the cancer cells and also can be used as an imaging reporter. The Howard University Nanomedicine Core was established and it has supported 10 research projects. The Nanomedicine Core has become a synergy center drawing multidisciplinary research collaborations using nanotechnology for targeted drug delivery and improving breast cancer diagnosis and therapy.					
15. SUBJECT TERMS training, nanotechnology, breast cancer, diagnosis, therapy, imaging, drug delivery					
16. SECURITY CLASSIFICATION OF:			17. LIMITATION OF ABSTRACT UU	18. NUMBER OF PAGES 87	19a. NAME OF RESPONSIBLE PERSON USAMRMC
a. REPORT U	b. ABSTRACT U	c. THIS PAGE U			19b. TELEPHONE NUMBER (include area code)

Á

DUTY

(

(

%&

%

%

%*

%

A Partnership Training Program – Studying Targeted Drug Delivery Nanoparticles in Breast Cancer Diagnosis and Therapy

I. INTRODUCTION

In this proposed training program a partnership between Howard University and the Johns Hopkins University In Vivo Cellular Molecular Imaging Center, with support from the Nanobiology Program and the Nanotechnology Characterization Laboratory at NCI-Frederick, will be established to pursue molecular imaging of breast cancer using nanoparticles for targeted drug delivery. At Howard University, this partnership will involve a multidisciplinary consortium of four departments: Radiology, Radiation Oncology, Molecular Biology and Biochemistry, and Electrical Engineering. The program has two components: a research component and a broad training component. Six Howard University faculty members will obtain training through collaborative research and by participating in a broad based training program. Internationally renowned experts in nanomedicine and molecular imaging from Johns Hopkins and NCI will participate in training through mentoring research, seminars, workshops, and by offering laboratory internships. This transfer of nanomedicine techniques will support ongoing, long-term breast cancer research at Howard University. The goal of this training program is to provide faculty trainees at Howard with updated nanomedicine techniques to apply to independent breast cancer research, enhancing their ability to educate the next generation of scientists. The program objectives are:

1. Á Train new researchers in breast cancer using modern nanomedicine techniques.
2. Á Offer lectures, seminars, workshops, and lab internships in nanotechnology and molecular imaging.
3. Á Conduct two proposed research projects.
4. Á Establish a Nanomedicine Core to support long-term sustainable research.
5. Á Research concept development and submission of competitive grants in breast cancer imaging.

II. BODY

Molecular imaging and functional MRI have provided new insights into the etiology, diagnosis, and treatment of breast cancer. Clinically, these methods have made a significant impact in breast cancer diagnosis and in monitoring response to therapy. As our understanding of breast cancer advances, we further recognize the complexities of this disease and the urgent need for individualized characterization and treatment. Recent exciting advances in the application of MR methods for breast cancer research have resulted from the development of contrast agents (CAs) that generate receptor-targeted or molecular targeted contrast. Targeted CAs can be directed to cell surface receptors using antibodies [1, 2], or ‘smart’ agents activated by specific enzymes, or based on the expression of detectable reporters [3, 4]. These molecular imaging capabilities, in combination with the strong functional imaging capabilities of MR methods, allow molecular–functional characterization of cancer and the physiological microenvironment of tumors [5]. Non-invasive MR can play an important role in the molecular–functional characterization of breast cancer for detection, drug delivery, development of therapeutics, and monitoring of treatment response. Lately, the development of nanotechnology has

shown a dramatic impact on diagnosis and treatment [6-8]. Among many possible applications of nanotechnology in medicine, the use of various nanomaterials as pharmaceutical delivery systems for drugs, DNA, and imaging agents has gained increasing attention. Many nanoparticle-based drug delivery and drug targeting systems have been developed for FDA approval or are under development [9-11]. The primary goals of utilizing nanoparticles for drug delivery are to minimize drug degradation, prevent undesirable side effects, and increase drug bioavailability and the fraction of drug dosage delivered to the pathological area.

In order to achieve the goals of this training program, we proposed to conduct two research projects and a broad-based training program to train researchers at Howard University in the field of application of nanotechnology in targeted drug delivery. In addition, we also proposed to establish a University Nanomedicine Core to promote and facilitate campus-wide research and training activities. The following progress report is a summary of the accomplishments for the first year in the areas: (i) research (ii) training (iii) establishment of Nanomedicine Core and (iv) alignment with the Statement-of-work.

II.1 Research

Project 1: Study the physicochemical characteristics of nanoparticles as MR contrast agent delivery system with the dynamic contrast enhancement pattern for clinical applications

Nanoparticles (NP) of different sizes, shapes and material properties have many applications in biomedical imaging, clinical diagnostics and therapeutics [12-17]. The commonly used nanoparticles include liposome (Lip), micelles; quantum dots (QDs), polymeric, gold, and magnetic nanoparticles. The unique physical and chemical properties of each nanoparticle significantly influence its interactions with tissues and cells. By varying the size, shape and material properties of engineered nanoparticles, their distribution, pharmacokinetics, the degree of binding and internalization in tissues can be precisely controlled. Having a better understanding of the interactions of nanoparticles with biological systems will greatly assist in designing smart drugs and targeted drug delivery systems with potential for much improved molecular-based diagnosis and therapy.

In this study, we have constructed liposomal nanoparticles with MR contrast agents (CAs), Magnevist (Mag), as payloads, transferrin (Tf) coupled to the liposome (Lip) surface as ligand for targeted delivery of CAs to breast cancer cells and xenograft tumors. This year we were devoted to perfecting liposome preparation, characterization, and optimization. We have been modified a previously described [18] method in order to have better control of the size of the nanoparticles. The size of NPs was controlled by sonication and further polycarbonate filtration. The Tf binding to the liposomes surface was verified by size measurements before and after conjugation. A typical result of size measurement of this nanoparticle complex is shown in Figure 1. As an example, the sizes of Lip-Mag and Tf-Lip-Mag were 111 nm and 122nm with full-width-half-maximum of 56 nm and 44 nm respectively. Since the dimension of transferrin is approximately 8×10 nm. This size measurement confirms the successful binding of Tf to the liposome surface. The properties of nanoparticles, such as size

distribution measured by light scattering and the surface charge measured by zeta potential, were characterized using a Malvern Zetasizer S90. The encapsulation efficiency, lipid concentration and Tf linkage on the surface will be measured by mass spectrometry and colorimetry. These physicochemical properties will be used to correlate the effectiveness of specific targeting of the nanoparticles in cells and tumors in live animals.

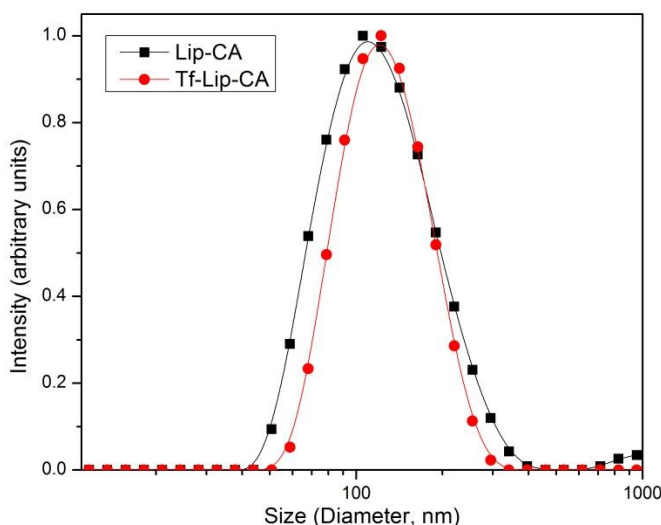


Figure 1. Liposome size measurement. Increase of the size as an indication for attachment of Tf.

We have also developed transferrin attached protein nanospheres with silicon coating, doped with rare earth oxide and rhodamine B isothiocyanate, optimized for enhancing MRI, CT and US contrast while also providing high sensitivity optical detection. No single clinical imaging modality has the ability to provide both high resolution and high sensitivity at the anatomical, functional and molecular level. Synergistically integrated detection techniques overcome these barriers by combining the advantages of different imaging modalities while reducing their disadvantages. The preliminary results indicate our transferrin protein nanosphere has an improved sensitivity of detection for MRI, CT, US and fluorescence imaging relative to its component parts and many commercially available contrast agents. This work has been presented in the 2011 SPIE meeting and a paper was published in the Proceedings of SPIE (attached in the Appendix).

One of the important physicochemical properties of the nanoparticle is its stability. For the nanoparticle to be used in the clinic, it is not only required to survive in harsh physiological conditions and to avoid being recognized by mononuclear phagocyte system, but also to be stable enough to maintain the integrity of the ligand for specific targeting. If the nanoparticle disintegrates inside the body before reaching the intended target, it may cause safety concerns. In this year, we have studied the stability of nanoparticle and developed a NMR spectroscopy method to monitor the integrity of the nanoparticle in the body. We have constructed QDs coated with TOPO for the stability study. We have demonstrated that this commonly used TOPO coating is not stable under physiological conditions, causing the release of toxic cadmium ions in the body. For improvement, we have used a novel triblock copolymer coating to reduce the potential toxicity of QDs. The detailed experimental procedures and

results were published in a paper in the Colloid and Surfaces A: Physicochem. Eng. Aspects (attached in Appendix).

Project 2: Development of multifunctional nanoparticles for breast cancer diagnosis and treatment – Using anti-VEGFR-2 immunotoxin as dual purpose ligand and chemotherapeutics as encapsulated payload

Angiogenesis is fundamental to sustain the growth, invasion and metastasis of tumors [19, 20]. Vascular endothelial growth factors (VEGF) receptors are the primary and most potent inducers of tumor angiogenesis [21, 22]. Activation of the VEGF signal pathway promotes endothelial cell survival, proliferation, migration and vascular permeability. VEGFR-2 appears to mediate almost all of the known cellular responses to VEGF and is a critical target for tumor suppression [20-23]. Immunotoxins are plant or bacterial toxins coupled or fused with monoclonal antibodies (mAbs), single-chain Fv (scFv) fragments or growth factors. The goal of immunotoxin development has been to achieve targeted cell killing, but maintain the low non-target cell toxicity of toxin A chains. In this research project we plan to (1) define the efficacy of anti-VEGFR-2 immunotoxin in animal models of breast cancer; (2) evaluate toxicity and maximum tolerated dose of anti-VEGFR-2 immunotoxin in healthy mice as well as in mice with tumor xenografts; (3) define biodistribution and pharmacokinetics of anti-VEGFR-2 immunotoxin.

In the first year we have collaborated with Dr. Liu and Dr. Neville from NIH to conduct a proof-of-principle study using their well-established fold-back of two single chain Fv fragments of anti-PSMA monoclonal antibody with the catalytic and translocation domains of diphtheria toxin A-dmDT(390)-scfbDb(PSMA) to study the tumor targeting and therapeutic potential of the immunotoxin. In this study, two types of prostate cancer, a PSMA positive and a PSMA negative cancers, were treated with A-dmDT(390)-scfbDb(PSMA). Cellular uptake and selective toxicity of A-dmDT(390)-scfbDb(PSMA) was evident in monolayer cultures of PSMA-positive LNCap prostate cancer cells but not in cultures of PSMA-negative PC-3 prostate cancer cells. Cellular accumulation of A-dmDT(390)-scfbDb(PSMA) increased with increasing incubation time or concentration in LNCaP cells and an increase in the proportion of apoptotic LNCaP cells occurred with increasing dose of the fold-back immunotoxin. A-dmDT(390)-scfbDb(PSMA) labeled with Alexa 680 was utilized in conjunction with MRI and optical imaging in vivo to demonstrate the specific targeting (Figure 2) and therapeutic efficacy (Figure 3) towards PSMA positive LNCaP solid tumor xenografts in athymic nude mice. A draft manuscript of this study for publication is attached in the Appendix.

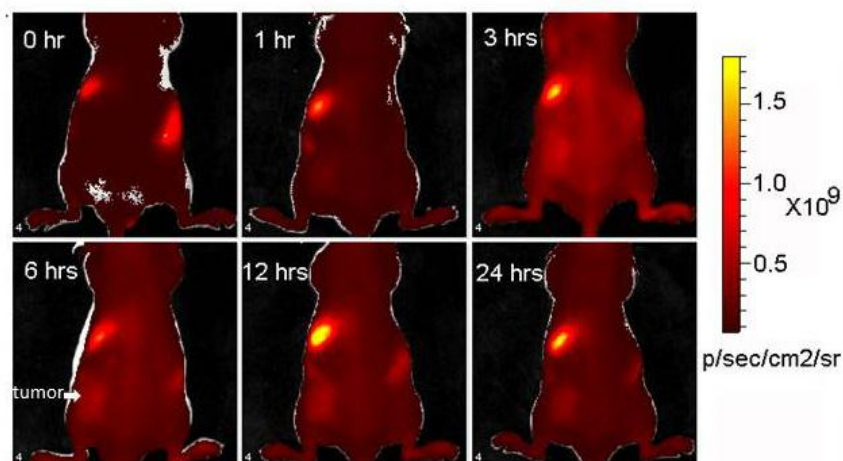


Figure 2. Live animal imaging following intravenous injection of Alexa Fluor 680 -labeled A-dmDT90(390)-scfbDb(PSMA) into LNCaP tumor bearing mice showing preferential accumulation of fluorescent signals in tumors (on left leg). Images were taken at 0, 1, 3, 6, 12 and 24 hours, separately.

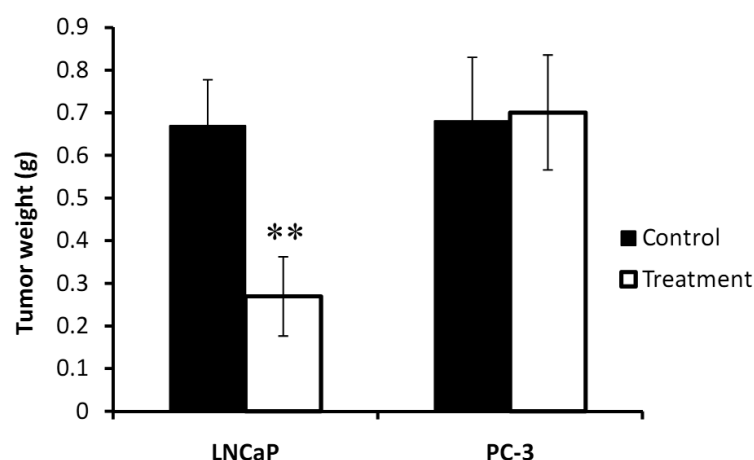


Figure3. Effect of A-dmDT90(390)-scfbDb(PSMA) immunotoxin on LNCaP and PC-3 carcinomas. 5 μg per dose of A-dmDT90(390)-scfbDb(PSMA) immunotoxin was given via i.p. injection, two doses a day with 6 hour interval for 6 days, compared to equivalent dose of BSA diluted in DPBS as control.

II.2 Training

The Molecular Imaging Lab has regular group meetings, journal club, and seminars. Bi-weekly group meetings provide opportunities to discuss the experimental issues of the research, review progress, and exchange ideas, and have been the primary mode of interaction between Howard researchers and collaborating experts. The faculty trainees have also attended special workshops on molecular imaging and imaging instrumentation. All the users of the Nanomedicine Core had hands-on training in using optical imaging, MRI and Zetasizer instruments. Through participation in the Imaging Core sponsored seminars, workshops and interactions with Imaging Core staff, we expect that significant common synergies of interests will be identified, and that much multidisciplinary research collaboration will be developed. Dr. Alexandru Korotcov has been working with Dr. Dmitri Artemov at Johns Hopkins University for developing MRI diffusion contrast enhancement techniques to be used in the in vivo study of the proposed research

project 1. The PI and the partnership leader at Johns Hopkins have been coordinating the training efforts through meetings and emails. The seminars and workshops organized/ or attended at Howard University, as well as at the Johns Hopkins University and other institutions, are listed as following:

Seminars and workshops

1. Á Synthesis and Evaluation of Novel RGD peptide conjugates for Tumor Optical Imaging. Yunpeng Ye, PhD. September 29, 2010, Molecular Imaging Laboratory, Howard University Hospital Cancer Center.
2. Á Computational Biology & Bioinformatics, Biomedical Imaging and Proteomics. Drs. Paul C. Wang, William M. Southerland, Sergei Nekhai. RCMI. November 16, 2010, Howard University Symposium.
3. Á Imaging of Breast Cancer Metastasis Suppression by Naringenin. Fayun Zhang, PhD. December 17, 2010, Molecular Imaging Laboratory, Howard University Hospital Cancer Center.
4. Á Anti-PSMA bivalent single-chain Fv fold-back format immunotoxin for prostate cancer imaging and therapy. Fayun Zhang, PhD. January 14, 2011, Molecular Imaging Laboratory, Howard University Hospital Cancer Center.
5. Á Use of MRI/MRS to assess white matter development including injury, recovery, and maturation of white matter: DTI and Spectroscopy Analysis. Alexandru V. Korotcov, PhD. February 9, 2011. Molecular Imaging Laboratory, Howard University Hospital Cancer Center.
6. Á Formula for Grant Success. Anthony M. Coelho, Jr, PhD. February 22, 2011, Howard University Louis Stokes Library.
7. Á Integrin $\alpha\beta 3$ -targeted Optical Imaging of Cancer by NIR Fluorescent cyclic RGD Peptides. Yunpeng Ye, PhD. March 29, 2011, Molecular Imaging Laboratory, Howard University Hospital Cancer Center.
8. Á Seminar: Synthesis or novel Quantum Dots for biomedical applications. Chung-Shieh Wu, Ph.D. May 25, 2011, Howard University Hospital Cancer Center.
9. Á Manuscript Review. Thomas Heinbockel, PhD and Edward Cornwell III, MD. June 16, 2011, Howard University Blackburn Center.
10. Á Discovering Disease Mechanisms: Advancing Imaging in the Cell. Produced by the Science/AAAS and sponsored by PerkinElmer, June 28, 2011, webner broadcasted in the Molecular Imaging Laboratory, Howard University Hospital Cancer Center.
11. Á New Signal-to-Noise Horizons in Preclinical and Molecular MRI – The MRI CryoProbe. Mat Brevard, PhD, Bruker BioSpin. June 28, 2011, Webner broadcasted in the Molecular Imaging Laboratory, Howard University Hospital Cancer Center.
12. Á Super Resolution Microscopy: key tools and processes. Produced by BioOptics World. webcast and sponsored by Carl Zeiss Microimaging and Mad City Labs. July 13, 2011, broadcasted in the Molecular Imaging Laboratory, Howard University Hospital Cancer Center.
13. Á An Vivo Optical Imaging Probe Developments. Rajendra Singh, Ph.D, Director, Biology R&D, Caliper Life Sciences. July 21, 2011, Webner broadcasted in the Molecular Imaging Laboratory, Howard University Hospital Cancer Center.
14. Á Antroduction to Magnetic Resonance Imaging and Spectroscopy (theory and hands-on training). Alexandru V. Korotcov, PhD and Stephen Lin, M.Eng. July 25 - 26, 2011, Molecular Imaging Laboratory, Howard University Hospital Cancer Center.
15. Á Principles and Applications of Multiphoton Imaging. Drs. Simon C. Watkins, Tomasz Zal, and Janos Peti-Peterdi. Sponsored by Leica Microsystem. July 27, 2011, Webner broadcasted in the Molecular Imaging Laboratory, Howard University Hospital Cancer Center.
16. Á Light Scattering Technology: Theory and Applications Workshop. Physicochemical characterization of nanoparticles (theory and hands-on training). Stephen Kelly, Product Specialist, Malvern Instruments Inc. September 13, 2011, Howard University Hospital Cancer Center.

Seminars and workshops at John Hopkins University and other institutions

1. Á Combating Lung Cancer: Newer Targets and Delivery Systems. Mandip Singh Sachdeva, PhD. October 4, 2010, National Cancer Institute, Frederick, MD.
2. Á Molecular Imaging of the Tumor Microenvironment with PET and Bioluminescence Imaging. Carolyn Anderson, PhD November 10, 2010, Dept. of Radiology, John Hopkins University, Baltimore, MD.
3. Á Visualizing the Tumor Vasculature: Applications to Phenotyping, Systems Biology and Biomarkers. Arvind Pathak, PhD. March 16, 2011, Dept. of Radiology, John Hopkins University, Baltimore, MD.
4. Á Localized Hypoxia Results in Spatially Heterogeneous Metabolic Signatures in Breast Tumor Models. Lu Jiang, PhD. April 20, 2011, Dept. of Radiology, John Hopkins University, Baltimore, MD.
5. Á Multi-scale molecular imaging of the degradome in breast tumors. Kristine Glunde, PhD. May 4, 2011, Dept. of Radiology, John Hopkins University, Baltimore, MD.
6. Á 6th Annual Cancer Nanobiology Think Tank. Symposium. Organizers: Drs. Robert Blumenthal and Anu Puri. May 17, 2011, National Cancer Institute, Frederick, MD.
7. Á From Molecular Imaging to DCE-MRI: New Ideas and Developments. Dmitri Artemov, Ph.D. June 1, 2011, Dept. of Radiology, John Hopkins University, Baltimore, MD.
8. Á Translational MRI and MRS Methods to Study the Tumor and its Environment. Harish Poptani, PhD. August 31, 2011, Dept. of Radiology, John Hopkins University, Baltimore, MD.

II.3 Establish a Nanomedicine Core

In the first year of the proposed training program, we have established the Nanomedicine Core. The core draws proficiency from the Howard University Nanoscience Facility and Molecular Imaging Laboratory to offer state-of-art instrumentation and technical support in nanotechnology for the researchers. We have purchased a new nanoparticle analyzer, a Malvern Zetasizer Nano S90. The Zetasizer Nano S90 provides the ability to measure particle size, zeta potential and molecular weight of particles or molecules in a liquid medium. The Zetasizer is housed in the Molecular Biology Lab convenient for constructing nanoparticles as molecular probes. The Zetasizer is also located close to the existing Optical Imaging and MRI/MRS instruments for in vivo and in vitro imaging studies. Through the consortium of the Nanomedicine Core and other core facilities on campus, researchers who are conducting nanomedicine research can also have access to analytical and imaging instrumentation such as electron microscope, confocal microscope, mass spectrometer and other instruments. The Nanomedicine Core has established collaboration with Dr. Michael McDonald at the NIST Nanotechnology program, which is part of the NCI Nanotechnology Characterization Lab consortium. Since the initiation, 10 research projects (see Appendix) have been supported by the Nanomedicine Core including projects in the initial phase of research. One of the crucial missions of the Nanomedicine Core is to support projects lacking funding and help obtain preliminary data for successful grant applications. There are 10 faculty members from 6 departments and 3 scientists from the neighboring institutions including NIST, NIH and Georgetown University using the core facility to conduct these research projects. There are 7 graduate students, one undergraduate, and one postdoctoral fellow working with principle investigators in these projects. The Nanomedicine Core has brought together Howard faculty researchers and their students who share common interests in using nanotechnology for drug delivery to improve breast cancer diagnosis and therapy.

II.4 Statement of Work Summary

The accomplishments aligned with the Statement-of-Work occurred in this reporting period is listed as following:

Research Component

- Task 1. To conduct Research Project 1 “Study the physicochemical characteristics of nanoparticles as MR contrast agent delivery system with the dynamic contrast enhancement pattern for clinical applications” (months 1-48).
- a. Purchase supplies for cell culture and materials for nanoparticles (months 1-2) (*completed*)
 - b. Construct liposome (Lip) nanoparticles with transferrin (Tf) as the ligand and encapsulated Gd-based MRI contrast agent (CA) inside as payload (months 3-9) (*completed*)
 - c. Characterize the physicochemical properties of nanoparticles including size distribution, surface charge, encapsulation efficiency, and Tf linkage on the surface. Some of the measurements will be done at NCL, NCI-Frederick. (months 6-12) (*in progress*)
 - d. Study targeting efficiency of the liposome nanoparticle using MDA-MB-231 cells. Study the interactions of nanoparticles with breast cancer cells (months 13-24).
 - e. Study the correlation of the dynamic contrast enhancement (DCE) pattern with distribution of Tf-liposome nanoparticles in tumor xenografts. Both MR and optical imaging will be used (30 mice) (months 25-36).
 - f. Evaluate the potential clinical applications of the DCE pattern, focusing on relationship between the DCE pattern and the tumor features of TfR expression level, permeability of neovasculatures, vascular density, tumor growth and necrosis (months 25-40).
 - g. Data analysis and preparation of manuscripts for publication (months 40-48)
- Task 2. To conduct Research Project 2 “Develop multifunctional nanoparticles for breast cancer diagnosis and treatment – using anti-VEGFR-2 immunotoxin as dual purpose ligand and chemotherapeutics as encapsulated payload” (months 1-48).
- a. Purchase supplies and prepare for the study (months 1-2) (*completed*)
 - b. Define the efficacy of the anti-murine anti-VEGFR-2 immunotoxin in endothelial cell killing and vascular permeability increase in animal models (months 3-18) (*in progress*)
 - c. Construct and characterize the targeted anti-VEGFR-2 immunotoxin multifunctional nanoparticles. Some of the work will be done at NCL (months 13-18).
 - d. Determine the biodistribution, pharmacokinetics and toxicity of the nanoparticles in healthy mice (8) and mice (22) bearing with tumor xenografts. Optical imaging will be used. Measurements of biodistribution will be done at NCL and HNF (months 19-40).
 - e. Define the synergistic effects by combined targeted delivery, anti-angiogenics and chemotherapeutics in animal models of breast cancer. Histological staining will be used to study the tumor vasculature (months 25-40).
 - f. Data analysis and preparation of manuscripts for publication (months 40-48).
- Task 3. Research concept development and submission of competitive grants in breast cancer targeted imaging and therapy (months 37-48).

Broad Training Component

- Task 4. Provide opportunities to the faculty trainees in Howard University for updated knowledge of nanomedicine (months 1-48) (*in progress for all tasks*)
- a. Biweekly group meetings at the Molecular Imaging Lab (months 1-48)
 - b. Monthly Seminar series at Howard University Cancer Center to be presented by the mentors and invited speakers (months 1-48).

- c. Johns Hopkins University ICMIC Seminar Series organized by Dr. Bhujwalla (months 1-48).
 - d. To attend the biweekly Nanobiology Program Seminar Series at NCI-Frederick organized by Dr. Blumenthal (months 1-48).
 - e. Annual scientific meetings with mentors and trainees.
- Task 5. Train Howard faculty in advanced nanomedicine lab techniques (*in progress for all tasks*)
- a. Laboratory internships at the Johns Hopkins University and NCL, topics include molecular imaging and nano characterization techniques, 2-4 days each (months 1-36).
 - b. Workshop series. Topics include MR and optical imaging, SEM/TEM/AFM, optical instrumentation, drug design and liposome. (months 1-48).
- Task 6. Administrative and communication affairs (coordinated by Drs. Wang and Bhujwalla) (Months 1-48) (*in progress for all tasks*)
- a. Status reports (quarterly and annual reports)
 - b. Research progress review (quarterly)
 - c. Administrative meetings (biannually meetings)
 - d. Coordination of seminars, workshops, and laboratory internships

III. KEY RESEARCH ACCOMPLISHMENTS

- Á Liposome nanoparticles of variable sizes were constructed. The liposomes were linked with transferrin as breast cancer cell targeting moiety on the surface. A Gd based MR contrast agent, Magnevist, was encapsulated inside the liposome for *in vitro* and *in vivo* imaging studies.
- Á The physicochemical properties of liposomal nanoparticles including size distribution, surface charges were characterized. The transferrin binding was confirmed by changes of particle size before and after conjugation.
- Á Transferrin protein nanospheres, silicon coated, doped rare earth oxide and rhodamine B isothiocyanate were constructed for enhancing MRI, CT and US contrast to provide both high resolution and high sensitivity of imaging at anatomical, functional and molecular level.
- Á To study the potential toxicity of nanoparticles, QDs coated with TOPO were constructed for breast cancer diagnosis. We have shown this commonly used TOPO coating is not stable under physiological conditions. It causes release of toxic cadmium ions in the body. For improvement, we have used a novel triblock copolymer for coating to reduce the potential toxicity of QDs.
- Á A fold-back of two single chain Fv fragments of anti-PSMA monoclonal antibody with diphtheria toxin (A-dmDT(390)-scfbDb(PSMA) has demonstrated the specific targeting and therapeutic efficacy towards PSMA positive LNCaP cells and solid tumor xenografts in mice.
- Á Bacterial magnetosomes synthesized by magnetotactic bacteria have recently been demonstrated as superior targeting nanoscale carriers for delivering antibodies, enzymes, nucleic acids, and chemotherapeutic drugs. We did a thorough literature review of the loading methods, strategies, and potential applications of the bacterial magnetosome as drug carrier.

IV. REPORTABLE OUTCOMES

Publications

1. Á Wang TX, Sridhar R, Korotcov A, Ting AH, Francis K, Mitchell J, Wang PC. Synthesis of amphiphilic triblock copolymers as multidentate ligands for biocompatible coating of quantum dots. *Colloid and Surfaces A: Physicochem. Eng. Aspects*, 375(1-3)147-155, 2011.
2. Á McDonald MA, Wang PC, Siegel EL. Protein Nanospheres: Synergistic Nanoplatform-Based Probes for Multimodality Imaging. *Proc. of SPIE Vol. 7910*, 79101G1-14, 2011.
3. Á Sun JB, Li Y, Liang XJ, Wang PC. Bacterial Magnetosome: A Novel Biogenetic Magnetic Targeted Drug Carrier with Potential Multifunctions. *Journal of Nanomaterials*. Vol 2011, Article ID 469031. doi:10.1155/2011/469031.

Presentations

1. Á Korotcov AV, Ye Y, Chen Y, Zhang F, Huang S, Sridhar R, Achilefu S, Wang PC. Tumor Optical Imaging of Glucosamine Linked Fluorescent Probes in Mice. *RCMI 12th International Symposium on Health Disparities*, Nashville, TN, December 6-9, 2010.
2. Á Korotcov AV, Wang T, Chen Y, Sridhar R, Mitchell J, Wang PC. 31P NMR Study of the Interaction of TOPO-QDs with Mercaptoethanol. *RCMI 12th International Symposium on Health Disparities*. Nashville, TN, December 6-9, 2010.
3. Á Ye YP, Zhu L, Xu B, Wang PC, Achilefu S, Chen XY. Integrin targeting and tumor imaging: comparison of two RGD peptides. *RCMI 12th International Symposium on Health Disparities*, Nashville, TN, December 6-9, 2010.
4. Á Korotcov AV, Wang T, Chen Y, Sridhar R, Mitchell J, Wang PC. 31P NMR Study of Thiol Mediated Degradation of TOPO-Quantum Dots. *Howard University College of Medicine Research Day 2010*, Howard University, Washington, DC, April 15 2011.
5. Á Wang PC, Wang TX, Korotcov AV, Chen Y, Sridhar R, Mitchell JW. Monitoring Thiol-Mediated Degradation of TOPO-Quantum Dots by 31P Nuclear Magnetic Resonance Spectroscopy. *Proceedings of Era of Hope 2011*, Orlando, FL, August 2-5, 2011.
6. Á Wang PC, Liang XJ. Applications of Nanoparticles for In Vivo Imaging. *International Conference on Nanoscience & Technology, ChinaNANO 2011*, Beijing, China, September 7-9, 2011.
7. Á Korotcov AV, Wang TX, Chen Y, Sridhar R, Mitchell J, Wang PC. Study of TOPO-Quantum Dot Degradation by 31P NMR. *2011 World Molecular Imaging Congress*, San Diego, CA, September 7-10, 2011.

Grants

1. Á NIH M01RR010284-15 GHUCCTS 04/01/2011-03/31/2013 Verbalis J (Program PI), Mellman T (co-PI) Osteopontin Genotype As A Determinant Of Muscle Remodeling: A Study of African-American Young Adult Volunteers. This is a pilot project supported by Georgetown-Howard Universities Center for

Clinical and Translational Science grant to conduct MR imaging study. Bond V. (PI), Paul Wang (co-PI) (funded)

2. Á NIH/NCI R21 09/01/2011-08/31/2013

Novel Multifunctional Zinc- and Integrin-binding Agents for Theranostics of Prostate Cancer
Ye Y. (PI) (not funded)

3. Á NIH/U54 09/01/2011- 08/31/2013 Smoot (program PI), Nelson (PI)

Targeting Pancreatic Cancer Stem Cells with Integrin Binding Nanoparticles.

Ye Y. (PI), Matsui W. (co-PI) (not funded)

4. Á RTRN/RCMI/DTCC 07/01/2011-06/30/2012

Novel Integrin-targeted Zinc-binding Nanoparticles for Theranostics of Prostate Cancer.

Ye Y (PI), Wang PC (co-PI) (not funded)

5. Á NIH R21 07/01/2012-06/30/2014

Enhancing the simultaneous inhibition of integrin $\alpha v \beta 3$ and mTOR for treatment of pancreatic cancer stem cells. Ye Y (PI) (pending)

6. Á NIH/SCORE 07/01/2012-06/30/2015

Design of Multifunctional Polymeric Nanoparticles for Breast Cancer Diagnosis and Treatment.

Akala E (PI) (pending)

V. CONCLUSIONS

In the first year of this training grant, faculty members, and graduate and undergraduate students from different departments at the Howard University have been trained using nanoparticles as targeted drug delivery vehicles for cancer diagnosis and therapy. A total of 16 seminars and webinars, plus 6 workshops and symposia in cancer, molecular imaging and nanomedicine have been offered. The trainees have also received hands-on training in imaging and Zetasizer instruments. Howard faculty trainees attended the 6th Annual Cancer Nanobiology Think Tank Workshop sponsored by the NCI, and various seminars at the Johns Hopkins University. The bi-weekly group meetings, a primary mode of interaction among the Howard researchers and collaborating experts, have provided opportunities to discuss the progress of research and brainstorm new ideas.

The two research projects started and progressed well. We have constructed and characterized cationic liposomes encapsulated MRI contrast agents for improving the sensitivity and specificity of MRI breast cancer imaging. In addition, the targeted delivery of MR contrast agents can potentially reduce the amount of Gd required to achieve high MR image contrast, which in turn will reduce the toxicity of the Gd particularly to the renal deficient patients. We studied the stability of nanoparticles in light of potential toxicity of nanoparticles used in humans. We have established a noninvasive method to monitor the dissociation of commonly used surfactant TOPO from quantum dots. We will use this method to test the stability of nanoparticles under harsh physiological conditions in live animals. We have also used A-dmDT(390)-scfDb(PSMA), a single chain Fv fragments of antibody with diphtheria toxin, to demonstrate that a nano sized immunotoxin can be used for targeted delivery of toxin to the cancer cells and at the same time it can be used as an imaging reporter of the cancer targeting efficiency. This immunotoxin has dual functions both as an imaging and as a therapeutic agent.

In this year, we have established the Howard University Nanomedicine Core. We have purchased a new nanoparticle analyzer - Zetasizer Nano S90 used for constructing nanoparticles as molecular probes.

Through the consortium of the Nanomedicine Core and other core facilities on campus, researchers who are conducting nanomedicine research can also have access to analytical and imaging instrumentation. Since the establishment, 10 research projects have been supported by the Nanomedicine Core. There are 10 faculty members from 6 departments and 3 scientists from the neighboring institutions including NIST, NIH and Georgetown University have used the core facilities. There are 7 graduate students, one undergraduate, and one postdoctoral fellow working with principle investigators in these projects. The Nanomedicine Core has become a synergy center drawing multidisciplinary research collaborations using nanotechnology for targeted drug delivery and improving breast cancer diagnosis and therapy.

VI. References

1. Artemov D, Mori N, Okolie B, Bhujwalla ZM. MR molecular imaging of the Her-2/neu receptor in breast cancer cells using targeted iron oxide nanoparticles. *Magnetic Resonance in Medicine* 49 (3): 403-408, 2003.
2. Artemov D, Bhujwalla ZM, Bulte JW. Magnetic Resonance Imaging of Cell Surface Receptors Using Targeted Contrast Agents *Current Pharmaceutical Biotechnology* 5 (6): 485-494, 2004.
3. Cohen B, Dafni H, Meir G, Harmelin A, Neeman M. Ferritin as an Endogenous MRI Reporter for Noninvasive Imaging of Gene Expression in C6 Glioma Tumors. *Neoplasia* 7 (2): 109-117, 2005.
4. Cohen B, Ziv K, Plaks V, Israely T, Kalchenko V, Harmelin A, Benjamin LE, Neeman M. MRI detection of transcriptional regulation of gene expression in transgenic mice. *Nat Med* 13 (4): 498-503, 2007.
5. Gillies RJ, Raghunand N, Karczmar GS, Bhujwalla ZM. MRI of the tumor microenvironment. *Journal of Magnetic Resonance Imaging* 16 (4): 430-450, 2002.
6. Ferrari M. Cancer nanotechnology: opportunities and challenges. *Nat Rev Cancer* 5 (3): 161-171, 2005.
7. Riehemann K, Schneider SW, Luger TA, Godin B, Ferrari M, Fuchs H. Nanomedicine - Challenge and Perspectives. *Angewandte Chemie International Edition* 48 (5): 872-897, 2009.
8. Sahoo SK, Parveen S, Panda JJ. The present and future of nanotechnology in human health care. *Nanomedicine: Nanotechnology, Biology and Medicine* 3 (1): 20-31, 2007.
9. Torchilin V. Targeted pharmaceutical nanocarriers for cancer therapy and imaging. *The AAPS Journal* 9 (2): E128-E147, 2007.
10. Faraji AH, Wipf P. Nanoparticles in cellular drug delivery. *Bioorganic & Medicinal Chemistry* 17(8): 2950-2962, 2009.
11. Gil PR, Parak WJ. Composite Nanoparticles Take Aim at Cancer. *ACS Nano* 2 (11): 2200-2205, 2008.
12. Xia Y, Yang P, Sun Y, Wu Y, Mayers B, Gates B, Yin Y, Kim F, Yan H. One-Dimensional Nanostructures: Synthesis, Characterization, and Applications. *Advanced Materials* 15 (5): 353-389, 2003.
13. Alivisatos AP. Semiconductor Clusters, Nanocrystals, and Quantum Dots. *Science* 271 (5251): 933-937, 1996.
14. Elghanian R, Storhoff JJ, Mucic RC, Letsinger RL, Mirkin CA. Selective Colorimetric Detection of Polynucleotides Based on the Distance-Dependent Optical Properties of Gold Nanoparticles. *Science* 277 (5329): 1078-1081, 1997.
15. Cao YC, Jin R, Mirkin CA. Nanoparticles with Raman Spectroscopic Fingerprints for DNA and RNA Detection. *Science* 297 (5586): 1536-1540, 2002.
16. Klostranec J M, Chan WCW. Quantum Dots in Biological and Biomedical Research: Recent Progress and Present Challenges. *Advanced Materials* 18 (15): 1953-1964, 2006.
17. Hirsch LR, Stafford RJ, Bankson JA, Sershen SR, Rivera B, Price RE, Hazle JD, Halas NJ, West JL. Nanoshell-mediated near-infrared thermal therapy of tumors under magnetic resonance guidance. *Proceedings of the National Academy of Sciences of the United States of America* 100 (23): 13549-13554, 2003.
18. Shan L, Wang S, Sridhar R, Bhujwalla ZM, Wang PC. Dual probe with fluorescent and magnetic properties for imaging solid tumor xenografts. *Molecular Imaging* 6 (2): 85-95, 2007.

19. Stefanini M, Wu F, Mac Gabhann F, Popel A. A compartment model of VEGF distribution in blood, healthy and diseased tissues. *BMC Systems Biology* 2 (1): 77, 2008.
20. Schenone S, Bondavalli F, Botta M. Antiangiogenic Agents: an Update on Small Molecule VEGFR Inhibitors. *Current Medicinal Chemistry* 14 (23): 2495-2516, 2007.
21. Kiselyov A, Balakin KV, Tkachenko SE. VEGF/VEGFR signalling as a target for inhibiting angiogenesis. *Expert Opinion on Investigational Drugs* 16 (1): 83-107, 2007.
22. Veeravagu A, Hsu AR, Cai W, Hou LC, Tse VCK, Chen X. Vascular Endothelial Growth Factor and Vascular Endothelial Growth Factor Receptor Inhibitors as Anti-Angiogenic Agents in Cancer Therapy. *Recent Patents on Anti-Cancer Drug Discovery* 2 (1): 59-71, 2007.
23. Lu D, Jimenez X, Zhang H, Wu Y, Bohlen P, Witte L, Zhu Z. Complete Inhibition of Vascular Endothelial Growth Factor (VEGF) Activities with a Bifunctional Diabody Directed against Both VEGF Kinase Receptors, fms-like Tyrosine Kinase Receptor and Kinase Insert Domain-containing Receptor. *Cancer Res* 61 (19): 7002-7008, 2001.

VII. APPENDICES (a list of)

1. Research Projects Supported by the Nanomedicine Core
2. Students Participated in Nanomedicine Core Supported Research Projects
3. Wang TX, Sridhar R, Korotcov A, Ting AH, Francis K, Mitchell J, Wang PC. Synthesis of amphiphilic triblock copolymers as multidentate ligands for biocompatible coating of quantum dots. *Colloid and Surfaces A: Physicochem. Eng. Aspects*, 375(1-3)147-155, 2011.
4. McDonald MA, Wang PC, Siegel EL. Protein Nanospheres: Synergistic Nanoplatfrom-Based Probes for Multimodality Imaging. *Proc. of SPIE Vol. 7910*, 79101G1-14, 2011.
5. Sun JB, Li Y, Liang XJ, Wang PC. Bacterial Magnetosome: A Novel Biogenetic Magnetic Targeted Drug Carrier with Potential Multifunctions. *Journal of Nanomaterials*. Vol 2011, Article ID 469031. doi:10.1155/2011/469031.
6. Korotcov AV, Ye Y, Chen Y, Zhang F, Huang S, Sridhar R, Achilefu S, Wang PC. Tumor Optical Imaging of Glucosamine Linked Fluorescent Probes in Mice. RCMI 12th International Symposium on Health Disparities, Nashville, TN, December 6-9, 2010, 03.01.26.
7. Korotcov AV, Wang T, Chen Y, Sridhar R, Mitchell J, Wang PC. ³¹P NMR Study of the Interaction of TOPO-QDs with Mercaptoethanol. RCMI 12th International Symposium on Health Disparities. Nashville, TN, December 6-9, 2010. 03.01.27
8. Ye YP, Zhu L, Xu B, Wang PC, Achilefu S, Chen XY. Integrin targeting and tumor imaging: comparison of two RGD peptides. RCMI 12th International Symposium on Health Disparities, Nashville, TN, December 6-9, 2010. 12.07.06
9. Korotcov AV, Wang T, Chen Y, Sridhar R, Mitchell J, Wang PC. ³¹P NMR Study of Thiol Mediated Degradation of TOPO-Quantum Dots. Howard University College of Medicine Research Day 2010, Howard University, Washington, DC, April 15 2011. p.65.
10. Wang PC, Wang TX, Korotcov AV, Chen Y, Sridhar R, Mitchell JW. Monitoring Thiol-Mediated Degradation of TOPO-Quantum Dots by ³¹P Nuclear Magnetic Resonance Spectroscopy. *Proceedings of Era of Hope 2011*, Orlando, FL, August 2–5, 2011. p.901
11. Wang PC, Liang XJ. Applications of Nanoparticles for In Vivo Imaging. *International Conference on Nanoscience & Technology, ChinaNANO 2011*, Beijing, China, September 7-9, 2011.
12. Korotcov AV, Wang TX, Chen Y, Sridhar R, Mitchell J, Wang PC. Study of TOPO-Quantum Dot Degradation by ³¹P NMR. *2011 World Molecular Imaging Congress*, San Diego, CA, September 7-10, 2011. P159
13. Zhang FY, Shan L, Liu YY, Neville D, Chen Y, Korotcov AV, Lin S, Huang S, Sridhar R, Liang W, Wang PC. Anti-PSMA Fold-back Diabody Fusion Diphtheria Immunotoxin Expresses Selectivity for Prostate Cancer Imaging and Therapy. (draft)

Appendix 1 Research Projects Supported by the Nanomedicine Core

1. Á Physicochemical Characteristics of Nanoparticles as MR Contrast Agent Delivery System with the Dynamic Contrast Enhancement Pattern for Clinical Applications (Wang PC, Korotcov A/ Radiology; Sridhar R/ Radiation Oncology; Bhujwala Z/Radiology/Johns Hopkins).
2. Á Develop multifunctional nanoparticles for breast cancer diagnosis and treatment – using anti-VEGFR-2 immunotoxin as dual purpose ligand and chemotherapeutics as encapsulated payload (Shan L, Zang FY/Radiology; Liu YY, Naville D/ NIH and Angimmune LLC).
3. Á Monitoring Thiol Mediated Degradation of TOPO-Quantum Dots by ³¹P NMR Spectroscopy (Wang TX/Chemical Engineering, Korotcov A/Radiology; Sridhar R/Radiation Oncology/Howard University).
4. Á Tumor Optical Imaging of Glucosamine Linked Fluorescent Probes in Mice (Korotcov A, Ye Y, Wang PC/Radiology; Achilefu S/Radiology/Washington University at St. Louis).
5. Á Integrin $\alpha\beta 3$ -targeted Prostate Cancer Imaging by Near-Infrared Fluorescent Mono- and Divalent RGD Compounds (Ye Y, Korotcov A/ Radiology/ Howard University).
6. Á Evaluation of Novel Disulfide-containing Cyclic RGD Compounds for Prostate Cancer Optical Imaging (Yunpeng Ye, Wang PC/Radiology/Howard University).
7. Á Protein Nanospheres: Synergistic Nanoplatfrom-Based Probes for Multimodality Imaging (McDonald MA/Material Measurement Laboratory/NIST, Wang PC/Radiology/Howard, Siegel EL/Radiology/University of Maryland).
8. Á Circumvention of Cisplatin-Resistance in Prostate Cancer (Canada R/Physiology and Biophysics)
9. Á Immunoliposome Based Nanotherapy of Brain Tumor (Chang E /Oncology/ Georgetown U)
10. Á Design of Multifunctional Polymeric Nanoparticles for Breast Cancer Diagnosis and Treatment (Akala E/Pharmacy)

Appendix 2 Students Participated in Nanomedicine Core Supported Research Projects

Postdoctoral Fellow

- Chung-Shieh Wu (Chemistry/Radiology)

Predoctoral M.D./Ph.D./Dental Students:

- Belinda Hauser (Genetics)
- Oluseyi Awodele (Medicine)
- Stephen Greene (Dentistry)
- Patrick Christophe (Dentistry)
- David Abdelmalak (Dentistry)
- Patrice Smith-Rios (Dentistry)
- Stephen Hayes (Dentistry)

Undergraduate student:

- Akeem Moore (Biology)
- Sophia Huang (Pre-med)



Synthesis of amphiphilic triblock copolymers as multidentate ligands for biocompatible coating of quantum dots

Tongxin Wang^{a,c,*}, Rajagopalan Sridhar^b, Alexandru Korotcov^a, Andy Hai Ting^c, Kyethann Francis^c, James Mitchell^c, Paul C. Wang^{a,**}

^a Department of Radiology, Howard University, Washington, DC 20060, USA

^b Department of Radiation Oncology, Howard University, Washington, DC 20060, USA

^c Crest Center for Nanomaterials, Howard University, Washington, DC 20060, USA

ARTICLE INFO

Article history:

Received 30 June 2010

Received in revised form 4 November 2010

Accepted 28 November 2010

Available online 10 December 2010

Keywords:

Quantum dot
Block copolymer
Nanoparticle
Biocompatible
Coating

ABSTRACT

One barrier to the application of current tri-octylphosphine oxide (TOPO) based quantum dots (QDs) for biomedical imaging is that the TOPO on TOPO-QDs can be replaced by the proteins in living system, which may cause the degradation of QDs and/or deactivation of protein. In order to develop biocompatible optical imaging agents, a novel triblock copolymer, designed as a multidentate ligand, was synthesized to coat quantum dot nanocrystals (QDs). The copolymer consists of a polycarboxylic acid block at one end and a polythiol block at the other end with an intervening cross-linked poly(styrene-co-divinylbenzene) block bridging the ends. The multiple mercapto groups from the polythiol block act as multidentate ligands to stabilize QDs, while the polycarboxylic acid block improves the water solubility of QDs and offers reaction sites for surface modification or conjugation with biomolecules. The cross-linked poly(styrene-co-divinylbenzene) block provides a densely compacted hydrophobic shell. This shell will act as a barrier to inhibit the degradation of QDs by preventing the diffusion of ions and small molecules into the core of QDs. This new multidentate polymer coating facilitates the transfer of QDs from organic solvent into aqueous phase. The QDs directly bound to multidentate mercapto groups instead of TOPO are less likely to be affected by the mercapto or disulfide groups within proteins or other biomolecules. Therefore, this research will provide an alternative coating material instead of TOPO to produce QDs which could be more suitable for *in vivo* use under complex physiological conditions.

© 2010 Elsevier B.V. All rights reserved.

1. Introduction

Due to its high sensitivity, relatively inexpensive cost and lack of any risk of exposure to ionizing radiation, optical imaging has become one of the attractive non-invasive diagnostic technologies for early detection of tumors, particularly for those situated near the body surface [1]. To improve the diagnostic accuracy of optical imaging, it is essential to develop highly sensitive, tissue and/or tumor specific contrast agents with adequate stability to withstand harsh physiological microenvironment. In comparison to conventional organic fluorescent probes, semiconductor quantum dots (QDs) based fluorescent imaging probes have several advantages, including (1) high resistance to photo-bleaching and chemical degradation; (2) size-dependent emission wavelength

from ultraviolet to near infrared range and wide adsorption spectra for excitation; (3) high quantum yield and molar extinction coefficients (~10–100-fold higher than those for organic dyes) [2–9]. In particular, the large molar extinction coefficient and resistance to photo-bleaching make QD an ideal agent for detection of small tumors.

Since the pioneering work by Alivisatos and co-workers [10] and Nie and co-worker [11], QDs have been covalently linked to various biomolecules such as antibodies, peptides, nucleic acids and other ligands for biological applications [12–27]. Recently, Wu et al. [28] described that QDs covalently linked to immunoglobulin G and streptavidin could effectively label the breast cancer marker Her2 on the surface of fixed and living cancer cells for cellular imaging. In spite of successful cellular labeling *in vitro*, there are few examples of the use of QDs for *in vivo* imaging of tumors in live animals. In a report by Chen and co-workers [29], commercially available QDs conjugated with RGD (arginine–glycine–aspartic acid) were shown to specifically bind to an $\alpha_v\beta_3$ integrin positive glioblastoma to enable *in vivo* optical imaging. In another report of *in vivo* imaging by Nie and co-workers [30], QD probes coated with an ABC triblock amphiphilic copolymer and tumor targeting ligands were shown to

* Corresponding author at: Howard University, Crest Center for Nanomaterials, 2300 6th Street NW, Washington, DC 20059, USA.

** Corresponding author.

E-mail addresses: twang@howard.edu (T. Wang), pwang@howard.edu (P.C. Wang).

accumulate in tumors because of enhanced vascular permeability and antibody binding to cancer-specific cell surface biomarkers. The authors pointed out that the strong hydrophobic interactions between the hydrophobic segment of the coating polymer and the trioctylphosphine oxide (TOPO) provide a protective hydrophobic coating layer that resists hydrolysis and enzymatic degradation of QDs even under complex *in vivo* conditions.

One key for successful *in vivo* imaging is that QDs should be able to withstand degradation by avoiding reaction with biomolecules under hostile physiological microenvironment. In general, surface coating of QDs is an efficient way to increase their stability, water solubility and biocompatibility by reducing toxicity [31]. Based on the TOPO coated QDs created by Bawendi and Murray [32], numerous techniques for surface coating have been developed. These methods can be generally classified as: encapsulation with silica shell, ligand exchange reaction with mercapto compounds, and encapsulation through hydrophobic interaction.

Encapsulation of QDs within silica shells is currently seldom used because of the relatively complicated procedure and the particularly large size of resulting QDs [10,33,34]. In contrast, coating of QDs with amphiphilic molecules through the hydrophobic interaction between TOPO and the polymers appears to be a promising approach for stabilizing QDs [12,35,36]. Its obvious advantage is the preservation of the native surface structure as well as the original quantum efficiency of QDs. This hydrophobic shell protects QDs against hydrolysis and enzymatic degradation [30]. Although these QDs are stable under usual chemical conditions, i.e., in water or buffer, they might not have sufficient biological stability, especially under the complex *in vivo* conditions in living systems. One major problem could arise from the surface exchange reaction between thiols from proteins and TOPO on the surface of QDs. There are ample mercapto groups in certain proteins, which can replace the TOPO on the surface of QDs. Such ligand exchange reactions may lead to the degradation of QDs under complex *in vivo* imaging conditions, resulting in the release of highly toxic Cd^{2+} ions. On the other hand, the direct binding of proteins to QDs may result in the alteration of the chemical conformation of proteins and loss of their bioactivities, as the mercapto and disulfide groups usually play critical roles in the conformation of proteins [37].

In order to develop physiologically stable QDs for *in vivo* imaging studies in live animals, coating of QDs with mercapto groups instead of TOPO may be an alternative strategy. Indeed, replacement of TOPO with mercapto compounds containing carboxylic acid or amino groups has previously been used as the representative ligand exchange reaction to prepare water-soluble QDs [11,38,39]. However, one of the major obstacles for this strategy is the insufficient stability of the resulting QDs due to the oxidation of the low molecular weight mono-thiols into disulfides. Recent studies show that the stability and resistance of QDs to chemical degradation can be improved through modification with bidentate ligand [40,41]. Additionally, multidentate ligands based on polyamines, such as polyethyleneimine or poly(2-N,N-dimethylaminoethyl methacrylate), have been used to coat and improve the stability of QDs [42–47].

Therefore, in this study, we took advantage of mercapto groups, multidentate effect and hydrophobic shell to design a novel triblock copolymer for surface coating of quantum dots (CdSe-ZnS). The triblock copolymer, synthesized by successive atom transfer radical polymerization (ATRP), consists of a polycarboxylic acid at one end, a polythiol block at the other end and an intermediate poly(styrene/divinylbenzene) block, which is densely compacted and strongly hydrophobic. The polythiol block is derived from bis[2-(2-bromoisobutyryloxy)ethyl] disulfide initiators. The multiple mercapto groups of the polythiol block serve as multidentate ligands not only to bind QDs but also to prevent the exchange reaction between TOPO on the surface of QDs and biomolecules

such as proteins in living systems. The polycarboxylic acid block, derived from *t*-butyl acrylate, will improve the water solubility of QDs and provide reaction sites for bioconjugation. In addition to the multidentate effect, divinylbenzene monomers were copolymerized with styrene to form a cross-linked hydrophobic segment separating the polycarboxylic block from the polythiol block. The densely compacted hydrophobic shell formed from the cross-linked poly(styrene/divinylbenzene) block will prohibit the diffusion of other molecules or ions through the hydrophobic shell so as to protect QDs from hydrolytic and enzymatic degradation.

2. Experimental

2.1. Materials

The monomers for successive ATRP polymerization, including styrene (ST, 99%, Sigma–Aldrich), divinylbenzene (DVB, 80%, Polysciences) and *t*-butyl acrylate (tBA, 99%, Aldrich) were purified by passing through short columns filled with basic alumina to remove radical inhibitors prior to use. CuBr (98%, Acros) was purified by washing repeatedly with glacial acetic acid followed by ether, and then stored under argon after drying. All other reagents, including 2-mercaptoethanol (Sigma), hydrogen peroxide (30% aqueous solution, Fisher), triethylamine (99%, Fisher), 2-bromoisobutyryl bromide (98%, Aldrich) and 2,2'-bispyridine (98%, Acros) were used without further purification.

All chemicals for preparation of QDs, including cadmium oxide (99.998%, Alfa Aesar), stearic acid (99%, Alfa Aesar), tri-*n*-octylphosphine oxide (TOPO, 90%, Aldrich), 1-hexadecylamine (90%, Alfa Aesar), trioctylphosphine (TOP, 90%, Aldrich), dimethylzinc (1.2 mol/L solution in toluene, Acros), and hexamethyldisilathiane (Fluka) were used as received.

2.2. Synthesis of disulfide (2)

Hydrogen peroxide (8.5 g of 30% aqueous solution, 75 mmol) was diluted with 10 mL of water. The diluted hydrogen peroxide was added dropwise into a solution of 2-mercaptoethanol (7.8 g, 100 mmol) in 25 mL of water. After 1 h of stirring at room temperature, the reaction mixture was extracted with 50 mL ethyl acetate three times. The ethyl acetate extract was dried over anhydrous sodium sulfate. After removal of sodium sulfate by filtering, the organic solvent was evaporated off under vacuum to obtain the disulfide **2** (Fig. 1) as a viscous oil in 92% yield. ^1H NMR (CDCl_3 ; δ , ppm): 2.56 (t, 2H, CH_2S), 3.58 (t, 2H, CH_2O). The scheme for chemical synthesis is shown in Fig. 1.

2.3. Synthesis of disulfide initiator (4)

The initiator **4** (Fig. 1) was prepared by a modified literature method [48,49]. Disulfide **2** (1.54 g, 10 mmol) and triethylamine (3.03 g, 30 mmol) were dissolved in dry THF (30 mL). After bubbling argon through the reaction mixture for 30 min, a solution of 2-bromoisobutyryl bromide **3** (9 g, 30 mmol in 10 mL of dry THF) was added under vigorous stirring within an ice bath. The reaction mixture was kept stirred in the ice bath for 10 min and then at room temperature for 2 h. 200 mL of water was added to quench the reaction. The aqueous solution was extracted with three portions of 50 mL ethyl acetate. The combined organic solvent was thoroughly washed first with aqueous sodium bicarbonate solution (1%, 50 mL) and then with water (50 mL), respectively. The organic extract was dried over anhydrous sodium sulfate. Sodium sulfate was removed by filtering and then ethyl acetate was evaporated by using a rotary evaporator to obtain crude product **4** (viscous brown oil, 89% yield). A light yellow oil was obtained after further purification by column chromatography (silica gel 60, dichloromethane as eluent). ^1H NMR

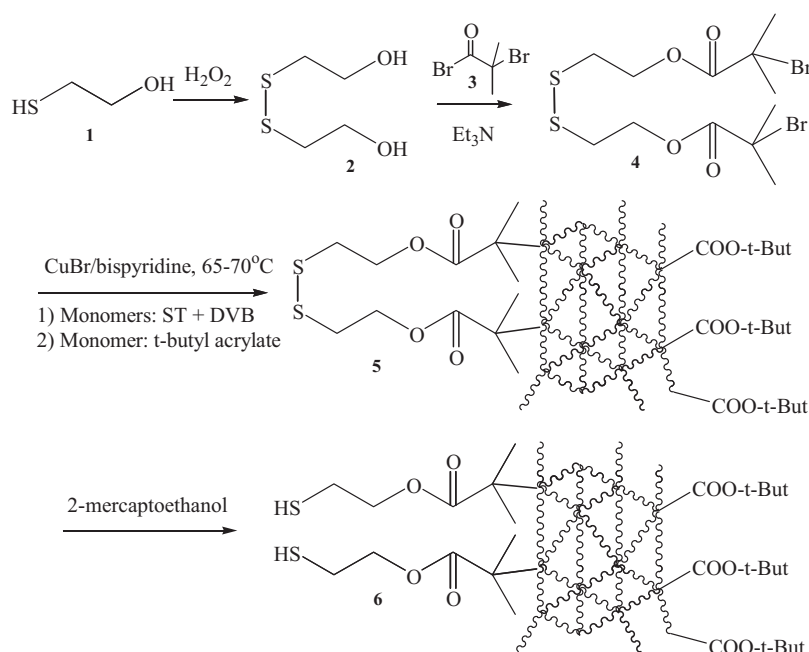


Fig. 1. Synthesis of disulfide initiator **4** and successive ATRP (atom transfer radical polymerization) to generate cross-linked multidentate triblock copolymer **6**.

(CDCl₃; δ , ppm): 4.44 (t, 2H, CH₂OOC), 2.98 (t, 2H, CH₂S) and 1.94 (s, 6H, (CH₃)₂CBr).

2.4. Preparation of the cross-linked multidentate triblock copolymer (**5**) by successive ATRP from ST, DVB and tBA.

Polymerization of ST and DVB was initiated using the disulfide initiator **4** (Fig. 1). Prior to polymerization experiments, the initiator was deoxygenated by bubbling with argon for 3 h. The effect of varying molar ratio of monomers, concentration, reaction time and temperature on polymerization as well as molecular weight was examined (Table 1). Typically, 650 mg of ST (6.25 mmol) and 406 mg of DVB (3.125 mmol) were added into 2 mL of diphenyl ether. The mixture was degassed by 4 freeze–pump–thaw cycles. 71.5 mg of CuBr (0.5 mmol) and 156.2 mg of 2,2′-bispyridine (1.0 mmol) were added into the frozen mixture. The flask was backfilled with argon and the mixture was warmed to room temperature. Then, 113 mg of the degassed disulfide initiator **4** (0.25 mmol, molar ratio of 1/25 vs ST monomer) was injected through a syringe. The mixture was immediately heated to 65–75 °C. 100 μ L of sample was taken out

every 30 min and the polymeric product was precipitated by addition of 1 mL methanol to monitor the polymerization.

After the polymerization of ST and DVB had progressed for 2.5 h, 400 mg of tBA (3.125 mmol) was added immediately. The reaction continued for another 1 h to allow polymerization of tBA to proceed. The cooled mixture was purified by reprecipitation with methanol/dichloromethane. Briefly, 1 mL of the reaction mixture was added into 5 mL of methanol and then centrifuged at 8000 rpm for 5 min. After washing with 1 mL methanol three times, the precipitated polymer was redissolved in 0.25 mL dichloromethane, and the resulting suspension was centrifuged at 8000 rpm for 5 min to remove the insoluble copper catalyst. The polymer was reprecipitated by addition of 1 mL of methanol and separated by centrifugation. The procedures were repeated three times to thoroughly remove the unpolymers and insoluble catalyst. The triblock copolymer **5** (Fig. 1) was then dried overnight under vacuum at room temperature. ¹H NMR (CDCl₃; δ , ppm): 6–8 (br), 3–4 (br) and 1–2 (br). Molecular weight distribution of polymer was determined on the basis of gel permeation chromatography (GPC).

Table 1

Experimental conditions, feeding ratio of reactants, and results for polymerization of styrene (ST), divinylbenzene (DVB), *t*-butyl acrylate (tBA) by ATRP.

No. of experiment	Molar ratio of I/ST/DVB/tBA	Temperature	Volume of solvent (mL)	Results of polymerization
1	1:25:12.5:0	90 °C	2 mL	Gelation
2	1:25:12.5:0	70 °C	2 mL	Controlled
3	1:25:12.5:0	60 °C	2 mL	No polymer
5	1:25:12.5:0	70 °C	4 mL	Controlled
6	1:25:12.5:0	70 °C	0.5 mL	Gelation
7	1:25:0:0	70 °C	2 mL	Controlled
8	1:0:25:0	70 °C	2 mL	Gelation
9	1:25:25:0	70 °C	2 mL	Gelation
10	1:12.5:25:0	70 °C	2 mL	Gelation
11	1:25:12.5:12.5	70 °C	2 mL	Controlled

(a) The feeding amount of disulfide initiator (I), CuBr or 2,2′-bispyridine is fixed at 0.25, 0.5 and 1.0 mmol, respectively. (b) The meaning of ‘controlled’ is that the amount or molecular weight of polymer can be controlled by the temperature, feeding ratio or time of polymerization.

2.5. Reductive cleavage of disulfide bonds within polymer **5** into mercapto groups

100 mg of block copolymer **5** (Fig. 1) was dissolved in 1 mL of DMF followed by addition of 2-mercaptoethanol (0.1 mL). After stirring overnight under argon protection, the mixture was poured into 10 mL of water, and then extracted three times with 20 mL of dichloromethane. After evaporation of organic solvent, the polymer **6** (Fig. 1) was reprecipitated three times using dichloromethane–methanol mixture to completely remove the residual 2-mercaptoethanol, and kept in argon before ligand exchange with TOPO/QDs.

2.6. Synthesis of TOPO stabilized quantum dot nanocrystals (TOPO/QDs)

TOPO/QDs in this paper represent CdSe–ZnS core-shell nanocrystals stabilized with TOPO. TOPO/QDs were synthesized according to the method described in the literature [30]. Cadmium oxide (25.6 mg, 0.2 mmol), stearic acid (0.5 g) and TOPO (2.0 g) were mixed and flushed with argon flow. Then, the mixture was heated to 250 °C until a clear solution was formed. Two grams of hexadecylamine was added to the clear solution after it had cooled down to room temperature. The mixture was heated back to 250 °C for 10 min and then raised to 300 °C. Selenium (15.8 mg, 0.2 mmol) in 2 mL of trioctyl phosphine was quickly injected into the hot solution. The mixture immediately changed colour to orange red, indicating formation of quantum dots. The reaction mixture was refluxed for 30 min, and then cooled down to 220 °C. Dimethylzinc (83.3 μ L of 1.2 mol/L in toluene, 0.1 mmol) and hexamethyldisilathiane (17.8 mg, 0.1 mmol) in 5 mL of trioctyl phosphine were slowly added dropwise (over 10 min) to the reaction mixture at 220 °C. The mixture was refluxed for 30 min and then cooled to room temperature. The TOPO/QDs were extracted with toluene or hexane and reprecipitated with methanol for 5 times. Size selective precipitation was performed using methanol and hexane. The TOPO/QDs were redispersed in toluene or chloroform for measuring dynamic light scattering (DLS) and recording UV–vis and fluorescent spectra.

2.7. Surface ligand exchange of TOPO/QDs with multimercapto polymers and formation of water-soluble QDs

5 mg of the multimercapto triblock copolymer **6** (Fig. 1) was dissolved in 1 mL of toluene. 2.0 mg of TOPO/QDs in toluene (1 mL) was added into the polymer solution under vigorous stirring in an argon atmosphere. The mixture was continuously stirred at room temperature for 2 h under argon. 5 mL of methanol was added into the above mixture and the resulting precipitated polymer stabilized QDs were collected by centrifugation at 8000 rpm. The polymer stabilized QDs were redispersed in toluene and precipitated again by addition of methanol in order to remove the dissociated TOPO and large excess of polymers.

Hydrolysis of the acrylate groups on the surface of QDs into carboxylic acid groups was carried out in a toluene–H₂O–NaOH heterogeneous system. The above polymer coated QDs were dispersed in 1 mL of toluene and mixed with 1 mL of 1% NaOH aqueous solution. After the heterogeneous mixture was vigorously stirred for 30 min under argon, the QDs were partitioned into the aqueous phase, which turned brown due to the formation of water-soluble QDs. The water-soluble QDs were separated from toluene using a separatory funnel and kept at pH 8 at 4 °C.

2.8. Characterization

¹H NMR spectra were recorded on a 400 MHz Bruker instrument. UV–vis spectra were recorded on a Cary 5000 spectrometer using a 1.0 cm quartz cuvette. Emission spectra were measured on a Hitachi F-7000 fluorescent spectrometer using a 1.0 cm quartz cuvette. The molecular weights of polymers were determined using a PL-GPC 50 gel permeation chromatograph (Polymer Laboratories) using THF as eluent and toluene as the internal standard (flow rate of 1.0 mL/min and differential refractive index (RI) detector). The apparent molecular weights and polydispersity were determined with a calibration based on polystyrene standards. Fourier transformed infrared spectra (FTIR) were collected on polymer/KBr pellets from 4000 to 650 cm^{−1}, using a Magna-IR 550 Spectrometer Series II (Nicolet). The polymer was mixed with 70 mg of spectroscopic grade KBr at a 1% (w/w) and ground into fine powder. The pellets (7 mm diameter) were pressed with a ThermobSpectra-Tech's Qwik Handi-Press for 5 min. Transmission electron micrographs (TEM) were taken by a JEOL 3010 HREM operating at 100 kV. Sample for TEM was prepared by depositing a drop of suspension of QDs onto carbon-coated Cu grids followed with drying at room temperature.

3. Results and discussion

3.1. Preparation of the multidentate triblock copolymer by successive atom transfer radical polymerization (ATRP)

The multidentate triblock copolymer **6** (Fig. 1) was designed for surface coating of QDs. The first block containing multiple thiols was designed as the multidentate ligand for surface coating of QDs. Recent studies show that, in comparison to low molecular weight monothiol, bidentate thiol can effectively improve the stability and resistance of QDs to chemical degradation [40,41]. Consequently, it is expected that multidentate thiols may lead to greater stability of QDs. Through the chelating effect, the multidentate mercapto groups will bind strongly to the surface of QDs, resulting in greater stability of QDs [40]. In addition, because this block is a mercapto group based stabilizer, it will reduce the possibility of the exchange reaction between TOPO on QDs and biomolecules such as proteins containing thiol groups. The second block is a cross-linked hydrophobic block which will form a densely compacted hydrophobic shell around QDs. This hydrophobic shell will prohibit the diffusion of other water-soluble molecules or ions within living systems into QDs core, so as to protect QDs from hydrolytic and enzymatic degradation. The third block consists of multiple *t*-butyl acrylates which can be hydrolyzed into carboxylic acid groups. This polycarboxylic block will improve the water solubility and biocompatibility of QDs, and provide reaction sites for subsequent bioconjugation for targeted delivery [30].

The triblock copolymer was prepared by successive atom transfer radical polymerization (ATRP) (Fig. 1). The first block, the multimercapto block, was generated from an initiator, disulfide **4**, which can be cleaved into thiols for QDs coating. The reason to use disulfide **4**, instead of thiol **1** as the initiator is because an unwanted chain transfer radical polymerization from thiol will occur if the initiator contains a mercapto group [50]. The disulfide initiator **4** was synthesized from 2,2'-dihydroxyethyl disulfide **2** and 2-bromoisobutryl bromide **3**. The bromoisobutryl group within the resulting disulfide initiator decomposed in the presence of CuBr/bispyridine to generate free radicals to initiate the successive ATRP with ST, DVB, tBA to generate the triblock copolymer. Finally, reductive cleavage of the disulfide bonds in the first block generated the multi-dentate mercapto groups, which are the binding groups to stabilize QDs.

The second block, a cross-linked hydrophobic block, was polymerized from ST and DVB. There are three reasons to select these two monomers. First, both ST and DVB are hydrophobic monomers, which can protect the core of QDs by preventing the diffusion of biological molecules and ions in physiological milieu (usually hydrophilic) into the polymeric shell. Second, the polymer block from these monomers tend to form a densely compacted structure through the strong π – π interaction between the benzene moieties within ST and DVB. Third, the densely compacted hydrophobic polymeric shell will be further strengthened as a result of cross-linking of the ethylene groups of DVB during polymerization. Recent studies indicate that such cross-linking of polymer can protect QDs core. The study of poly(maleic anhydride-*alt*-tetradecene) indicated that the stability was increased by cross-linking of the polymers [35]. Another report used lysines as linkers to generate such a cross-linked shell [51,52]. In comparison to the amide groups from lysines, the block copolymerized from ST and DVB within our triblock copolymer will have greater hydrophobicity, thus it is expected that this polymer has greater capability to prevent the diffusion of biological molecules and ions into the core.

The third block containing multiple carboxylic acids makes QDs water-soluble and biocompatible, while furnishing reaction sites for pegylation or conjugation with tumor-targeting ligands. Direct polymerization of acrylic acids is not suitable for ATRP, because the acid groups can coordinate with the copper ions and poison the catalysts. In addition, bipyridine, the complex ligand for CuBr catalyst, can be protonated by carboxylic acid, resulting in decomplexation of copper bipyridyl complex catalyst. An alternative approach to prepare polymethacrylic acids by ATRP is to polymerize the protected monomers such as *t*-butyl methacrylate, and benzyl methacrylate followed by hydrolysis [53]. In the present approach, the carboxylic block was generated from tBA, which were subsequently hydrolyzed to carboxylic acids.

The polymerization of the monomers ST or DVB, individually and in combination, was examined in a number of solvents, such as acetone, toluene and diphenyl ether. The progress of polymerization was primarily monitored by the precipitation of the polymer from reaction mixture with methanol. Polymerization was not observed even after being refluxed in acetone overnight, probably due to the lower boiling point of acetone. Similar result was found from the solvent of toluene when the temperature is below 60 °C (experiment 3 in Table 1). However, polymerization of ST and DVB occurred at temperatures above 65 °C in toluene or diphenyl ether as solvents. Temperature plays a critical role in the progress of ATRP and control of the molecular weights of polymers because high temperature leads to a faster polymerization. Linear polyST homopolymer as well as its block copolymer with poly(methyl acrylate) containing mercapto groups have been reported in the literature [48,49]. In Ref. [48], polymerization of ST initiated by a similar disulfide initiator at 90 °C led to a polymer with molecular weight around 1.5×10^4 g/mol. Our first experiment carried out at 90 °C immediately resulted in a gelled structure within only 20 min at the molar ratio of 1:25:12.5 (initiator:ST:DVB) (experiment 1 in Table 1). This suggests that the polymerization rate is too fast at such a high temperature to control the degree of cross-linking.

Therefore, in order to prepare polymers with relatively low and controllable molecular weights, copolymerization of ST and DVB was carried out at a reaction temperature below 90 °C. However, if the temperature is below 60 °C, no obvious polymerization occurred even though the reaction mixture was stirred overnight. Eventually, the temperature between 65 and 75 °C was selected for copolymerization of ST and DVB for controllable molecular weight.

The feeding ratio of monomer is central to controlling molecular weight and the degree of cross-linking. Polymerization from single monomer and co-monomers at variable feeding ratio is shown in

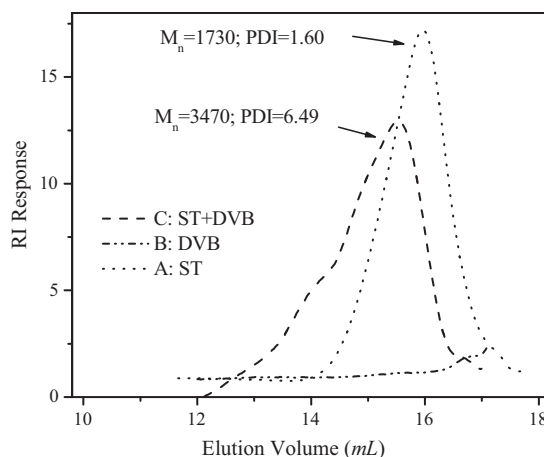


Fig. 2. GPC (gel permeation chromatography) profiles of homopolymers or copolymer from monomers: styrene (ST) and divinylbenzene (DVB). All polymerizations were carried out for 2.5 h at 65 °C. THF was used as the eluting solvent at a flow rate of 1.0 mL/min and toluene was used as an internal standard with refractive index detection. The instrument was calibrated using standard polystyrene samples.

Table 1. The result of polymerization and the degree of cross-linking can be primarily observed by eye on the experimental phenomenon and indicated by the solubility of the resulting polymer within variable solvents, e.g., THF or dichloromethane. The homopolymer of polyST generated after 2.5 h at 65–70 °C in diphenyl ether was completely soluble in both THF and dichloromethane (experiment 7 in Table 1). However, the homopolymer from DVB alone (poly-DVB) was completely insoluble in either THF or dichloromethane (experiment 8 in Table 1). The insolubility and swelling property of polyDVB in THF and dichloromethane implies its highly cross-linked structure.

The combination of ST and DVB will lead to copolymers with cross-linked structures, but with a relatively low degree of cross-linking. In addition, the degree of cross-linking and the molecular weights of the copolymers, which can be indicated by its solubility, can be controlled by the molar ratio of ST and DVB (DVB/ST). As expected, the solubility of poly(ST-*co*-DVB) copolymer is intermediate between that of polyST and polyDVB. If the molar ratio of DVB/ST was increased, then the solubility of copolymer decreased, indicating the increase in degree of cross-linking. When the feeding ratio of ST and DVB is 2:1, 2.0 mg of poly(ST-*co*-DVB) is completely soluble in 200 μ L of dichloromethane and THF completely (experiment 2 in Table 1). When the molar ratio increases to 1:1, the solubility in THF decreases sharply, but the polymer can still be dissolved in dichloromethane (0.8 mg insoluble residual from the original 2.0 mg of copolymer, experiment 9 in Table 1). If the molar ratio increases to 1:2 (ST/DVB), 2 mg of copolymer is hardly soluble in THF and dichloromethane, which is similar to polyDVB (experiment 10 in Table 1).

Quantitatively, GPC measurements on the prepared polymers are in agreement with their solubility characteristics in THF or dichloromethane. When the same amount (2.0 mg) of the polymers was used for GPC analysis, the GPC profiles of polyST and polyDVB were quite different (Fig. 2). PolyST shows a longer elution time (i.e., larger elution volume) indicating a lower molecular weight (1730 g/mol with a polydispersity of 1.60, line A in Fig. 2). The GPC profile of polyDVB consists of an almost flat elution pattern with very weak intensity, except for a small peak around elution volume of 17 mL (line B in Fig. 2). The small peak may be due to the residual monomer, rather than small molecular weight polymeric species. The weak intensity indicates that hardly any soluble polymer can be detected. This supports the insolubility of polyDVB in THF, indicating a gelled structure with high degree of cross-linking.

Line C in Fig. 2 shows a GPC profile of the copolymer (poly(ST-co-DVB)) from the mixed monomers in a molar ratio of 2/1 (ST/DVB). It shows a relatively low elution volume and an intermediate molecular weight of 3470 g/mol. The molecular weight is greater than that of polyST but is certainly lower than that of polyDVB, the highly cross-linked gelled structure. By adjusting the molar ratio of monomer ST and DVB, the degree of cross-linking and molecular weight of polymer can be tuned.

Unlike the feeding ratio of monomers, the effect of monomer concentration at a fixed molar ratio of ST/DVB to the molecular weight was not observed. In order to examine the concentration effect, an experiment using a fixed molar ratio of disulfide initiator, ST and DVB (initiator/ST/DVB = 1:25:12.5) was conducted using different volumes of solvent. When the solvent volume was taken as 2 mL and 4 mL for the same amount of monomers (experiments 2 and 5 in Table 1), the resulting polymers possessed similar molecular weights shown by GPC (data not shown). However, the yield of polymer from the low concentration is less than that from high concentration at the same time of polymerization. This implies that the polymer molecular weight was probably independent of the concentration at the tested range. However, if the solvent is as little as 0.5 mL, monomer concentration is so high as a bulk polymerization that only gelled product with a very high molecular weight was formed (experiment 6 in Table 1).

Time dependent polymerization showed a gradual increase in the amount of polymer, but did not demonstrate an obvious molecular weight change during a 4-h period. The time dependent polymerization was examined at a constant molar ratio of the initiator to monomers (initiator/ST/DVB = 1/25/12.5) between 65 and 75 °C. In order to monitor the progress of polymerization, a sample (0.1 mL) was taken out every 30 min during a polymerization period of 4 h. Then, 1.0 mL of methanol was added to each sample to precipitate the polymer for GPC measurements. In the first 30 min, hardly any polymer could be precipitated from methanol. With increasing reaction time, more polymers were precipitated (i.e., 0.5 mg, 1.8 mg and 4.2 mg from the samples polymerized for 1 h, 1.5 h and 2.5 h, respectively). This indicates the continuous polymerization over time. The gradual increase in the amount of polymer indicates that the polymerization process can be well controlled by the polymerization time within such a temperature range. However, GPC measurements showed no obvious effect of reaction time on molecular weight of polymer. The molecular weights of poly(ST-co-DVB) sampled at different times are close to each other. For example, the molecular weights of poly(ST-co-DVB)s from polymerization reactions after 1 h and 2.5 h are approximately 3470 g/mol (lines A and B in Fig. 3). This is in agreement with the chain reaction mechanism of addition polymerization of unsaturated monomers which leads to formation of products with invariable molecular weight [54]. Primary activation of a monomer is followed by the addition of other monomers in rapid succession until the growing chain is eventually deactivated under our experimental conditions.

Once the cross-linked polymer of poly(ST-co-DVB) was formed, poly(*t*-butyl acrylate) (polytBA) block can successively grow to generate the triblock copolymer. The successive growth of polytBA is evidenced by GPC measurement. Although there is no obvious increase of molecular weight of poly(ST-co-DVB) with polymerization time, the molecular weight increased immediately to 4921 g/mol after addition of tBA (lines C and D in Fig. 3). The GPC elution peak around 3470 g/mol (poly(ST-co-DVB)) disappeared when tBA was added. The control experiment without addition of tBA still kept the molecular weight of polymer around 3470 g/mol of poly(ST-co-DVB). This confirms that polytBA block was growing from the existing poly(ST-co-DVB) macroinitiator to form the final block copolymer: poly(ST-co-DVB-*b*-tBA).

Fourier transformed infrared spectroscopy (FTIR) confirmed the formation of the block copolymer. Fig. 4 is the FTIR spectrum of

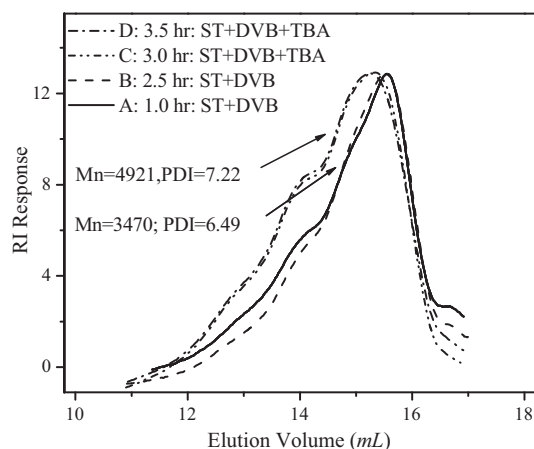


Fig. 3. GPC profiles of copolymers showing the effect of polymerization time and monomers on molecular weights. Polymerization was conducted at 65 °C. Styrene (ST) and divinylbenzene (DVB) were copolymerized from the beginning, while *t*-butyl acrylate (tBA) was added at 2.5 h of polymerization to form the block copolymer. GPC condition is the same as that in Fig. 2.

the prepared polymer before and after addition of tBA. In both spectra, the strong peaks at 3025 and 2927 cm⁻¹ are attributed the stretch of CH₂. The peaks at 1600, 1493 and 1454 cm⁻¹ from both spectra are the typical characteristics of benzene within styrene and DVB. This is in agreement with the previous conclusion that ST has been cross-linked with DVB (Fig. 2). Significantly, in addition to the major peaks from ST and DVB, the spectrum of polymer after addition of tBA shows additional two strong peaks at 1728 cm⁻¹ (C=O) and 1151 cm⁻¹ (C–O from ester). Because the residual tBA monomers have been completely removed by

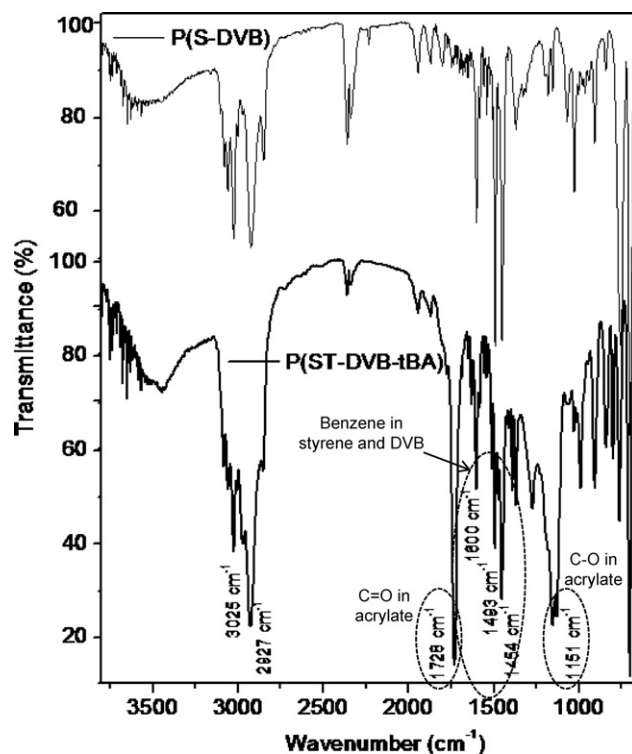


Fig. 4. FTIR spectra of polymer from styrene and divinylbenzene before (spectrum of P(ST-co-DVB)) and after (spectrum of P(ST-co-DVB-*b*-tBA)) addition of *t*-butyl acrylate. The co-existing of the vibration peak of benzene (1600, 1493 and 1454 cm⁻¹) and ester (1728 and 1151 cm⁻¹) indicates the formation of the block copolymer, P(ST-co-DVB-*b*-tBA).

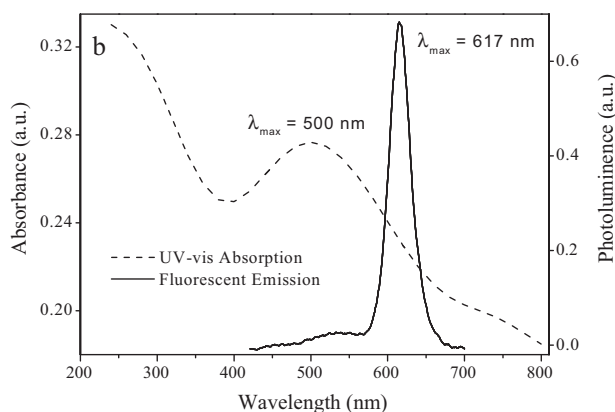


Fig. 5. Absorption spectra and photoluminescence spectra of TOPO/QDs in toluene.

reprecipitation with methanol/dichloromethane, the co-existence of *t*-butylacrylate and styrene in the FTIR confirms the formation of the triblock copolymer, poly(ST-*co*-DVB-*b*-tBA).

Conclusively, polymerization of ST and DVB can be initiated by the newly prepared disulfide initiator **4**. The temperature and molar ratio of monomers are critical to control the cross-linking degree and molecular weight of copolymer. tBA block can grow from the poly(ST-*co*-DVB) macroinitiator to generate the block copolymer poly(ST-*co*-DVB-*b*-tBA). Disulfide in the first block will be cleaved into mercapto groups for surface coating of QDs. The intermediate ST/DVB block will form a cross-linked hydrophobic shell to protect QDs. The tBA within the third block will be hydrolyzed into carboxylic acid so as to make QDs water-soluble and offer reaction site for further conjugation with targeting delivery ligand.

3.2. Surface coating of QDs with multidentate block copolymers

TOPO stabilized CdSe-ZnS QDs (TOPO/QDs) were synthesized for ligand exchange with multimercapto copolymers. The TOPO/QDs were synthesized using cadmium oxide and selenium as reactants and dimethyl zinc and hexamethyldisilathiane as ZnS coating precursors according to the method described in the literature [30]. Fractionation by centrifugation was followed by size selective precipitation from toluene or hexane solution by addition of methanol, yielding QDs with size distribution within a narrow range. Transmission electron microscopy (TEM) measurement indicates that these QDs are nearly spherical particles at an average diameter of 4.5 nm together with some rod-like structures at about 6.8 nm length.

The optical properties of QDs were confirmed by fluorescent emission and UV-vis absorption spectra (Fig. 5). The broad absorption around 500 nm in UV-vis spectrum is a typical characteristic of QDs. The maximum absorption around 500 nm in UV-vis spectrum and maximum fluorescent emission at 617 nm in fluorescent spectrum are in agreement with earlier studies [41].

The above TOPO/QDs are soluble in non-polar solvent such as toluene or chloroform but are insoluble in methanol or water (sample A in Fig. 6). For biological application, additional surface coating is necessary to improve the water solubility and biocompatibility of QDs.

The new triblock copolymer containing multidentate mercapto groups can effectively coat QDs and make them water-soluble. Water-soluble QDs were prepared by the ligand surface exchange reaction between polymer and TOPO/QDs in toluene followed by hydrolysis of *t*-butyl acrylates into carboxylic acids [40].

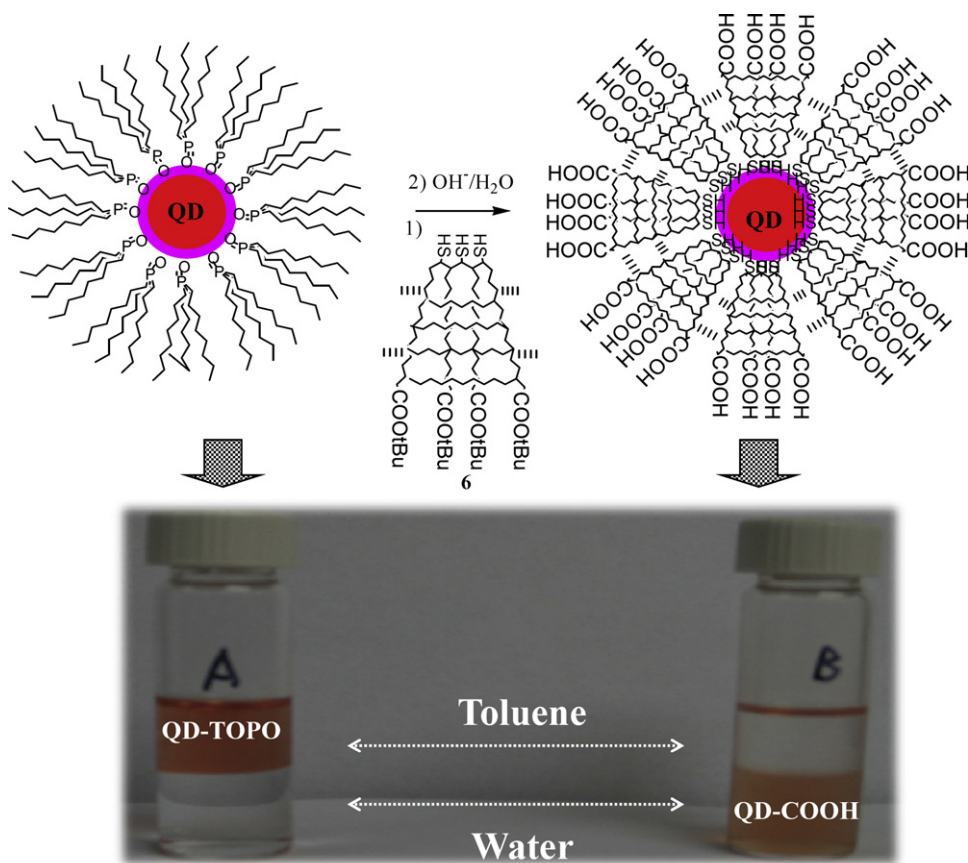


Fig. 6. Scheme of ligand exchange reaction between multidentate block copolymers and TOPO/QDs and transferring QDs from organic phase to aqueous phase: (A) a control experiment of TOPO/QDs before ligand exchange reaction and (B) the toluene–water system after ligand exchange reaction, showing QDs in the aqueous phase.

Disulfides bind poorly with QDs, whereas thiols bind well with QDs. Therefore, the multiple disulfides within polymers need to be cleaved into thiols for strong binding to QDs. The disulfide bond can be reductively cleaved into thiols either by free thiol (e.g., dithiothreitol or 2-mercaptoethanol) or by phosphines (e.g., Bu_3P) [55]. In this research, the disulfides were cleaved using 2-mercaptoethanol in DMF according to the published method [48]. Reduction was carried out under argon atmosphere in order to avoid air oxidation of the thiol groups within polymers and 2-mercaptoethanol.

It is well-known that TOPO on QDs can be easily replaced by mercapto groups [11,38,39]. Through the multidentate mercapto groups, the new triblock copolymer will replace TOPO and link with QDs. A large excess of polymers were used for ligand exchange reaction to avoid cross-linking between QDs. Argon atmosphere is critical to prevent oxidation of the multiple mercapto groups during ligand exchange reaction. Because the hydrophobicity of tBA, the resulted polymer coated QDs are soluble in chloroform or toluene. Following hydrolysis, the QDs were completely water soluble implying the formation of carboxylic acids on the surface of QDs.

Hydrolysis of tBA into carboxylic acid was conducted in a heterogeneous mixture of diluted NaOH (1%) aqueous solution and polymer coated QDs in toluene in an argon atmosphere. The progress of hydrolysis was monitored by the solubility of the resulting QDs in water. After hydrolysis for about half an hour, the QDs were completely transferred into aqueous phase, indicating by the brown colour of aqueous phase (sample B in Fig. 6). The formation of water-soluble QDs confirms the generation of carboxylic acid from tBA.

Therefore, the new triblock copolymer can be successfully used as surface coating material to prepare water-soluble QDs. The TOPO ligand on the surface of TOPO/QDs can be replaced with the new multimercapto groups. By hydrolyzing the carboxylate groups, QDs can be transferred into aqueous phase. In addition to improve the water solubility, the carboxylic acids on QDs can also be used as functional groups to conjugate with biomolecules (e.g., protein or antibodies) for targeted imaging. A drawback of such aqueous QDs suspensions is their low stability in water, shown by the aggregation after 1 h at room temperature. Possible reasons might be the easy oxidation of mercapto groups or/and the over-cross-linking of the multi-dentate polymer with too high molecular weight. Further research will be focused on improvement of the chemical stability of such aqueous QDs through disulfide stabilizing groups and/or molecular weight control of polymer. Conjugation of QDs with biomolecules for cellular labeling and *in vivo* imaging studies in live animals will also be explored.

4. Conclusions

A new kind of polymer was successfully synthesized through successive atom transfer radical polymerization from disulfide initiator and three different monomers: styrene, divinylbenzene and *t*-butyl acrylate. This polymer – designed for surface coating of QD nanocrystals – is composed of three different blocks: polythiol, poly(styrene-co-divinylbenzene) and polycarboxylic acid. The multiple mercapto groups of the polythiol block act as multidentate ligands to stabilize QDs. The polycarboxylic acid block generated from poly(*t*-butyl acrylate) not only makes QDs water-soluble but also offers reaction sites for further bioconjugation of QDs for targeted molecular imaging. The intermediate poly(styrene-co-divinylbenzene) block is a hydrophobic block formed from cross-linked poly(styrene-co-divinylbenzene). The cross-linking degree of this block can be controlled through reaction time, monomer molar ratio and reaction temperature. This block will form a densely compacted hydrophobic shell during coating of QDs

and will effectively prevent the diffusion of other molecules into the QDs core, so as to better protect the QD cores against decomposition.

By using this triblock copolymer, QDs can be transferred from toluene to water efficiently. Because the multidentate mercapto groups instead of TOPO are the functional groups to bind with QDs, such QDs will be less likely to be displaced by the mercapto or disulfide groups within proteins or other biomolecules. An existing problem of the prepared QDs is the insufficient stability, which might be due to the oxidation the mercapto groups. With the improvement of the stability of QDs in the future study, this research will provide an alternative coating material to produce QDs which could be more suitable for *in vivo* use under complex physiological conditions than the current TOPO stabilized QDs.

Acknowledgments

This work was supported by DoD USAMRMC W81XWH-05-1-0291, NIH/NCRR/RCMI 2G12 RR003048 and NIH 5U54CA091409-06. Mr. Haiyong He and Dr. Xingjie Liang are acknowledged for TEM measurements. The authors also thank Prof. Zaver Bhujwala and Prof. Oladapo Bakare for helpful discussions and support.

References

- [1] M.G. Pomper, J.S. Lee, *Curr. Pharm. Design* 11 (2005) 3247.
- [2] A.P. Alivisatos, W. Gu, C. Larabell, *Annu. Rev. Biomed. Eng.* 7 (2005) 55.
- [3] A.M. Smith, X. Gao, S. Nie, *Photochem. Photobiol.* 80 (2004) 377.
- [4] B.O. Dabbousi, J. Rodriguez-Viejo, F.V. Mikulec, J.R. Heine, H. Mattoussi, R. Ober, K.F. Jensen, M.G. Bawendi, *J. Phys. Chem. B* 101 (1997) 9463.
- [5] C.A. Leatherdale, W.K. Woo, F.V. Mikulec, M.G. Bawendi, *J. Phys. Chem. B* 106 (2002) 7619.
- [6] C.J. Murphy, *Anal. Chem.* 74 (2002) 520A.
- [7] W.J. Parak, D. Gerion, T. Pellegrino, D. Zanchet, C. Micheel, S.C. Williams, R. Boudreau, M.A. Le Gros, C.A. Larabell, A.P. Alivisatos, *Nanotechnology* 14 (2003) R15.
- [8] C.M. Niemeyer, *Angew. Chem., Int. Ed.* 40 (2001) 4128.
- [9] A.P. Alivisatos, *Nat. Biotechnol.* 22 (2004) 47.
- [10] M. Bruchez, M. Moronne, P. Gin, S. Weiss, A.P. Alivisatos, *Science* 281 (1998) 2013.
- [11] W.C.W. Chan, S. Nie, *Science* 281 (1998) 2016.
- [12] B. Dubertret, P. Skourides, D.J. Norris, V. Noireaux, A.H. Brivanlou, A. Libchaber, *Science* 298 (2002) 1759.
- [13] D.R. Larson, W.R. Zipfel, R.M. Williams, S.W. Clark, M.P. Bruchez, F.W. Wise, W.W. Webb, *Science* 300 (2003) 1434.
- [14] D. Ishii, K. Kinbara, Y. Ishida, N. Ishii, M. Okochi, M. Yohda, T. Aida, *Nature* 423 (2003) 628.
- [15] J.K. Jaiswal, H. Mattoussi, J.M. Mauro, S.M. Simon, *Nat. Biotechnol.* 21 (2003) 47.
- [16] I.L. Medintz, A.R. Clapp, H. Mattoussi, E.R. Goldman, B. Fisher, J.M. Mauro, *Nat. Mater.* 2 (2003) 630.
- [17] M. Dahan, S. Levi, C. Luccardini, P. Rostaing, B. Riveau, A. Triller, *Science* 302 (2003) 442.
- [18] S.J. Rosenthal, I. Tomlinson, E.M. Adkins, S. Schroeter, S. Adams, L. Swafford, J. McBride, Y. Wang, L.J. DeFelice, R.D. Blakely, *J. Am. Chem. Soc.* 124 (2002) 4586.
- [19] R. Mahtab, H.H. Harden, C.J. Murphy, *J. Am. Chem. Soc.* 122 (2000) 14.
- [20] B. Sun, W. Xie, G. Yi, D. Chen, Y. Zhou, J. Cheng, *J. Immunol. Methods* 249 (2001) 85.
- [21] S. Pathak, S.K. Choi, N. Arnheim, M.E. Thompson, *J. Am. Chem. Soc.* 123 (2001) 4103.
- [22] E. Klarreich, *Nature* 413 (2001) 450.
- [23] P. Mitchell, *Nat. Biotechnol.* 19 (2001) 1013.
- [24] X. Michalet, F.F. Pinaud, L.A. Bentolila, J.M. Tsay, S. Doose, J.J. Li, G. Sundaresan, A.M. Wu, S.S. Gambhir, S. Weiss, *Science* 307 (2005) 538.
- [25] S. Kim, Y.T. Lim, E.G. Soltész, A.M. De Grand, J. Lee, A. Nakayama, J.A. Parker, T. Mihajlovic, R.G. Laurence, L.H. Cohn, M.G. Bawendi, J.V. Frangioni, *Nat. Biotechnol.* 22 (2004) 93.
- [26] J.K. Jaiswal, S.M. Simon, *Trends Cell Biol.* 14 (2004) 497.
- [27] I.L. Medintz, H.T. Uyeda, E.R. Goldman, H. Mattoussi, *Nat. Mater.* 4 (2005) 435.
- [28] X. Wu, H. Liu, K.N. Haley, J.A. Treddway, J.P. Larson, N. Ge, F. Peale, M.P. Bruchez, *Nat. Biotechnol.* 21 (2003) 41.
- [29] W. Cai, D.W. Shin, K. Chen, O. Gheysens, O. Cao, S.X. Wang, S.S. Gambhir, X. Chen, *Nano Lett.* 6 (2006) 669.
- [30] X. Gao, Y. Cui, R. Levenson, L. Chung, S. Nie, *Nat. Biotechnol.* 22 (2004) 969.
- [31] A.M. Derfus, W.C.W. Chan, S.N. Bhatia, *Nano Lett.* 4 (2004) 11.
- [32] C.B. Murray, D.J. Norris, M.G. Bawendi, *J. Am. Chem. Soc.* 115 (1993) 8706.
- [33] D. Gerion, F. Pinaud, S.C. Williams, W.J. Parak, D. Zanchet, S. Weiss, A.P. Alivisatos, *J. Phys. Chem. B* 105 (2001) 8861.

- [34] A.L. Rogach, D. Nagesha, J.W. Ostrander, M. Giersig, N.A. Kotov, *Chem. Mater.* 12 (2000) 2676.
- [35] T. Pellegrino, L. Manna, S. Kudera, T. Liedl, D. Koktysh, A.L. Rogach, S. Keller, J. Rädler, G. Natile, W.J. Parak, *Nano Lett.* 4 (2004) 703.
- [36] H. Fan, E.W. Leve, C. Scullin, J. Gabaldon, D. Tallant, S. Bunge, T. Boyle, M.C. Wilson, C. Brinker, J. *Nano Lett.* 5 (2005) 645.
- [37] J.M. Berg, J.L. Tymoczko, L. Stryer, *Biochemistry*, 6th ed., W.H. Freeman & Company, 2007, p. 25.
- [38] S.F. Wuister, I. Swart, v.F. Driel, S.G. Hickey, C. de Mello Donega, *Nano Lett.* 3 (2003) 503.
- [39] J. Aldana, Y.A. Wang, X. Peng, *J. Am. Chem. Soc.* 123 (2001) 8844.
- [40] H. Mattoussi, J.M. Mauro, E.R. Goldman, G.P. Anderson, V.C. Sundar, F.V. Mikulec, M.G. Bawendi, *J. Am. Chem. Soc.* 122 (2000) 12142.
- [41] H.T. Uyeda, I.L. Medintz, J.K. Jaiswal, S.M. Simon, H. Mattoussi, *J. Am. Chem. Soc.* 127 (2005) 3870.
- [42] H. Duan, S. Nie, *J. Am. Chem. Soc.* 129 (2007) 3333.
- [43] T. Nann, *Chem. Commun.* (2005) 1735.
- [44] A.M. Smith, H.W. Duan, M.N. Rhyner, G. Ruan, S. Nie, *Phys. Chem. Chem. Phys.* 8 (2006) 3895.
- [45] M.S. Nikolic, M. Krack, V. Aleksandrovic, A. Kornowski, S. Forster, H. Weller, *Angew. Chem., Int. Ed.* 45 (2006) 6577.
- [46] A.C. Wisher, I. Bronstein, V. Chechik, *Chem. Commun.* (2006) 1637.
- [47] M. Wang, N. Felorzabihi, G. Guerin, J.C. Haley, G.D. Scholes, M.A. Winnik, *Macromolecules* 40 (2007) 6377.
- [48] N.V. Tsarevsky, K. Matyjaszewski, *Macromolecules* 35 (2002) 9009.
- [49] N.V. Tsarevsky, K. Matyjaszewski, *Macromolecules* 38 (2005) 3087.
- [50] K. Matyjaszewski, T.P. Davis, *Handbook of Radical Polymerization*, John Wiley & Sons, Inc., Hoboken, 2002.
- [51] W. Jiang, S. Mardyani, H. Fischer, W.C.W. Chan, *Chem. Mater.* 18 (2006) 872.
- [52] K.T. Yong, J. Qian, I. Roy, H.H. Lee, E.J. Bergey, K.M. Trampusch, S. He, M.T. Swihart, A. Maitra, P.N. Prasad, *Nano Lett.* 7 (2007) 761.
- [53] K.A. Davis, B. Charleux, K. Matyjaszewski, *J. Polym. Sci. A: Polym. Chem.* 38 (2000) 2274.
- [54] P.J. Flory, *Principles of Polymer Chemistry*, Cornell University Press, 1953, p. 51.
- [55] P.C. Jocelyn, *Methods Enzymol.* 143 (1987) 246.

Protein Nanospheres: Synergistic Nanoplatform-Based Probes for Multimodality Imaging

Michael A. McDonald^a, Paul C. Wang^b, Eliot L. Siegel^c

^aMaterial Measurement Laboratory, National Institute of Standards and Technology (NIST), 100 Bureau Drive, Gaithersburg, MD 20899-8313; ^bDepartment of Radiology, Howard University, 2041 Georgia Avenue, NW, Washington, DC 20060; ^cDepartment of Radiology, Baltimore VA Medical Center and the University of Maryland, 10 North Greene Street Baltimore, MD 21201

ABSTRACT

No single clinical imaging modality has the ability to provide both high resolution and high sensitivity at the anatomical, functional and molecular level. Synergistically integrated detection techniques overcome these barriers by combining the advantages of different imaging modalities while reducing their disadvantages. We report the development of protein nanospheres optimized for enhancing MRI, CT and US contrast while also providing high sensitivity optical detection. Transferrin protein nanospheres (TfpNS), silicon coated, doped rare earth oxide and rhodamine B isothiocyanate nanoparticles, $\text{Si}\square\text{Gd}_2\text{O}_3\text{:Eu,RBITC}$, (NP) and transferrin protein nanospheres encapsulating $\text{Si}\square\text{Gd}_2\text{O}_3\text{:Eu,RBITC}$ nanoparticles (TfpNS-NP) were prepared in tissue-mimicking phantoms and imaged utilizing various cross-sectional imaging modalities. Preliminary results indicate a 1:1 NP to TfpNS ratio in TfpNS-NP and improved sensitivity of detection for MRI, CT, US and fluorescence imaging relative to its component parts and/or many commercially available contrast agents.

Keywords: Protein nanospheres, multimodal imaging, gene delivery, nanoplatform, synergistic

1. INTRODUCTION

Single-modality imaging methods are often not sufficient for the elucidation of disease etiology¹. Synergistic imaging allows more useful clinical information to be obtained via the combination of two or more modalities than may be obtained from the individual component images². The unique attributes of each technique often has the potential to provide anatomical, function and/or molecular information that complements the other imaging modalities³. The physico-chemical interactions involving each imaging method and their contrast agents may differ however. Positron Emission Tomography/Computed Tomography (PET/CT) has been the most useful clinical example of synergistic imaging. It provides excellent lesion localization via anatomical/functional registration, distinction between physiological and pathological uptake, and shorter PET scan time by using CT for attenuation correction⁴. However, cost, radioisotope preparation issues, challenges associated with image co-registration, and increased ionizing radiation dose resulting from both radionuclide and X-ray exposure highlight the need for the development of alternatives. The main advantage of using multiple modalities for imaging is the potential to combine optimal sensitivity and specificity of disease detection with high spatial resolution. High sensitivity imaging methods such as PET and Single Photon Emission Computed Tomography (SPECT), which have poor spatial resolution, must often be combined with high resolution techniques such as Magnetic Resonance Imaging (MRI), CT and Ultrasound (US), which have poor sensitivity and specificity of disease detection. Integration of optical techniques with these conventional medical imaging methods should increase sensitivity, specificity, spatial resolution and provide lower cost options for the detection, monitoring and treatment of disease⁵.

[illegible]

An important step in being able to compare imaging results is the development of multimodality imaging agents capable of providing contrast across several imaging modalities simultaneously. It is desirable that these agents act synergistically in providing optimal image enhancement in each imaging modality ⁶. In so doing, these agents could potentially function as imaging reference standards, facilitating image comparison via probe co-localization, simplified image co-registration and decreased intra- and inter-modality variability ⁷. Improved sensitivity of probe detection may also result in the use of less contrast material ⁸. This could decrease toxicity and lead to reduced ionizing radiation dose/exposure during procedures such as X-ray CT due to improved certainty of probe location ⁹.

Numerous dual-modality imaging agents have been reported in the literature, exploiting MRI-optical ¹⁰, PET-optical ¹¹, SPECT-optical ¹² and PET-MRI ¹³ technologies. These agents often combine the use of paramagnetic gadolinium chelates, organic dyes, metallic gold nanoparticles, semiconducting quantum dots and magnetic nanoparticles into single probes ¹⁴. Molecular targeting is often accomplished by conjugation of the imaging agents to macromolecules such as DNA, peptides and antibodies as well as viruses and carbon nanotubes ^{15, 16}. Towards this aim we have developed a prototype multimodality contrast agent, transferrin protein nanospheres (TfpNS) encapsulating silicon coated, doped rare earth oxide and rhodamine B isothiocyanate nanoparticles (Si-Gd₂O₃:Eu,RBITC), TfpNS-NP. In previous studies we demonstrated enhanced specificity for transferrin receptor-mediated uptake and gene delivery in cancer cells *in vitro* utilizing transferrin protein nanospheres ¹⁷. In the present study phantoms were constructed to test the utility of a single probe, TfpNS-NP, in enhancing MRI, CT, US and fluorescent imaging contrast. These preliminary studies also investigate whether TfpNS-NP can improve sensitivity for probe detection utilizing conventional imaging modalities and fluorescence imaging.

2. MATERIALS AND METHODS

2.1 Contrast Agent Synthesis

Briefly, the $\text{Si-Gd}_2\text{O}_3\text{:Eu,RBITC}$ NP was synthesized via a modification of methods by Louis et. al.^{18,*}. 0.1 mol/L Gd (95%) and Eu (5%) in the presence of 13 mg RBITC was prepared in DEG salt and precipitated versus 3 mol/L NaOH at high temperature (140° C for 1 hr, 180° C for 4 hr). Activation via 0.1 M TEA aqueous solution followed by 88.5 uL APTES and 66.8 uL TEOS at low temperature facilitated formation of a polysiloxane shell around the $\text{Gd}_2\text{O}_3\text{:Eu,RBITC}$ core. Subsequent dialysis against ethanol and water provided the purified final product. Transferrin was purchased from Athens Research & Technology (Athens, GA). Unlabeled transferrin protein nanospheres (TfpNS) and TfpNS-NP were synthesized via ultrasonic irradiation at 70 W/cm² and modification of methods previously described in detail¹⁹.

2.2 Contrast Agent Characterization

Samples for AFM were imaged with a Bioscope II atomic force microscope (Veeco, Santa Barbara, CA) on a silicon substrate. AFM images were collected in tapping mode using silicon tips (Veeco) at resonance frequencies of 200 kHz - 300 kHz. Images were collected at a scan rate of 1 Hz and captured an 8 X 8 micron image, 2048 X 2048 pixels. The theoretical x,y resolution is 3.9 nm and Z resolution is 0.5 nm. AFM images were flattened and plane-fit before image analysis. All images were collected under ambient conditions. TfpNS and TfpNS-NP size and zeta potential were determined by dynamic laser light scattering (DLS) using a ZetaPALS particle size analyzer (Brookhaven Instruments, Holtsville, NY). Measurements were performed at 25°C in aqueous solution. Absorbance and fluorescence spectra were obtained using Carey Eclipse spectrometers (Varian, Palo Alto, CA). Gadolinium concentration was determined with the semi-quantitative mode of an Agilent model 7500cs inductively coupled plasma mass spectroscopy (Agilent Technologies, Santa Clara, CA).

2.3 Phantom Preparation

Phantoms were utilized in order to decrease variability secondary to NP agglomeration and facilitate image comparison. A dilution series of each contrast agent (TfpNS, NP and TfpNS-NP as well as control samples) was prepared in 8% gelatin in either eppendorf tubes for MRI and CT experiments or in a 24-well plate for optical imaging. Typically, the gelatin solution was heated to 95° C with stirring until it clarified. It was next cooled to 55°C with stirring and aliquoted with the appropriate concentration of contrast agent into eppendorf tubes. The tubes were then vortexed and placed in a refrigerator for faster cooling. Similarly, the still-liquid gelatin solution and contrast agents were then poured into 24-well plates and rapidly cooled in a refrigerator. Phantoms for US imaging were prepared by heating 4% agarose to 95°C in a waterbath with stirring, pouring it into a 250 mL container and leaving a void tube (a lithium greased metal rod) in place to make a 6 mL void volume²⁰. The agarose was hardened in a refrigerator. Subsequently contrast agent in 8% gelatin, prepared as above, was poured into the agarose void volume. The gelatin/contrast agent inclusions were then hardened in a refrigerator. All imaging experiments utilizing phantoms were conducted with sample and measurement numbers of at least n = 3 and error less than 4% unless otherwise noted in the text.

2.4 Magnetic Resonance Experiments

MRI was acquired using a Philips Achieva 1.5T SE (Philips Medical Systems, Andover MA). A spin-echo (SE) imaging sequence was used to obtain T1-weighted images. The imaging parameters were as follows: echo time (TE) 15 milliseconds, repetition time (TR) 434 milliseconds, Flip angle 69°, slice thickness 3.0 mm, field of view 200 mm, zoom 328%, 256 X 256, 20 frames. A turbo spin echo (TSE) imaging sequence was utilized for T2 experiments. The T2 measurement parameters were as follows: TE 100 milliseconds, TR 3.2 seconds, Flip angle 90°, slice thickness 3.0 mm, field of view 220 mm, zoom 205%, 256 X 256, 20 frames. A Philips 8 Channel SENSE Head Coil was used for both T1 and T2 imaging experiments.

* Disclaimer: The full description of the procedures used in this paper requires the identification of certain commercial products and their suppliers. The inclusion of such information should in no way be construed as indicating that such products or suppliers are endorsed by NIST or are recommended by NIST or that they are necessarily the best materials, instruments, software or suppliers for the purposes described.

2.5 Computed Tomography Experiments

Experiments were performed to determine the relative CT attenuation of the NP. The Gd containing contrast agent MultiHance was used for comparison of X-ray attenuation. Data were acquired at ambient temperature. Samples were positioned in the center of the gantry of a Siemens Somatom Definition Flash CT scanner (Siemens, Baltimore MD) and imaged under the following constant scanning parameters: slice thickness 0.750 mm, 120 keV, 220 mA, scan time 1 second, 300 mm field of view, W: 100 L: 45. Attenuation measurements were recorded as mean Hounsfield units obtained from region-of-interest squares approximately 300 mm² using syngo CT software and plotted against contrast agent concentration using linear regression analysis.

2.6 Ultrasound Experiments

Ultrasound imaging experiments were conducted with a ATL HDI® 4000 Ultrasound System in 2D imaging mode, 256 (8 bits) greyscale, Two different ultrasound transducers were used for imaging studies: 1) a 5-2 MHz curvilinear array transducer and 2) a 12-5 MHz 256 element high resolution linear array transducer. Both were operated at a MI of 0.7 and 13 Hz frame acquisition rate.

2.7 Fluorescence Imaging Experiments

The contrast agents were quantified with respect to fluorescent intensity (radiance, photons/s/cm²/sr) using a Caliper IVIS Spectrum imaging system (Caliper Life Sciences, Hopkinton, MA) with excitation/emission filters at 570/620 nm and the following parameters: 5 second exposure, F/stop = 2, binning = 16 pixels per superpixel, manual focus @ 0.5cm above stage, FOV = 12.9cm.

3. RESULTS AND DISCUSSION

3.1 Contrast Agent Characterization

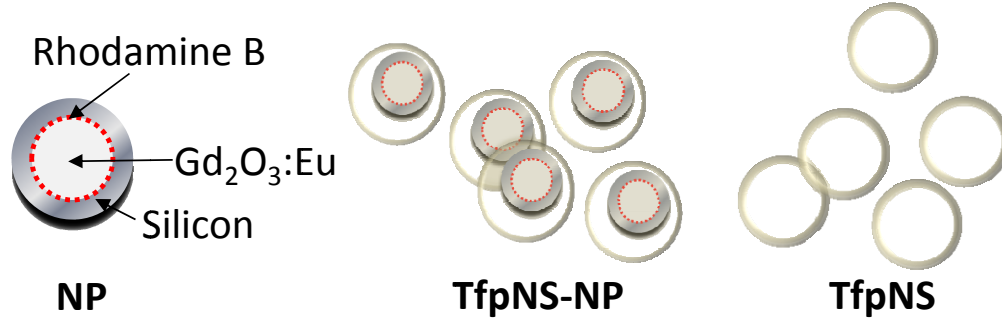


Fig. 1. Schematic depicting experimental contrast agents: Si-Gd₂O₃:Eu,RBITC nanoparticles (NP), transferrin protein nanospheres (TfpNS) and transferrin protein nanospheres encapsulating Si-Gd₂O₃:Eu,RBITC nanoparticles (TfpNS-NP).

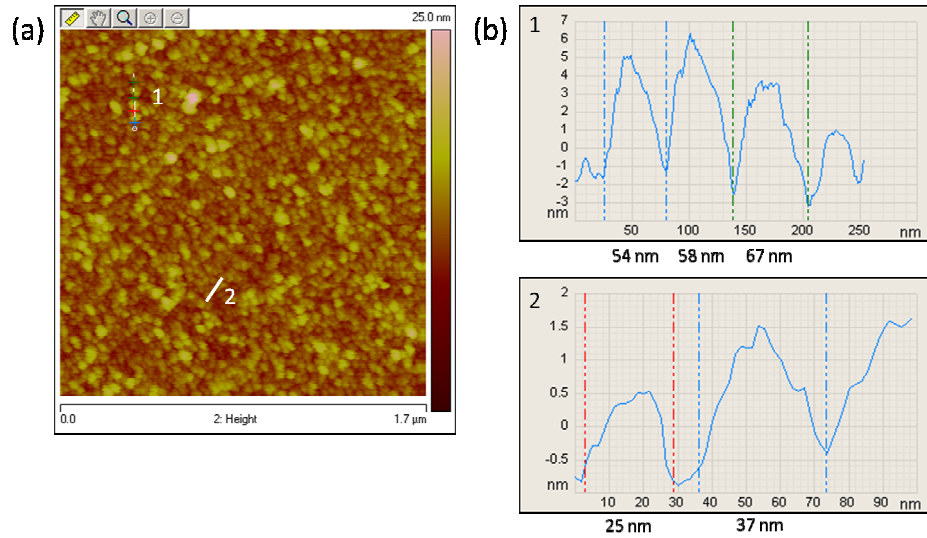


Fig. 2. A representative Atomic Force Microscope scan of multiple Si-Gd₂O₃:Eu,RBITC nanoparticles (NPs) (a) with detailed AFM size distribution data of five NPs (b).

Table 1. Summary of Characterization Results for Si-Gd₂O₃:Eu,RBITC nanoparticles (NP), transferrin protein nanospheres (TfpNS) and transferrin protein nanospheres encapsulating Si-Gd₂O₃:Eu,RBITC nanoparticles (TfpNS-NP)

	NP (Si-Gd ₂ O ₃ :Eu,RhB)	TfpNS-NP	TfpNS
Gd, Eu Concentration (ICP-MS)	Gd=0.31 mg/mL Eu=0.025 mg/mL	Gd=0.25 mg/mL Eu=0.020 mg/mL	
UV-Vis	550-590 nm	550-590 nm	280nm
Fluorescence	580-700 nm	580-700 nm	
DLS	(unstable, micron sized)	63-80 nm	79-91 nm
ZetaPotential @ pH 7.4	2.06 ± 0.97 mV	-45.05 ± 7.39 mV	-47.37 ± 0.87 mV
AFM	25-68nm		

As indicated in Table 1, the NP has a positive zeta potential at pH 7.4 making it more likely to agglomerate in solution²¹. NP agglomeration was further substantiated by DLS and AFM studies (Fig. 2). Both TfpNS and TfpNS-NP have negative zeta potentials larger than -30 mV at physiological pH, favoring dispersion in solution. Experiments conducted in which NP was added to TfpNS did not result in a change in zeta potential until more than 3/4 of the volume contained NP, at which point a precipitous increase in charge was observed. Similarly, adding TfpNS to NP did not initially result in a change in zeta potential. These results support the hypothesis that the NP is encapsulated within TfpNS in the case of TfpNS-NP. Size and charge analysis (as determined by DLS and AFM measurements) indicate that it is likely that the NP to protein ratio in TfpNS-NP is 1:1. We are currently exploring the use of flow cytometry to differentiate and/or separate NP (positively charged and strongly fluorescent) from TfpNS-NP (negatively charged and strongly fluorescent) and TfpNS (negatively charged and weakly fluorescent) and as means of improved characterization.

3.2 Magnetic Resonance Experiments

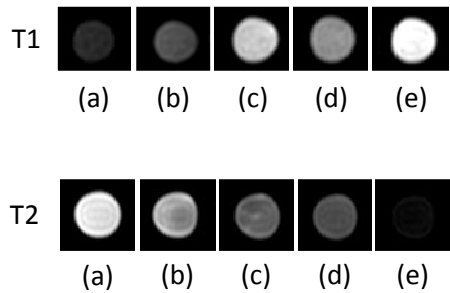


Fig. 3. T1- and T2-weighted magnetic resonance images of phantoms containing SiC-Gd₂O₃:Eu,RBITC nanoparticles (NP) at a Gd concentration of 0 mM (a), 0.002 mM (b), 0.050 mM (c), 0.200 mM (d), and 0.500 mM (e). The NPs were suspended in 8% gelatin.

Table 2. Mean T1 and T2 ± SD values calculated from phantoms (n = 3) containing SiC-Gd₂O₃:Eu,RBITC nanoparticles (NP) in 8% gelatins at ambient temperature.

	0 mM Gd	0.002 mM Gd	0.05 mM Gd	0.20 mM Gd	0.5 mM Gd
T1 (msec ± SD)	156 ± 14.5	255 ± 21	605 ± 33	454 ± 24	758 ± 66
T2 (msec ± SD)	667 ± 31	472 ± 63	310 ± 32	260 ± 15	78 ± 11

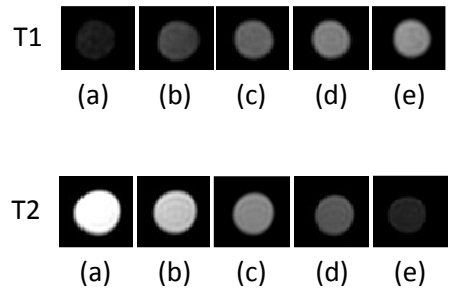


Fig. 4. T1- and T2-weighted magnetic resonance images of phantoms containing transferrin protein nanospheres encapsulating SiC-Gd₂O₃:Eu,RBITC nanoparticles (TfpNS-NP) at a Gd concentration of 0 mM (a), 0.002 mM (b), 0.040 mM (c), 0.200 mM (d), and 0.400 mM (e). The TfpNS-NPs were suspended in 8% gelatin.

Table 3. Mean T1 and T2 ± SD values calculated from phantoms (n = 3) containing transferrin protein nanospheres encapsulating SiC-Gd₂O₃:Eu,RBITC nanoparticles (TfpNS-NP) in 8% gelatins at ambient temperature.

	0 mM Gd	0.002 mM Gd	0.04 mM Gd	0.16 mM Gd	0.4 mM Gd
T1 (msec ± SD)	349 ± 44	671 ± 57	949 ± 142	1130 ± 194	1263 ± 203
T2 (msec ± SD)	2270 ± 113	1753 ± 82	1240 ± 54	853 ± 46	433 ± 38

Representative T1- and T2-weighted MR images of TfpNS and NP are shown in Fig. 3 and 4. At the relatively low Gd concentrations studied, a nonlinear increase in T1 and T2 signal intensity with increasing NP and TfpNS-NP concentration was observed (Tables 2 and 3). However, despite this non-linearity, the possibility of detecting less than 0.04 mM gadolinium in TfpNS-NP is demonstrated. This represents a significant improvement in sensitivity of probe detection in comparison to many commercially available MRI contrasts agents²². TfpNS-NP exhibit a larger increase in T1 and T2 relaxation than either the NP or MultiHance, a clinically used MRI contrast agent, when matched for NP concentration and/or gadolinium concentration. This may be due to the increased rotational correlation time associated with the size of the NP and encapsulation of the NP within TfpNS, which is anticipated to have an effect on local viscosity²³. Prolonged water residence time proximal to the gadolinium oxide nucleus²⁴, due to water compartmentalization/sequestration within the protein nanosphere, may also influence the relaxation rate. Relaxivity as a function of time, r_1 and r_2 , were estimated via a non-linear model²⁵. r_1 and r_2 were 28.6 and 38.0 s⁻¹ mM⁻¹, respectively, for TfpNS-NP and 11.3 and 18.8 s⁻¹ mM⁻¹, respectively for the NP. MultiHance when prepared in the same manner had r_1 and r_2 values of 6.4 and 7.3 s⁻¹ mM⁻¹, respectively. This difference from the manufacturer reported values²² may be due to our measurements having been conducted in 8% gelatin and/or variability associated with preparation of the gelatin phantoms i.e., evaporation of water during phantom preparation. The presence of varying amounts of water was shown to exert a significant influence on 1/T1 and 1/T2 even in the absence of contrast media.

3.3 Computed Tomography Experiments

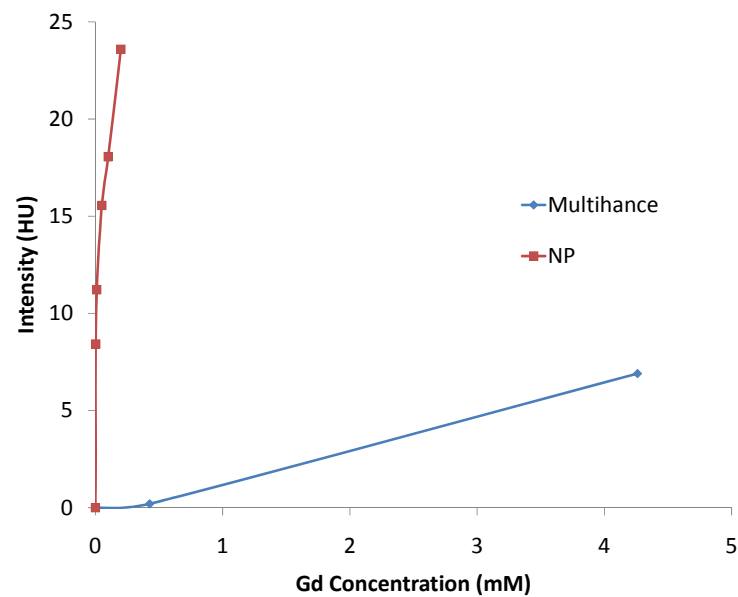


Fig. 5. SiC₂Gd₂O₃:Eu,RBITC nanoparticles (NP) and MultiHance X-ray CT attenuation (HU) plotted as a function of gadolinium concentration. Both agents were suspended in 8% gelatin.

A plot of X-ray CT attenuation (HU) versus gadolinium concentration (Fig. 5) demonstrates the potential for detection of the NP at a concentration of less than 0.2 mM gadolinium. Iodine-based contrast agents are typically given to patients at molar concentration²⁶, i.e., the NP is detectable at 4 orders of magnitude lower contrast agent concentration than is used clinically. On an equimolar basis, gadolinium exhibits approximately double the X-ray attenuation of iodine at 120 keV²⁷. In addition, gadolinium’s higher density (7.41 g/cm³ for gadolinium oxide vs. 2.2 g/cm³ for iodine) and the packaging of hundreds of thousands of gadolinium atoms per nanoparticle may account for the significantly greater X-ray CT attenuation observed with the NP vs. MultiHance, a monomeric gadolinium chelate. However, X-ray CT attenuation of the NP is non-linear, indicating it is poorly dispersed. Phantom variability and NP clustering (Table 1) may also contribute to the observed increase in sensitivity for detection.

3.4 Ultrasound Experiments

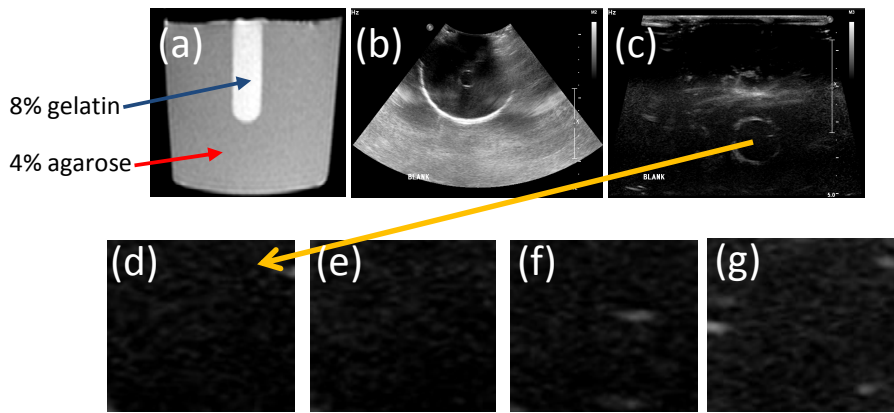


Fig. 6. Magnetic resonance (a) and ultrasound images (b-g) of gelatin/agarose phantoms in coronal view (a), axial view at 5 MHz utilizing a curvilinear ultrasound transducer (b) and at 7 MHz utilizing a linear ultrasound transducer (c). An arrow originating from the 8% gelatin inclusion (c) indicates the ROI used for backscatter determination in a control phantom (d) and phantoms containing $\text{Si}\text{-}\text{Gd}_2\text{O}_3\text{:Eu,RBITC}$ nanoparticles (NP) (e), transferrin protein nanospheres (TfpNS) (f) and transferrin protein nanospheres encapsulating $\text{Si}\text{-}\text{Gd}_2\text{O}_3\text{:Eu,RBITC}$ nanoparticles (TfpNS-NP) (g). The gadolinium concentration for the NP (e) and TfpNS-NP (g) is 0.200 mM. TfpNS and TfpNS-NP were prepared at equivalent protein nanosphere concentration (as indicated by A_{280} protein concentration measurements).

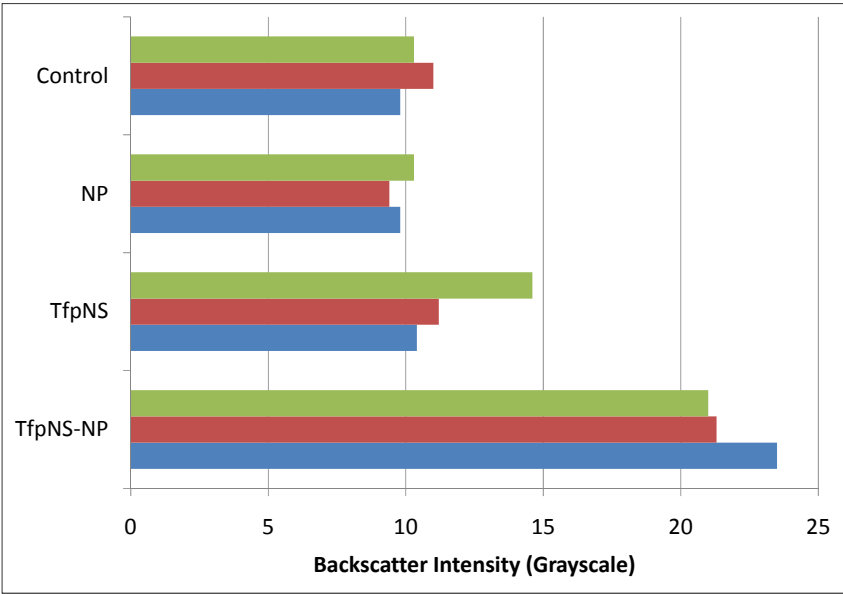


Fig. 7. Ultrasound backscatter intensity at 7 MHz of control phantoms and phantoms containing $\text{Si}\text{-}\text{Gd}_2\text{O}_3\text{:Eu,RBITC}$ nanoparticles (NP), transferrin protein nanospheres (TfpNS) and transferrin protein nanospheres encapsulating $\text{Si}\text{-}\text{Gd}_2\text{O}_3\text{:Eu,RBITC}$ nanoparticles (TfpNS-NP). The gadolinium concentration for the NP and TfpNS-NP is 0.200 mM. TfpNS and TfpNS-NP were prepared at equivalent protein nanosphere concentration (as indicated by A_{280} protein concentration measurements).

Fig. 6 demonstrates the 2-fold increase in US backscatter at 7 MHz observed for TfpNS-NP relative to TfpNS, NP and a control. The experiments controlled for NP and protein nanosphere concentration making it more likely that an interaction between the NP and the wall of the protein nanosphere accounts for the increased signal intensity seen in TfpNS-NP. In previous studies we investigated the use of protein (sub)microspheres as US, optical and photoacoustic imaging agents¹⁷. The present experiment demonstrates the utility of NP encapsulation within TfpNS. In addition to providing high specificity for disease targeting and a means of delivering therapeutic genes and drugs into cells, encapsulation of the NP is essential for extending the functionality of protein nanospheres to US imaging.

3.5 Fluorescence Imaging Experiments

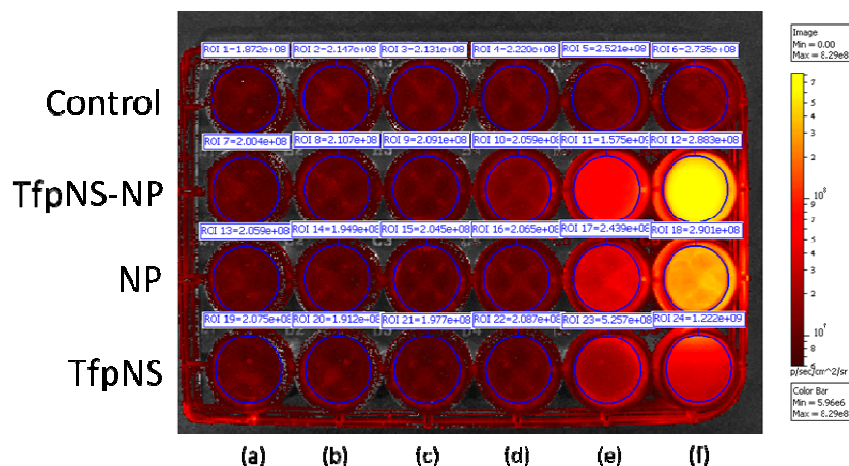


Fig. 8. Sample image from a 24-well plate containing 8% gelatin (control), 8% gelatin and transferrin protein nanospheres encapsulating $\text{Si}\text{--}\text{Gd}_2\text{O}_3\text{:Eu,RBITC}$ nanoparticles (TfpNS-NP), $\text{Si}\text{--}\text{Gd}_2\text{O}_3\text{:Eu,RBITC}$ nanoparticles (NP), and transferrin protein nanospheres (TfpNS). The gadolinium concentrations in the TfpNS-NP and NP rows are 0 mM (a), 1.59×10^{-5} mM (b), 1.59×10^{-4} mM (c), 1.59×10^{-3} mM (d), 1.59×10^{-2} mM (e) and 1.59×10^{-1} mM (f). TfpNS and TfpNS-NP were prepared at equivalent protein nanosphere concentration (as indicated by A_{280} protein concentration measurements).

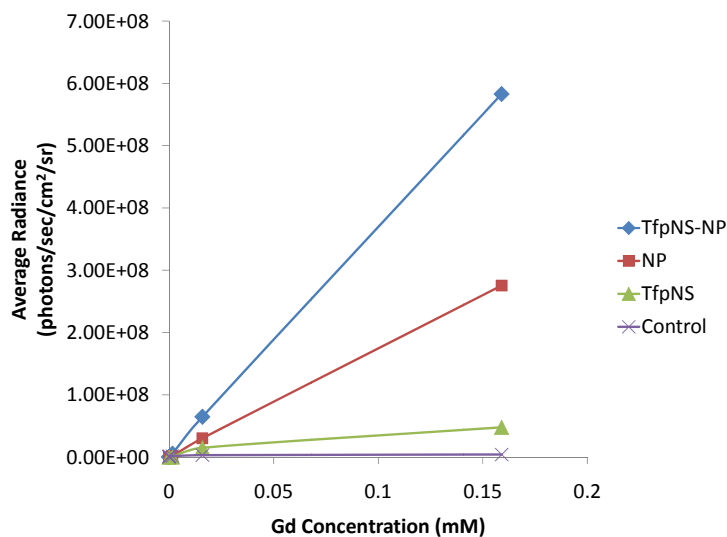


Fig. 9. Plot of fluorescence intensity (expressed as the average radiance) versus Gd concentration from a 24-well plate containing 8% gelatin and transferrin protein nanospheres encapsulating $\text{Si}\text{--}\text{Gd}_2\text{O}_3\text{:Eu,RBITC}$ nanoparticles (TfpNS-NP), $\text{Si}\text{--}\text{Gd}_2\text{O}_3\text{:Eu,RBITC}$ nanoparticles (NP), transferrin protein nanospheres (TfpNS) and a control. TfpNS and TfpNS-NP were prepared at equivalent protein nanosphere concentration (as indicated by A_{280} protein concentration measurements)

Fig. 9 demonstrates linear increase in fluorescence intensity observed with increasing NP and TfpNS-NP concentration. Among the potential advantages of using NPs vs. dye molecules, such as RBITC, for optical bioimaging are broader spectrum excitation, longer fluorescence lifetime, decreased quenching, and lower cytotoxicity; all of which are influenced by the protection of RBITC (and $\text{Gd}_2\text{O}_3:\text{Eu}$) within the porous silicon structure²⁸. TfpNS-NPs exhibit 3-fold greater fluorescence intensity relative to the NP although matched for NP and gadolinium concentration. The overall sensitivity for detection utilizing fluorescence imaging is greater than 2×10^{-8} M gadolinium. The cause for TfpNS-NPs increased fluorescence signal relative to the NP is still under investigation. A broadened increase in TfpNS fluorescence intensity is observed between 300 nm and 500 nm. This may correspond to the intrinsic fluorescence of native transferrin reported by other investigators²⁹. It is possible that intrinsic fluorescence contributes to both the TfpNS fluorescence signal observed in Fig. 8 and 9 and to the increased signal intensity seen for TfpNS-NP as compared to NP despite equivalent NP concentration. We are actively investigating a means of quantifying the contribution of RBITC versus europium doping/trivalent lanthanide ion luminescence ($\text{Gd}_2\text{O}_3:\text{Eu}$) to NP fluorescence.

4. CONCLUSIONS

In conclusion we have developed a multimodal imaging contrast agent, TfpNS-NP, capable of permitting high sensitivity of probe detection utilizing MRI, CT, US and optical imaging with a single contrast injection. These preliminary studies represent an attempt to characterize imaging sensitivity in advance of initiating toxicity and probe metabolism/excretion studies. As little as 10^{-5} M Gd can be detected by MRI, 10^{-4} M Gd by X-ray CT and 10^{-8} M Gd by fluorescence imaging. In addition, there is a 2-fold increase in TfpNS-NP US backscatter relative to the agents' component parts (NP and TfpNS). Because the probe itself is the targeting moiety protein nanospheres represent a unique and flexible imaging and therapeutic nanoplatform. They may be easily rerouted to diverse disease types simply by creating protein nanospheres from protein disease markers capable of binding to their respective ligand/receptor. In addition to providing a means of delivering nanoparticles, drugs and genes to specific cells it is anticipated that nanomaterials that closely mimic endogenous proteins, such as protein nanospheres, may eventually play a role in monitoring protein metabolism *in vivo*, serving as an entry point for the integration of proteomics and personalized medicine into multimodal molecular imaging³⁰.

ACKNOWLEDGEMENTS

The authors would like to acknowledge Dr. Lee Yu, Material Measurement Laboratory, NIST for the ICP-MS analysis and for his generosity of time; Dr. Tighe A. Spurlin, formerly of NIST, for sharing his expertise in AFM measurements; and the Radiology staff at the Baltimore VA Medical Center for their enthusiasm for the project and assistance with US, CT and MRI. This research is partially supported by the DOD USAMRMC W81XWH-10-1-0767 and the NIH/NCRR/RCMI 2G12 RR003048 grants.

REFERENCES

1. Frangioni, J.V. New technologies for human cancer imaging. *J Clin Oncol* **26**, 4012-4021 (2008).
2. Maisey, M.N., Hawkes, D.J. & Lukawieck-Vydelingum, A.M. Synergistic imaging. *European journal of nuclear medicine* **19**, 1002-1005 (1992).
3. Seevinck, P.R. et al. Factors affecting the sensitivity and detection limits of MRI, CT, and SPECT for multimodal diagnostic and therapeutic agents. *Anti-cancer agents in medicinal chemistry* **7**, 317-334 (2007).
4. Seemann, M.D. Whole-body PET/MRI: the future in oncological imaging. *Technology in cancer research & treatment* **4**, 577-582 (2005).
5. Ntziachristos, V., Ripoll, J., Wang, L.V. & Weissleder, R. Looking and listening to light: the evolution of whole-body photonic imaging. *Nature biotechnology* **23**, 313-320 (2005).
6. Cheon, J. & Lee, J.H. Synergistically integrated nanoparticles as multimodal probes for nanobiotechnology. *Accounts of chemical research* **41**, 1630-1640 (2008).
7. Abdelmoez, A.A. et al. Albumin-based nanoparticles as magnetic resonance contrast agents: II. Physicochemical characterisation of purified and standardised nanoparticles. *Histochemistry and cell biology* **134**, 171-196 (2010).
8. Smith, A.M., Ruan, G., Rhyner, M.N. & Nie, S. Engineering luminescent quantum dots for in vivo molecular and cellular imaging. *Annals of biomedical engineering* **34**, 3-14 (2006).
9. Hasebroock, K.M. & Serkova, N.J. Toxicity of MRI and CT contrast agents. *Expert opinion on drug metabolism & toxicology* **5**, 403-416 (2009).
10. Jennings, L.E. & Long, N.J. 'Two is better than one'--probes for dual-modality molecular imaging. *Chemical communications (Cambridge, England)*, 3511-3524 (2009).
11. Sevick-Muraca, E.M. & Rasmussen, J.C. Molecular imaging with optics: primer and case for near-infrared fluorescence techniques in personalized medicine. *Journal of biomedical optics* **13**, 041303 (2008).
12. Cai, W. & Chen, X. Nanoplatforms for targeted molecular imaging in living subjects. *Small (Weinheim an der Bergstrasse, Germany)* **3**, 1840-1854 (2007).
13. Xie, J. et al. PET/NIRF/MRI triple functional iron oxide nanoparticles. *Biomaterials* **31**, 3016-3022 (2010).
14. Lee, S. & Chen, X. Dual-modality probes for in vivo molecular imaging. *Mol Imaging* **8**, 87-100 (2009).
15. de la Zerda, A. et al. Ultrahigh sensitivity carbon nanotube agents for photoacoustic molecular imaging in living mice. *Nano letters* **10**, 2168-2172 (2010).
16. Kobayashi, H. & Choyke, P.L. Target-Cancer-Cell-Specific Activatable Fluorescence Imaging Probes: Rational Design and in Vivo Applications. *Accounts of chemical research* **Epub ahead of print** (2010).
17. McDonald, M.A., Spurlin, T.A., Tona, A., Elliott, J.T., Halter, M., Plant, A.L. Transferrin protein nanospheres: a nanoplatform for receptor-mediated cancer cell labeling and gene delivery. *Proc. SPIE* **7576**, 1-12 (2010).
18. Fizet, J. et al. Multi-luminescent hybrid gadolinium oxide nanoparticles as potential cell labeling. *Journal of nanoscience and nanotechnology* **9**, 5717-5725 (2009).

19. McDonald, M.A., Jankovic, L., Shahzad, K., Burcher, M. & Li, K.C. Acoustic fingerprints of dye-labeled protein submicrosphere photoacoustic contrast agents. *Journal of biomedical optics* **14**, 034032 (2009).
20. Madsen, E.L. et al. Tissue-mimicking oil-in-gelatin dispersions for use in heterogeneous elastography phantoms. *Ultrasonic imaging* **25**, 17-38 (2003).
21. Faure, A.C. et al. Control of the in vivo biodistribution of hybrid nanoparticles with different poly(ethylene glycol) coatings. *Small (Weinheim an der Bergstrasse, Germany)* **5**, 2565-2575 (2009).
22. Laurent, S., Elst, L.V. & Muller, R.N. Comparative study of the physicochemical properties of six clinical low molecular weight gadolinium contrast agents. *Contrast media & molecular imaging* **1**, 128-137 (2006).
23. Nicolle, G.M., Toth, E., Eisenwiener, K.P., Macke, H.R. & Merbach, A.E. From monomers to micelles: investigation of the parameters influencing proton relaxivity. *J Biol Inorg Chem* **7**, 757-769 (2002).
24. Zech, S.G., Eldredge, H.B., Lowe, M.P. & Caravan, P. Protein binding to lanthanide(III) complexes can reduce the water exchange rate at the lanthanide. *Inorganic chemistry* **46**, 3576-3584 (2007).
25. Landis, C.S. et al. Determination of the MRI contrast agent concentration time course in vivo following bolus injection: effect of equilibrium transcytolemmal water exchange. *Magn Reson Med* **44**, 563-574 (2000).
26. Rutten, A. & Prokop, M. Contrast agents in X-ray computed tomography and its applications in oncology. *Anti-cancer agents in medicinal chemistry* **7**, 307-316 (2007).
27. Thomsen, H.S., Almen, T. & Morcos, S.K. Gadolinium-containing contrast media for radiographic examinations: a position paper. *European radiology* **12**, 2600-2605 (2002).
28. Tan, W. et al. Bionanotechnology based on silica nanoparticles. *Medicinal research reviews* **24**, 621-638 (2004).
29. James, N.G. et al. Intrinsic fluorescence reports a global conformational change in the N-lobe of human serum transferrin following iron release. *Biochemistry* **46**, 10603-10611 (2007).
30. Coto-Garcia, A.M. et al. Nanoparticles as fluorescent labels for optical imaging and sensing in genomics and proteomics. *Analytical and bioanalytical chemistry* **399**, 29-42 (2011).

Review Article

Bacterial Magnetosome: A Novel Biogenetic Magnetic Targeted Drug Carrier with Potential Multifunctions

Jianbo Sun,¹ Ying Li,² Xing-Jie Liang,^{3,4} and Paul C. Wang⁵

¹ Department of Microbiology and Immunology, College of Physicians and Surgeons, Columbia University, New York, NY 10032, USA

² State Key Laboratories for Agro-biotechnology and College of Biological Sciences, China Agricultural University, Beijing 100193, China

³ Laboratory of Nanomedicine and Nanosafety, Division of Nanomedicine and Nanobiology, National Center for Nanoscience and Technology, Beijing 100190, China

⁴ CAS Key Laboratory for Biomedical Effects of Nanomaterials and Nanosafety, Chinese Academy of Sciences, Beijing 100190, China

⁵ Laboratory of Molecular Imaging, Department of Radiology, Howard University, Washington, DC 20060, USA

Correspondence should be addressed to Xing-Jie Liang, liangxj@nanoctr.cn and Paul C. Wang, pwang@howard.edu

Received 30 May 2011; Accepted 12 July 2011

Academic Editor: Donglu Shi

Copyright © 2011 Jianbo Sun et al. This is an open access article distributed under the Creative Commons Attribution License, which permits unrestricted use, distribution, and reproduction in any medium, provided the original work is properly cited.

Bacterial magnetosomes (BMs) synthesized by magnetotactic bacteria have recently drawn great interest due to their unique features. BMs are used experimentally as carriers for antibodies, enzymes, ligands, nucleic acids, and chemotherapeutic drugs. In addition to the common attractive properties of magnetic carriers, BMs also show superiority as targeting nanoscale drug carriers, which is hardly matched by artificial magnetic particles. We are presenting the potential applications of BMs as drug carriers by introducing the drug-loading methods and strategies and the recent research progress of BMs which has contributed to the application of BMs as drug carriers.

1. Introduction

Nanoscale drug carriers for targeted drug delivery have great potential [1–4] to resolve the issues associated with regular drug administration such as nonspecific biodistribution of pharmaceuticals; the lack of drug specific affinity and the necessity of a large dosage to achieve high local concentration; the crossing of biological barriers such as organs, cells, and intracellular bilayers; and nonspecific toxicity and other adverse side effects (immunity, neural systems, etc.) due to high drug doses [5, 6].

Pharmaceutical carriers include soluble polymers, microstructures, cell ghosts, lipoproteins, liposomes, dendrimers, micelles and so on [2–6], which can all be designed for drug delivery vehicles. Such vehicles include (a) direct application of carriers with drug into the affected zone; (b) passive drug accumulation in the tissues with leaky vasculature; (c) physiological targeting based on abnormal pH and/or temperature in the pathological zone; (d) magnetic targeting under the use of an external magnetic field; (e) intelligentized targeting

using specific molecules such as ligands or antibodies, which can recognize the targeted area and increase the affinity to it.

Magnetic-targeted drug carriers are prepared using Fe_3O_4 or Fe_2O_3 as a core and coated with biocompatible polymers for drug delivery [7–9] due to their attractive advantages for medical applications which are (a) paramagnetism for magnetic resonance imaging (MRI); (b) position altering with magnetic field; (c) hyperthermia with an external alternating magnetic field; (d) controllable size; (e) surface modification with diverse bioactive molecules; (f) nonsignificant safety concerns. This technology has evolved rapidly since the 1970s [10], although its application has been hampered by problems such as low drug loading, propensity of congregating, poor dispersion, and difficult control of microspheric shape or size [9]. Bacterial magnetosomes (BMs) [11] synthesized by magnetotactic bacteria have recently drawn great interest [12–15] as alternatives for targeting drug carriers due to their unique features such as paramagnetism, nanoscale, narrow-size distribution, and being bounded to the membrane [16–20].

2. Characterization of BMs

Magnetosomes are found in all magnetotactic bacteria and consisted of magnetic iron mineral particles and present species-specific characteristics. Magnetosomes from the same species have the same unique composition and uniform morphology with narrow-size distribution. In various magnetotactic bacteria, magnetosomes have shapes in cubo-octahedral, elongated hexagonal prismatic, and bullet-shaped morphologies (Figure 1) [16, 21–23]. Magnetosomes in most magnetotactic bacteria strains consist of magnetite, Fe_3O_4 . The Raman Spectrum of BMs from *M. gryphiswaldense* shows resemblance to Fe_3O_4 . The FTIR spectrum of BMs also shows the presence of Fe_3O_4 [24]. Typical particle sizes are 35–120 nm, however, in some locations, crystals larger than 200 nm are found. Magnetosomes, in several magnetotactic bacteria from sulfuric environments, consist of the iron-sulfide mineral greigite, Fe_3S_4 , which is ferrimagnetically ordered [16, 25].

2.1. Characterization of Magnetosome Membrane. All magnetosomes examined to date have a lipid bilayer admixed with special proteins, which is termed magnetosome membrane. The magnetosome membrane of *M. magnetotacticum* MS-1 contains neutral lipids and free fatty acids; as well as glycolipids, sulfolipids, and phospholipids (in a weight ratio of 1:4:6). The phospholipids include phosphatidylserine and phosphatidylethanolamino. There are numerous proteins detected in the magnetosome membrane which were not found in other cell membranes or soluble fractions [18]. The fatty acid and proteomic analysis of the magnetosome membrane of *M. magneticum* AMB-1 showed a striking similarity between the cytoplasmic and magnetosome membrane profiles [19, 26]. The results showed that palmitoleic acid and oleic acid account for 90% of the total fatty acids and phospholipids compose 58% of the total lipid; with phosphatidyl ethanolamino accounting for 50% of the total phospholipids. 78 identified magnetosome membrane proteins were also found to be common in the cytoplasmic membrane, several of which are related to magnetosome biosynthesis.

The magnetosome membrane of *M. gryphiswaldense* is composed of phospholipids and fatty acids, which is similar to that from outer and cytoplasmic membranes but with different proportions [20]. There are at least 18 proteins that make up the magnetosome subproteome, and most of these proteins are unique for *M. gryphiswaldense*. The FTIR spectrum of BMs has shown these membrane lipids and the amino groups [24].

Analysis of magnetosome membrane proteins in different *Desulfovibrio magneticus* strains RS-1, AMB-1, and MSR-1 indicated three magnetosome-specific proteins MamA (Mms24), MamK, and MamM. The collagen-like protein and alleged iron-binding proteins are considered to play key roles in magnetite crystal formation and are identified as specific proteins in strain RS-1. The newly identified magnetosome membrane proteins might contribute to the formation of the unique irregular, bullet-shaped crystals in the strain [27].

The presence of polarizable primary amino groups in the magnetosome membrane offers an explanation of the elevation of external pH increasing the surface negativity of magnetosome membrane. The zeta potential of BMs from *M. gryphiswaldense* in pH 7.4 buffer is -24.4 ± 4.0 mV. The zeta potential for the BMs of *M. magneticum* AMB-1 changes from -2.5 to -25.0 mV when the pH value changes from 4.0 to 7.0 [24, 28]. The biodistribution of nanosize drug carriers following intravenous administration depends heavily on particle size and surface properties such as surface charge and hydrophobicity [29, 30]. The mononuclear phagocytic system (MPS), or reticuloendothelial system (RES), mainly consists of macrophages in the liver and spleen. The RES has the ability to remove unprotected nanoparticles from the bloodstream within seconds after intravenous administration. In general nanoscale size of BMs (35–120 nm) and the negative zeta potential of BMs are good to reduce liver clearance. It has been shown that after the injection of BMs through sublingual vena; BMs were accumulated in the liver of SD rats [24].

2.2. Magnetic Properties of BMs. The analysis of the magnetic properties of magnetosomes focused on the magnetic microstructure, hysteresis, and relaxation time. Researches by various groups showed that magnetosomes from *M. Magnetotacticum* MS-1, *M. magneticum* AMB-1, *M. gryphiswaldense*, the marine vibrioid strain MV-1, and the coccoid strain MC-1 were all single-magnetic-domain particles [11, 16, 21, 31–36]. The magnetization directions of small super paramagnetic crystals were constrained by magnetic interactions with larger crystals in the magnetosome chain having predominant saturation magnetization [32]. Shape anisotropy was found to dominate magnetocrystalline anisotropy in elongated crystals, grain elongation, and separation for chains of identical magnetite grains. The inclusion of magnetic interactions was found to decrease the blocking volume, thereby increasing the range of stable single magnetic domain, a scale not attainable for chemically synthesized nanoparticles [37].

Holograms showed a coercive field of 300 Oe for *M. magnetotacticum* [38] and coercive field of 300–450 Oe for the MV-1 chain [32]. The exact value of coercive field for any given magnetosome chain is sensitive to the particle size, separation, and chain length, as well as magnetocrystalline anisotropy [31]. For aqueous suspensions of magnetosomes extracted from *M. gryphiswaldense*, the coercivity at room temperature is 0.7 kA/m, while coercivity increases to 2.6 kA/m or 6.5 kA/m by suspending magnetosomes in aqueous solution of gelatin, with subsequent particle immobilization by gelation, coercivity increases to 2.6 kA/m or 6.5 kA/m [39, 40]. Compared to 20 A/m of the commercially available ferrofluid Resovist, this extremely high value confirms the high anisotropy-related Néel relaxation time. The magnetic losses, converted into heat in hyperthermia, were determined calorimetrically to be 960 W/g at 10 kA/m and 410 kHz. This value is exceptionally large and may even exceed those of compared metallic magnetic particles such as cobalt particles, which are hardly matched by artificial magnetic particles [39, 41].

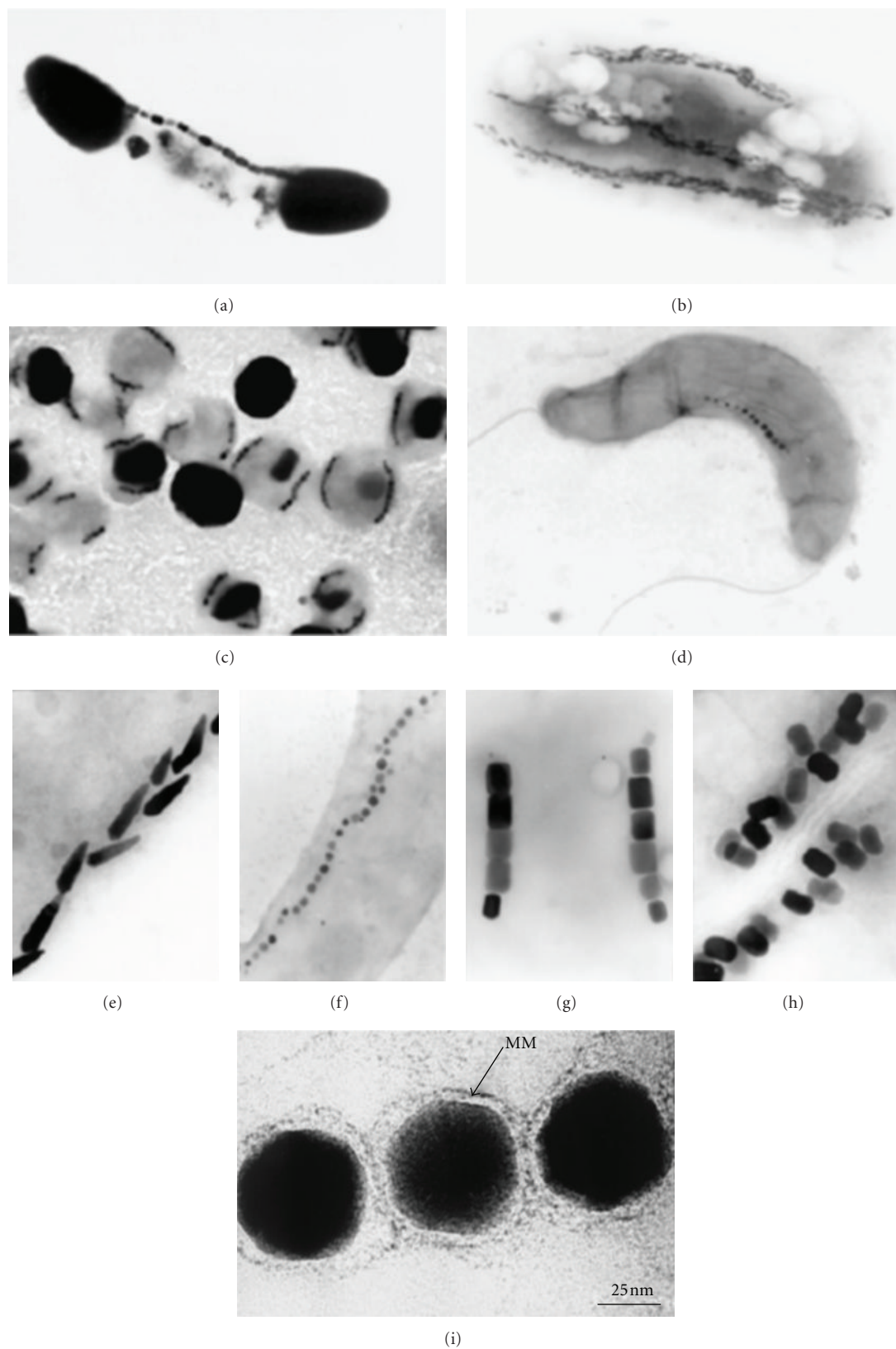


FIGURE 1: Magnetotactic bacteria with magnetosomes (a–d) and its membrane (i). Various morphologies of magnetosomes (e–h) [22, 23].

Alphandéry et al. [42] examined mechanisms of heat production by whole intact cells and extracted chains and individual magnetosomes of the magnetotactic bacterium *M. magneticum* strain AMB-1- when exposed to an oscillating magnetic field of frequency 108 kHz and field amplitudes of 23 and 88 mT. In this study, magnetosomes did not contain magnetite as the magnetite oxidized to maghemite. Intact bacterial cells that contain chains of magnetosomes, heat is generated through hysteresis losses yielding specific absorption rates of 115 ± 12 W/gFe at 23 mT and 864 ± 9 W/gFe at 88 mT. When the chains of magnetosomes are extracted from the bacterial cells and exposed to the same magnetic field, there is an additional contribution to the heat-producing mechanism due to the rotation of the magnetosomes. This contribution results in higher observed specific absorption rates of 864 ± 13 W/gFe at 23 mT and 1242 ± 24 W/gFe at 88 mT. Individual magnetosomes whose membranes had been removed produced specific absorption rate values of 529 ± 14 W/gFe at 23 mT and 950 ± 18 W/gFe at 88 mT.

Magnetotactic bacteria embedded with magnetosomes affect the T2-relaxation more greatly than T1-relaxation rate in MRI system [35] and can be used as a negative contrast agent for MRI. The physicochemical and magnetorelaxometric characterizations of bacterial magnetosomes and iron oxide nanoparticles were investigated. The longitudinal and transverse relaxivities of the magnetosomes were studied with a 1.5 T MRI system to be $R_1 = 7.688$ mmol-1s-1 and $R_2 = 147.67$ mmol-1s-1, respectively [39]. Magnetosomes in agarose gel were analyzed [43] using a 3.0 T MRI-scanner and showed T2 relaxivity of 1175 mM-1s-1, which was larger than synthetic magnetic nanoparticles with 551 mM-1s-1 and Resovists with 230 mM-1s-1. Both bacterial magnetosomes and synthetic magnetites can be used as a negative contrast agents and show slight T1 effects and strong T2 effects on MRI images. The signal attenuation of bacterial magnetite samples is more prominent than that of synthetic magnetite samples at the same concentration because bacterial magnetosomes have larger mean aggregate size, better dispersion, and stronger ferromagnetism compared to synthetic magnetites.

2.3. Biocompatibility of BMs. BMs have been predicted to be highly biocompatible because they are formed by bacterial cells rather than artificially synthesized. BMs also pose potential risks as they are nanosized particles isolated from bacterial cells and their membrane contains various nonhuman proteins [18–20, 26]. Chemical toxicity of BMs from iron ions is negligible [44, 45] due to the insolubility of Fe_3O_4 . Therefore, the toxicity of BMs may be primarily due to (a) their nanoscale size, which leads to embolism, blockage, and deposition in the body and (b) impurities, particularly proteins, nucleic acids, and polysaccharides associated with BMs extracted from bacterial cells, resulting in immunotoxicity.

Sun et al. have studied the biocompatibility of BMs and have shown the body tissue distribution and host tissue elimination following administration of BMs into the

vascular system [24] and in vitro cytotoxicity for mouse fibroblasts [46]. BMs displayed targeted distribution in SD rat liver, suggesting that BMs may be less likely to congregate than other nanoparticles; that is, BMs may avoid incurring organ congestion or infarction in vivo since they can be transferred from the sublingual vein to the liver. Purified and sterilized magnetosomes were found to be nontoxic to mouse fibroblasts in vitro. The injection of 1 mg BMs did not increase body temperature of rabbits during the pyrogen test, which showed antigens or pyrogens free with BMs administration [47].

The biocompatibility of purified magnetosomes was also evaluated comprehensively by Sun et al. It was found that magnetosomes showed slight acute toxicity, immune toxicity, and cytotoxicity [47]. The LD50 of BMs was 62.7 mg/kg when injected into the sublingual vein of SD rats. Further studies, with injection of 40 mg/kg BMs, showed no significant difference between BM-treated and nontreated control rats in terms of routine blood exam results, liver and kidney function tests, organ coefficients of major organs, or Stimulation Index of lymph cells with ConA and/or LPS antigens. The histological examination of major organs from these 40 mg/kg BM-treated rats showed no obvious pathological changes, except increased number of vacuoles in livers and thicker interlobular septa in lungs. BMs showed little cytotoxic effect on H22, HL60, or EMT-6 cells. Incubation with 9 $\mu\text{g/mL}$ BMs neither inhibited nor stimulated the growth of all three cells and had no effect on DNA content, cell size, or cell membrane integrity. Kim et al. reported that magnetosomes without surface modification were incorporated into endothelial progenitor cells in vitro, and cells containing BMs showed high viability [48].

3. Superiority of BMs as Targeted Nanoscale Drug Carriers

Bacterial magnetosomes also show superiority as targeting nanoscale drug carriers, which is hardly matched by artificial magnetic particles. Using magnetosomes of *M. gryphiswaldense* as an example, BMs show superiority as follows: (a) very narrow size distribution (25–55 nm) and uniform morphology, which is biogenetically controllable and reproducible; (b) an inorganic component of Fe_3O_4 with high purity [49]; (c) stable single-magnetic-domain particles, which show paramagnetism with extremely high coercivity values, exceptionally larger magnetic losses converted into heat in hyperthermia, and more obvious T2 signal attenuation in MRI than that of synthetic magnetite samples; (d) negatively charged surface and better dispersion due to polarized primary amino groups in the magnetosome bilayer lipid membrane; (e) easy functionalization with diverse bioactive molecules because of the abundance of primary amino groups in the surface of magnetosomes; (f) potentially slow drug release from magnetosomes in vivo due to the digestible magnetosome membrane; (g) a well-established large-scale production method of magnetosomes with high purity [50, 51]; (h) high biocompatibility.

4. Drug-Loading Strategies with BMs

BMs are able to be modified very easily with diverse bioactive molecules due to the abundance of primary amino groups on the surface of magnetosome membrane and chimeric proteins displayed specifically on the surfaces of genetically engineered isolated magnetosomes [52]. There are two major drug-loading strategies: directly loading drugs to BMs with dual function linkers, and indirectly loading drugs to BMs with linkers after modification of BMs and/or drugs.

4.1. Direct Drug-Loading onto BMs with Dual Functional Linkers. There are many chemotherapeutic drugs which contain one or more amino groups per drug molecule. Doxorubicin, epirubicin, daunorubicin, idarubicin, and pirarubicin contain one amino group per molecule, while mitomycin, bleomycin, and peplomycin contain multi-amino groups per molecule. BMs can be linked to these drugs by the homobifunctional crosslinking agents such as aliphatic binary aldehyde, diisocyanates, diisothiocyanates, di(succinimido) aliphatic esters, and their derivatives (Table 1) [53]. Drugs with carboxyls or phosphate groups also can be linked to the amino groups of BMs by using 1-Ethyl-3-[3-dimethylamino-propyl] carbodiimide (EDC).

4.2. Indirect Drug-Loading onto BMs After Modification of BMs and/or Drugs. Drugs without amino or carboxyl groups cannot be directly linked to BMs through the previously mentioned methods. There are three ways to load such drugs to BMs: attaching an amino or carboxyl group to the drugs by modification of the drugs, modifying the BMs without changing the drug molecules, and modifying both the drug molecules and BMs so that they can be linked with bifunctional reagents.

Drugs with sulphydryl or disulfide bond can be linked to BMs with modified SPDP (N-Succinimidyl 3-[2-pyridyldithio] propionate) and then reduced with DTT (Dithiothreitol). For example, antibodies can be linked to BMs by this method [54, 55]. It is simple to switch amino groups into sulphydryls in the BMs or drugs when Traut's reagent 2-iminothiolane reacts with primary amino groups [53]. This reaction provides more choices for drug loading onto BMs. Drugs with primary amino groups can also be loaded onto BMs with this indirect method. For other drugs without amino group, sulphydryl or disulfide bond, drug loading onto BMs can be achieved by introducing one of these residues in the drugs and then using the strategies mentioned above.

Another unique method to load drugs onto BMs is by linking BMs with macromolecules, which are loaded with numerous small drug molecules [56]. Such macromolecules include poly-Glu, poly-Lys, poly-Asp, polyethylene glycol, and dextran. Poly-L-glutamic acid (PLGA) is a polymer of amino acids which contains multicarboxyl groups and only one single amino group. The single amino group of PLGA can be masked with a thiol group first and form PLGA-3-[2-pyridyldithio] propionyl (PLGA-PDP). PLGA-PDP, with the help of EDC, can react with small drug molecules carrying

amino groups such as doxorubicin (DOX) and form PDP-PLGA-(DOX) $_n$. This compound then reacts with the BMs modified with SPDP and DTT, and the PLGA-(DOX) $_n$ can be loaded onto BMs. The process is summarized in Figure 2.

There are also drug loading methods without additional chemical reactions. For example, BMs have a negatively charged surface can be modified with cationic silane such as N(trimethoxysilylpropyl) isothiuronium chloride, 3-Aminopropyltriethoxysilane, and 3-[2-(2-aminoethyl)-ethylamino]-propyltrimethoxysilane. The modified BMs show a cationic surface and can absorb nucleic acid drug [57, 58]. Protein A can be expressed in the membrane of BMs with genetic engineering can conjugate antibody drugs directly [52, 59].

5. Drug-Loading Types with BMs

There are four major groups of drugs that are able to be loaded onto BMs: protein drugs, nuclei acid drugs, radioactive isotopes, and chemotherapeutic drugs.

5.1. Protein Drugs. Protein drugs come in all shapes and sizes: recombinant human proteins such as insulin, growth hormone, and erythropoietin; monoclonal antibodies such as Remicade, Rituxan, and Erbitux; viral or bacterial proteins used as vaccines to elicit a specific immune response [60]. These protein drugs on the market fail to deliver in one or more target areas because they are digested or disrupted very readily during the process of crossing biological barriers such as organs, cells, and intracellular compartments. Therapeutic anticancer antibodies suffer from poor curative effects against solid tumors. Solid tumors are usually bounded with a pyknotic basement membrane and show lymphatic backflow obstacles, which impede the transfer of antibodies into solid tumors. This drawback can be overcome if the antibodies are loaded onto BMs and maintained in the solid tumors with magnets.

Methods for loading proteins onto BMs were developed by the research group led by T. Matsunaga. In 1987, Matsunaga et al. successfully immobilized glucose oxidase and uricase on BMs. The activity of glucose oxidase immobilized on BMs was 40 times than that of immobilized artificial magnetites or Zn-ferrite particles. Both glucose oxidase and uricase coupled with BMs retained their activities when they were reused five times [61]. The same research group also immobilized FITC conjugated anti-IgG antibodies on BMs, which were modified with glutaraldehyde or SPDP for the detection of allergen [19, 54, 55]. In 2001, the group loaded Hemoglobin A1c (HbA1c) onto modified BMs, which were coupled with m-aminophenylboronic acid (mAPB) by using homobifunctional crosslinker, Bis(succinimidyl)suberate (BS3) (Figure 3) [62].

Recombinant BMs with Protein A expressed on their surface were constructed using magA. MagA is a key gene in the BMs biosynthesis of magnetotactic bacteria. Homogeneous chemiluminescence enzyme immunoassay using antibody bound Protein A-BMs complexes was developed for detection of human IgG (Figure 4) [52, 59].

TABLE 1: Homobifunctional cross linkers that can react with amino group [53].

Linker reagents	
Imidoesters	<p>Reaction</p> $R-NH_2 + R'-CH_2-C(=NH_2^+)OCH_3 \longrightarrow R'-CH_2-C(=NH)R + CH_3OH$ <p>Agents</p> <div style="display: flex; justify-content: space-around;"> <div> <p>DMA</p> $^{-}Cl^+H_2N-C(=O)CH_2-CH_2-CH_2-CH_2-C(=O)NH_2^+Cl^{-}$ $H_3CO \quad OCH_3$ </div> <div> <p>DTBP</p> $^{-}Cl^+H_2N-C(=O)CH_2-CH_2-S-S-CH_2-CH_2-C(=O)NH_2^+Cl^{-}$ $H_3CO \quad OCH_3$ </div> </div> <div style="display: flex; justify-content: space-around;"> <div> <p>DMS</p> $^{-}Cl^+H_2N-C(=O)CH_2-CH_2-CH_2-CH_2-CH_2-CH_2-C(=O)NH_2^+Cl^{-}$ $H_3CO \quad OCH_3$ </div> <div> <p>DMP</p> $^{-}Cl^+H_2N-C(=O)CH_2-CH_2-CH_2-CH_2-CH_2-C(=O)NH_2^+Cl^{-}$ $H_3CO \quad OCH_3$ </div> </div>
NHS esters	<p>Reaction</p> $R-NH_2 + R'-C(=O)O-N \begin{array}{c} \diagup \diagdown \\ \diagdown \diagup \end{array} \longrightarrow R'-C(=O)NHR + \begin{array}{c} \diagup \diagdown \\ \diagdown \diagup \end{array} N-OH$ <p>Agents</p> <div style="display: flex; justify-content: space-around;"> <div> <p>DSG</p> $\begin{array}{c} \diagup \diagdown \\ \diagdown \diagup \end{array} N-O-C(=O)-CH_2-CH_2-CH_2-C(=O)-O-N \begin{array}{c} \diagup \diagdown \\ \diagdown \diagup \end{array}$ </div> <div> <p>DST</p> $\begin{array}{c} \diagup \diagdown \\ \diagdown \diagup \end{array} N-O-C(=O)-C(OH)(H)-C(OH)(H)-C(=O)-O-N \begin{array}{c} \diagup \diagdown \\ \diagdown \diagup \end{array}$ </div> </div> <div style="display: flex; justify-content: space-around;"> <div> <p>Sulto-GMBS</p> $\begin{array}{c} \diagup \diagdown \\ \diagdown \diagup \end{array} N-(CH_2)_3-C(=O)-O-N \begin{array}{c} \diagup \diagdown \\ \diagdown \diagup \end{array} SO_3Na$ </div> <div> <p>Sulto-SMPB</p> $NaO_3S \begin{array}{c} \diagup \diagdown \\ \diagdown \diagup \end{array} N-O-C(=O)-CH_2-CH_2-CH_2-C_6H_4-N \begin{array}{c} \diagup \diagdown \\ \diagdown \diagup \end{array}$ </div> </div>
Aldehydes	<p>Reaction</p> $R-NH_2 + R'-CHO \rightleftharpoons R'-CH=N-R \xrightarrow{NaCNBH_3} R'-CH_2-NH-R$ <p>Agents</p> $O=CH-CH_2-CH_2-CH_2-CH_2-CHO$
Photoreactive crosslinkers	<p>Reaction</p> <p>Diazopyruvate derivative</p> $R-NH-C(=O)-C(=O)-CH=N^+=N^- \xrightarrow{UV \text{ light}} R-NH-C(=O)-C(=O)-C: \longrightarrow R-NH-C(=O)-CH=O \xrightarrow[H_2N-R']{\text{Nucleophile}} R-NH-C(=O)-CH_2-C(=O)-NH-R'$ <p>Carbene formation with wolff rearrangement to reactive ketene</p> <p>Insertion with covalent bond formation</p> <p>Ring expansion</p> $\begin{array}{c} \diagup \diagdown \\ \diagdown \diagup \end{array} N=N^+=N^- \xrightarrow{UV \text{ light}} \begin{array}{c} \diagup \diagdown \\ \diagdown \diagup \end{array} N: \xrightarrow{\text{Ring expansion}} \begin{array}{c} \diagup \diagdown \\ \diagdown \diagup \end{array} \xrightarrow{R-NH_2} \begin{array}{c} \diagup \diagdown \\ \diagdown \diagup \end{array} N-R$

TABLE 1: Continued.

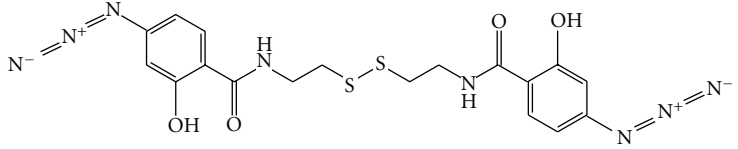
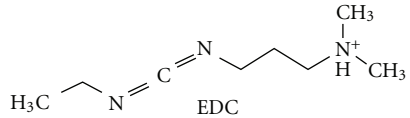
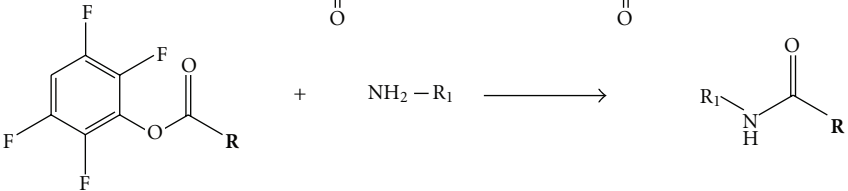
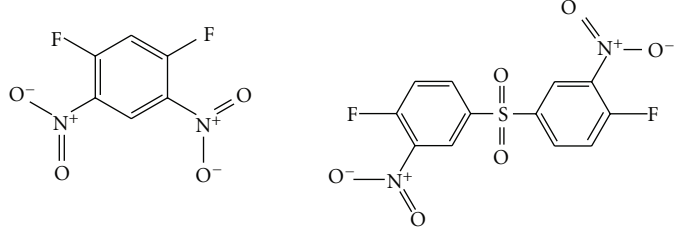
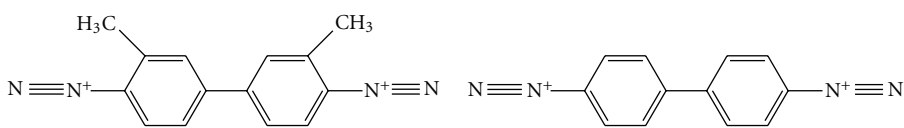
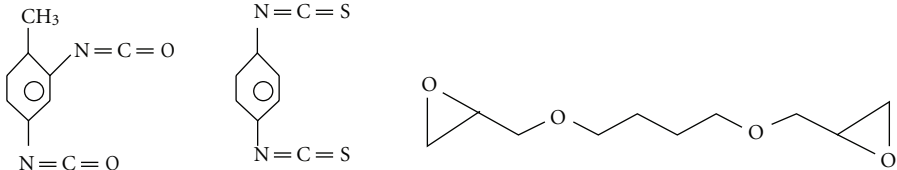
Photoreactive crosslinkers	 <p>Based</p>
Reaction	$\text{R}-\text{O}-\text{P}(\text{OH})(\text{O}^-)-\text{OH} + \text{R}'-\text{NH}_2 \xrightarrow{\text{EDC}} \text{R}-\text{O}-\text{P}(\text{OH})(\text{O}^-)-\text{NH}-\text{R}'$
Carbodiimides	$\text{R}-\text{COOH} + \text{R}'-\text{NH}_2 \xrightarrow{\text{EDC}} \text{R}-\text{CONH}-\text{R}'$
Agents	 <p>EDC</p>
Reaction	$\text{R}-\text{NH}_2 + \text{C}_6\text{H}_5\text{F} \longrightarrow \text{C}_6\text{H}_5\text{NHR}$ $\text{R}-\text{NH}_2 + \text{R}'-\text{SO}_2\text{Cl} \longrightarrow \text{R}'-\text{SO}_2\text{NHR}$
Halides	
Agents	 <p>DFDNB DFDNPS</p>
Reaction	$\text{R}-\text{NH}_2 + \text{R}'-\text{C}(=\text{O})-\text{N}^+\equiv\text{N} \longrightarrow \text{R}'-\text{C}(=\text{O})-\text{NHR}$
Agents	

TABLE 1: Continued.

Others	Reaction	$\text{R}-\text{NH}_2 + \text{R}'-\text{N}=\text{C}=\text{O} \longrightarrow \text{R}'-\text{HN}-\overset{\text{O}}{\underset{\text{ }}{\text{C}}}-\text{NH}-\text{R}$
		$\text{R}-\text{NH}_2 + \text{R}'-\text{N}=\text{C}=\text{S} \longrightarrow \text{R}'-\text{HN}-\overset{\text{S}}{\underset{\text{ }}{\text{C}}}-\text{NH}-\text{R}$
		$\text{R}-\text{Cyclopropane} + \text{R}'-\text{NH}_2 \longrightarrow \text{R}-\text{CH}_2-\text{CH}(\text{OH})-\text{CH}_2-\text{NH}-\text{R}'$
Agents		

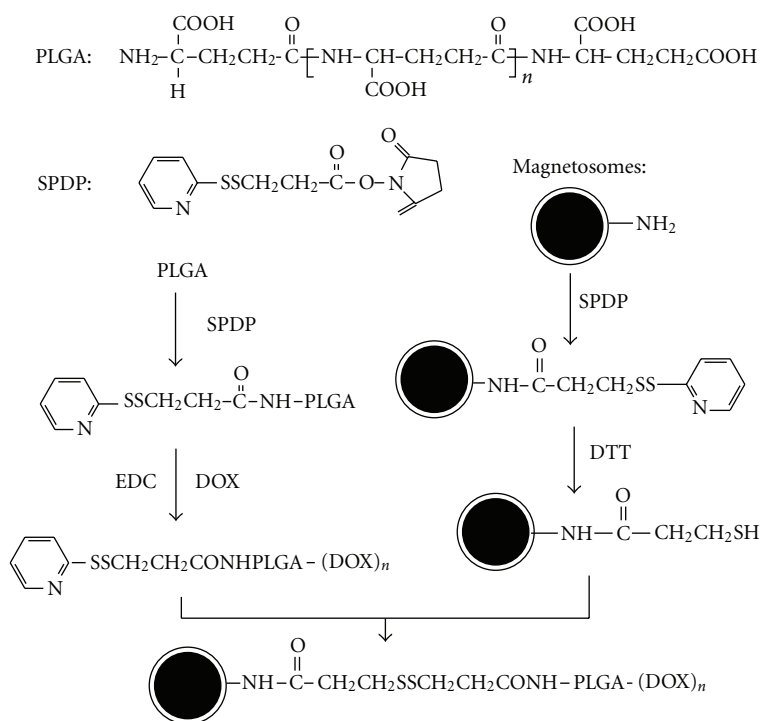


FIGURE 2: Schematic diagram of using PLGA as a bridge to link DOX with BMs.

Yoshino et al. established a method for displaying functional proteins on BMPs [63–65]. A novel promoter, termed msp3 promoter, was identified for the strong expression of BMs' membrane-specific protein using *M. magneticum* AMB-1 genome and proteome databases. The msp3 promoter showed 400 times higher activity than the magA promoter previously used. Efficient protein display on BMs was performed using the newly identified promoter sequences. This developed display system will facilitate the assembly of various functional proteins onto BMs.

5.2. Nucleic Acid Drugs. Nucleic acids, DNA, and RNA are endogenous materials which encode genetic information responsible for the biological process and also for dreadful

diseases as well. The nucleic acids act as drugs through different mechanisms such as binding with the synthesized proteins and hybridizing to a messenger RNA, that leads to translation altering or inducing degradation of target RNA. Through this process, the nucleic acids act as drugs for gene expression and regulation. BMs were reported for DNA and RNA extraction and gene delivery and detection [57, 58, 67–71].

BMs have a negatively charged surface and a membrane that contains 25% phosphatidylethanolamino and can absorb much lower nucleic acids (less than 0.5 μg DNA per 100 μg BMs) directly. Matsunaga's group modified BMs with cationic silanes such as N(trimethoxysilylpropyl) isothiuronium chloride, 3-Aminopropyltriethoxysi-

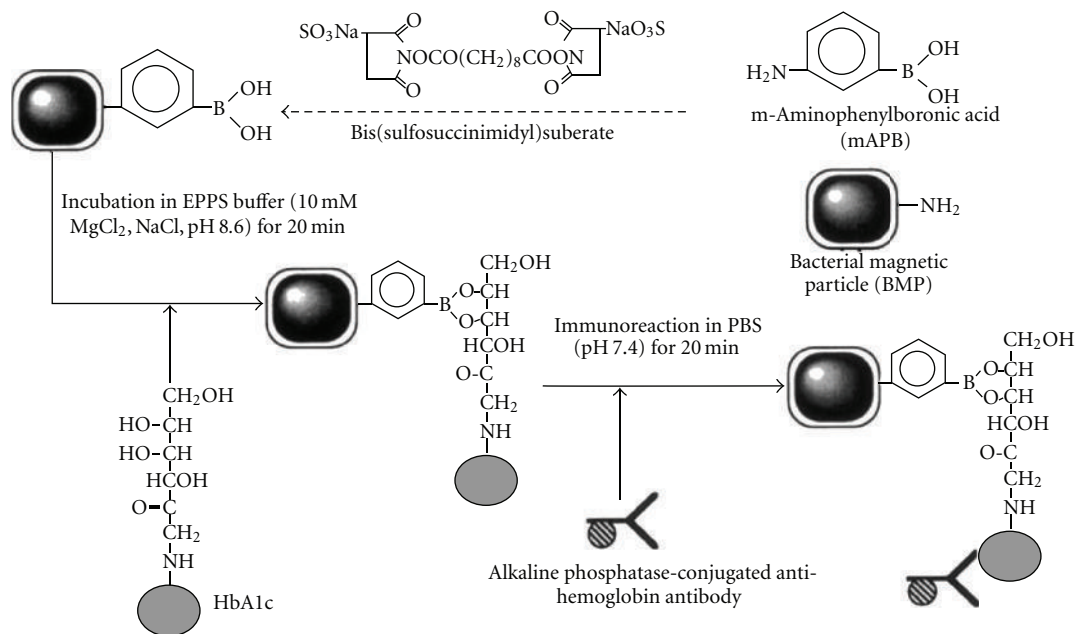


FIGURE 3: Schematic diagram of the boronate affinity immunoassay using mAPB-BMPs and alkaline phosphatase-conjugated anti-Ho antibody (ALP-antibody) [62].

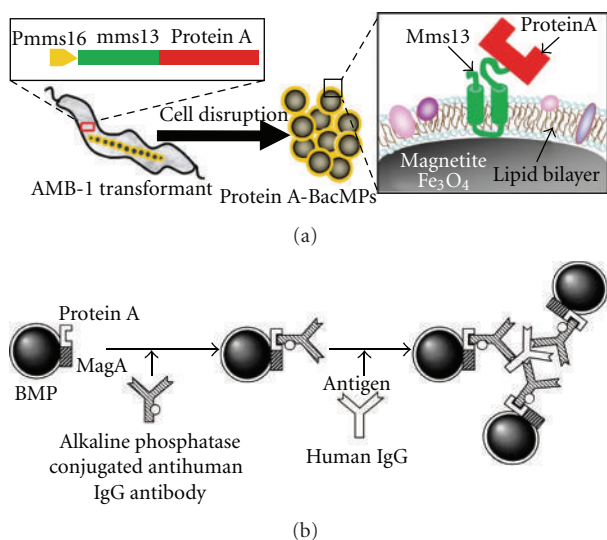


FIGURE 4: Schematic diagram of production of Protein A-BMs (A) and the homogenous chemiluminescence enzyme immunoassay using Protein A-BMs complexes [52, 65].

lane, and 3-[2-(2-aminoethyl)-ethylamino]-propyltrimethoxysilane. The DNA binding efficiency of the modified BMs increased with the number of amino groups presented on the silane compounds and was 14-fold higher than that of untreated BMs [57]. They also developed a better method of direct formation of a cascading hyperbranched polyamidoamino dendrimer onto the surface of amino silane modified BMs (Figure 5) [58]. Characterization of the synthesis revealed linear doubling of the surface

amino charge from generations one through five starting with an amino silane initiator. The dendrimer modified BMs have been used to carry out magnetic separation of DNA. Binding and release efficiencies increased with the number of generations of dendrimer. The binding and release efficiencies of bacterial magnetite modified with six-generation dendrimer (1.7×10^6 aminos/BM) were 7 and 11 times, compared with bacterial magnetites modified with only amino silane.

The Matsunaga group also immobilized biotin-labeled oligonucleotide probes onto BMs, which were modified with Sulfo-NHS-LC-LC-biotin and streptavidin [68–71]. A semiautomated system for the large-scale detection of single nucleotide polymorphisms (SNPs) has been developed with these probes-BMs particles [71]. Matsunaga et al. developed this method which binds nucleic acid fragments or protein to BMs modified with dual functional reagents after several reaction steps [71]. Biotin groups were attached to the magnetosome membrane either by incorporation of [1,2-dipalmitoyl-sn-glycero-3-phosphoethanolamino-N-(biotinyl)(sodiumsalt)] (biotin-DPPE) or by the covalent modification of the proteins within the magnetosome membrane using sulfo-N-hydroxy-succinimide ester sodium salt (NHS-biotin). Magnetosomes modified with surface-bound biotin groups were used to bind streptavidin (STV), and the resulting STV-functionalized BMs were functionalized with biotinylated DNA oligomers and/or antibodies.

5.3. Radioactive Isotopes. Radiotherapy can be used to treat diseases, especially cancer, using radiation to weaken or destroy particular targeted cells. Different types of radiation sources such as X-rays, γ -rays, particle beams, protons or neutrons are used to destroy the cancer cells within

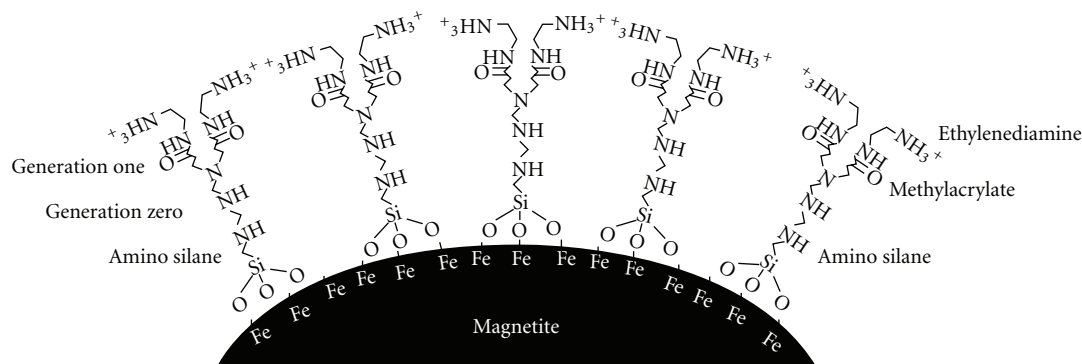


FIGURE 5: Structure of amino silane modified bacterial magnetite dendrimer [58].

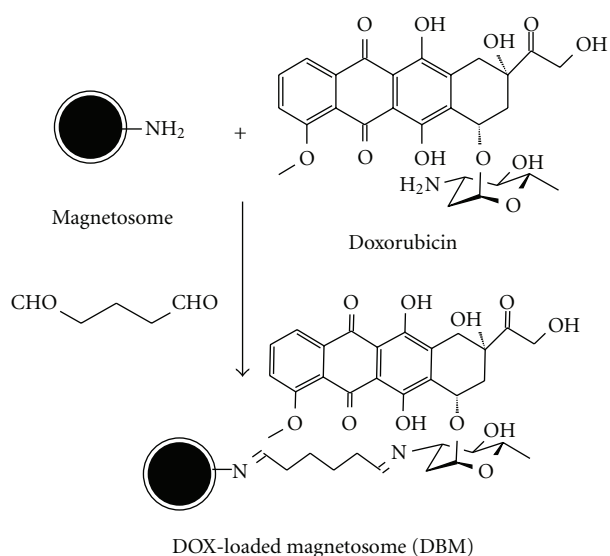


FIGURE 6: Schematic diagram for preparing DBMs with glutaraldehyde [66].

the body [72, 73]. The most commonly used radioactive isotope in clinic is technetium-99, and accounts for 80% of nuclear medicine procedures. In the US alone, over 18 million nuclear medicine procedures are recorded each year. Radioactive isotopes such as ^{99m}Tc , ^{131}I , ^{123}I , and ^{111}In can be linked to BMs with suitable chelates, radioactive-labeled molecules such as nucleic acids and proteins, and by including the radioactive isotopes in culture medium during BMs' formation. BMs labeled with radioactive isotopes show advantages in internal radiation or brachytherapy of solid tumors due to their targeted delivery.

5.4. Chemotherapeutic Drugs. The era of cancer chemotherapy began in the 1940s with the use of nitrogen mustards and folic acid antagonist drugs, and cancer drug development has been used widely since then [74, 75]. Modern chemotherapy avails itself, further to the cytotoxic drugs, of further agents that are differentiation inducers, radiosensitising agents, biological response modifiers, and/or agents capable of inducing hypoxia in the neoplastic clone

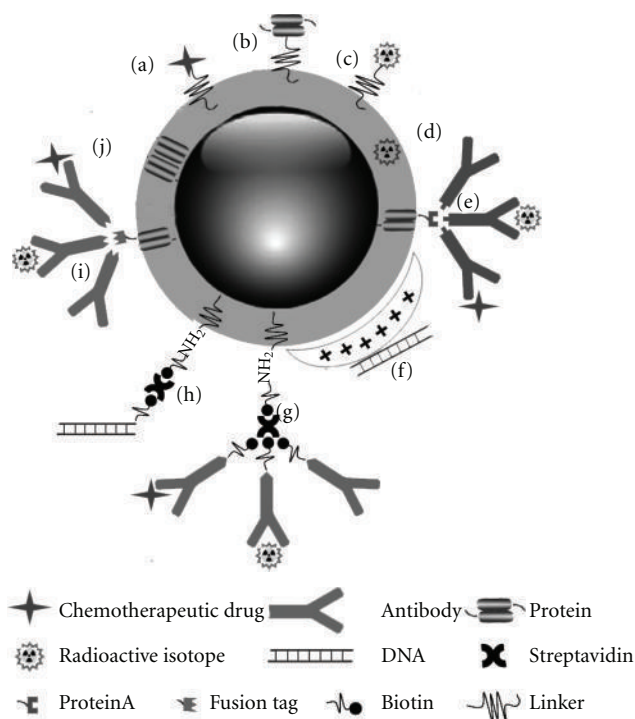


FIGURE 7: Schematic diagram of multifunctional BMs. Chemotherapeutic drug (a), protein drug (b), and radioactive isotope (c) could be loaded onto BMs by cross linkers or chelators. Radioactive isotopes could be incorporated in the membrane of BMs during the formation of BMs (d). Antibodies modified with or without radioactive isotopes or chemotherapeutic drugs could be loaded onto BMs by immunoconjugating the genetic engineering expressed Protein A (e) or fusion protein tag (i) or by streptavidin-mediated conjugation with the biotin-streptavidin-biotin (g). DNA drugs could be absorbed onto BMs modified with cationic silanes (f) or linked to BMs with biotin-streptavidin-biotin (h). Specific protein drug could be expressed in BMs membrane by genetic fusion to BMs membrane protein (j).

cells. The majority of chemotherapeutic drugs can be divided into alkylating agents, antimetabolites, anthracyclines, plant alkaloids, topoisomerase inhibitors, and other antitumour agents [76]. All of these drugs affect cell division or DNA

synthesis and function in some way. The activities of the most chemotherapeutic drugs suffer from the inability to accumulate selectively at the site of action. Drug targeting may attenuate adverse effects.

BM's membrane contains an abundance of primary amino groups which can be modified and/or linked with chemotherapeutic drugs by various strategies mentioned above. Sun et al. provided an effective method of loading doxorubicin (DOX) onto BMs with glutaraldehyde (Figure 6) and explored the clinical potential of magnetosomes as drug carriers in target therapy of cancers [13, 66]. Cancer suppressant effects in response to DOX-loaded BMs (DBMs) was evaluated. The DBMs prepared were cytotoxic to H22, HL60, and EMT-6 cells with inhibition of cell proliferation, suppression in c-myc expression, and diminishment of cell size and DNA content, which is consistent with free DOX. The in vivo antitumor effects were evaluated in BABL/c mice bearing tumors formed with H22 cells. In H22 cell-bearing mice, DBMs, DOX, and BMs displayed tumor suppression rates of 86.8%, 78.6%, and 4.3%, respectively. The mortality rates following administration of DBMs, DOX, and BMs were 20%, 80%, and 0%, respectively. Pathological examination of hearts and tumors revealed that both DBMs and DOX effectively inhibited tumor growth, but DBMs displayed a much lower cardiac toxicity compared with DOX.

6. Prospective

Magnetosomes are shown to be excellent magnetic nanocarriers for antibodies, enzymes, ligands, nucleic acids, and chemotherapeutic drugs. It was reported that functionalized magnetosomes could be used for DNA/RNA recovery, ELISA, cell sorting, target therapy of cancers, gene delivery, and as a contrast agent in MRI and cellular markers for gene expression. Although most of these studies are still at the proof-of-concept stage, and each study showed only one type of potential application of magnetosomes, these findings indicated that it will be very easy to develop multifunctional magnetosomes for clinical application. For instance, magnetosomes premodified with anticancer drugs can be linked with radioactive isotope-labeled antibodies and can recognize carcinoembryonic antigens. The multifunctional magnetosomes can simultaneously be used as molecular probes for tumor detection with MRI and as targeting drug carriers for tumor chemotherapy and radioimmunotherapy combined with magnetic hyperthermia (Figure 7). There are great potentials for the preclinical and clinical applications of the BMs.

Acknowledgments

This paper was supported in part by Chinese High Technology Research and Development Program (no. 2007AA021805), Chinese Natural Science Foundation project (no. 30970784), National Key Basic Research Program of China (2009CB930200), Chinese Academy of Sciences (CAS) "Hundred Talents Program" (07165111ZX), and CAS Knowledge Innovation Program. This paper was

also supported by DoD USAMRMC W81XWH-10-1-0767 and NIH/NCRR/RCMI G12 RR003048 grants.

References

- [1] P. Couvreur, B. Kante, and L. Grislain, "Toxicity of polyalkylcyanoacrylate nanoparticles. II: doxorubicin-loaded nanoparticles," *Journal of Pharmaceutical Sciences*, vol. 71, no. 7, pp. 790–792, 1982.
- [2] G. A. Hughes, "Nanostructure-mediated drug delivery," *Nanomedicine*, vol. 1, no. 1, pp. 22–30, 2005.
- [3] M. Yokoyama, "Drug targeting with nano-sized carrier systems," *Journal of Artificial Organs*, vol. 8, no. 2, pp. 77–84, 2005.
- [4] A. Singh, G. Garg, and P. K. Sharma, "Nanospheres: a novel approach for targeted drug delivery system," *International Journal of Pharmaceutical Sciences Review and Research*, vol. 5, no. 3, pp. 84–88, 2010.
- [5] V. P. Torchilin, "Drug targeting," *European Journal of Pharmaceutical Sciences*, vol. 11, no. 2, pp. S81–S91, 2000.
- [6] G. A. Silva, "Nanotechnology approaches for drug and small molecule delivery across the blood brain barrier," *Surgical Neurology*, vol. 67, no. 2, pp. 113–116, 2007.
- [7] Q. A. Pankhurst, J. Connolly, S. K. Jones, and J. Dobson, "Applications of magnetic nanoparticles in biomedicine," *Journal of Physics D*, vol. 36, no. 13, pp. R167–R181, 2003.
- [8] J. Dobson, "Magnetic nanoparticles for drug delivery," *Drug Development Research*, vol. 67, no. 1, pp. 55–60, 2006.
- [9] J. Akhtar, R. Chaturvedi, J. Sharma et al., "Magnetized carrier as novel drug delivery system," *International Journal of Drug Delivery Technology*, vol. 1, no. 1, pp. 28–35, 2009.
- [10] K. J. Widder, A. E. Senyei, and D. G. Scarpelli, "Magnetic microspheres: a model system for site specific drug delivery in vivo," *Proceedings of the Society for Experimental Biology and Medicine*, vol. 158, no. 2, pp. 141–146, 1978.
- [11] D. L. Balkwill, D. Maratea, and R. P. Blakemore, "Ultrastructure of a magnetotactic spirillum," *Journal of Bacteriology*, vol. 141, no. 3, pp. 1399–1408, 1980.
- [12] M. Hopkin, "Magnet-making bacteria could target tumours," *Naturenews*, 2004.
- [13] J. B. Sun, J. H. Duan, S. L. Dai et al., "In vitro and in vivo antitumor effects of doxorubicin loaded with bacterial magnetosomes (DBMs) on H22 cells: the magnetic bio-nanoparticles as drug carriers," *Cancer Letters*, vol. 258, no. 1, pp. 109–117, 2007.
- [14] V. K. Varadan, L. Chen, and J. Xie, "Magnetosomes and their biomedical applications," in *Nanomedicine*, pp. 175–213, John Wiley & Sons, Chichester, UK, 2008.
- [15] J. Xie, K. Chen, and X. Chen, "Production, modification and bio-applications of magnetic nanoparticles gestated by magnetotactic bacteria," *Nano Research*, vol. 2, no. 4, pp. 261–278, 2009.
- [16] D. A. Bazylnski, A. J. Garratt-Reed, and R. B. Frankel, "Electron microscopic studies of magnetosomes in magnetotactic bacteria," *Microscopy Research and Technique*, vol. 27, no. 5, pp. 389–401, 1994.
- [17] A. Hoell, A. Wiedenmann, U. Heyen, and D. Schüler, "Nanostructure and field-induced arrangement of magnetosomes studied by SANSPOLE," *Physica B*, vol. 350, no. 1–3, pp. E309–E313, 2004.
- [18] Y. A. Gorbey, T. J. Beveridge, and R. P. Blakemore, "Characterization of the bacterial magnetosome membrane," *Journal of Bacteriology*, vol. 170, no. 2, pp. 834–841, 1988.

- [19] N. Nakamura, K. Hashimoto, and T. Matsunaga, "Immunoassay method for the determination of immunoglobulin G using bacterial magnetic particles," *Analytical Chemistry*, vol. 63, no. 3, pp. 268–272, 1991.
- [20] K. Grünberg, E. C. Müller, A. Otto et al., "Biochemical and proteomic analysis of the magnetosome membrane in magnetospirillum gryphiswaldense," *Applied and Environmental Microbiology*, vol. 70, no. 2, pp. 1040–1050, 2004.
- [21] U. Lins, F. Freitas, C. N. Keim, and M. Farina, "Electron spectroscopic imaging of magnetotactic bacteria: magnetosome morphology and diversity," *Microscopy and Microanalysis*, vol. 6, no. 5, pp. 463–470, 2000.
- [22] D. Schüler and R. B. Frankel, "Bacterial magnetosomes: microbiology, biomineralization and biotechnological applications," *Applied Microbiology and Biotechnology*, vol. 52, no. 4, pp. 464–473, 1999.
- [23] D. Schüler, "The biomineralization of magnetosomes in Magnetospirillum gryphiswaldense," *International Microbiology*, vol. 5, no. 4, pp. 209–214, 2002.
- [24] J. B. Sun, Z. L. Wang, J. H. Duan et al., "Targeted distribution of bacterial magnetosomes isolated from magnetospirillum gryphiswaldense MSR-1 in healthy sprague-dawley rats," *Journal of Nanoscience and Nanotechnology*, vol. 9, no. 3, pp. 1881–1885, 2009.
- [25] M. Pósfai, P. R. Buseck, D. A. Bazylinski, and R. B. Frankel, "Reaction sequence of iron sulfide minerals in bacteria and their use as biomarkers," *Science*, vol. 280, no. 5365, pp. 880–883, 1998.
- [26] M. Tanaka, Y. Okamura, A. Arakaki, T. Tanaka, H. Takeyama, and T. Matsunaga, "Origin of magnetosome membrane: proteomic analysis of magnetosome membrane and comparison with cytoplasmic membrane," *Proteomics*, vol. 6, no. 19, pp. 5234–5247, 2006.
- [27] T. Matsunaga, M. Nemoto, A. Arakaki, and M. Tanaka, "Proteomic analysis of irregular, bullet-shaped magnetosomes in the sulphate-reducing magnetotactic bacterium Desulfovibrio magneticus RS-1," *Proteomics*, vol. 9, no. 12, pp. 3341–3352, 2009.
- [28] T. Tanaka and T. Matsunaga, "Fully automated chemiluminescence immunoassay of insulin using antibody—Protein A—bacterial magnetic particle complexes," *Analytical Chemistry*, vol. 72, no. 15, pp. 3518–3522, 2000.
- [29] A. Vonarbourg, C. Passirani, P. Saulnier, and J. P. Benoit, "Parameters influencing the stealthiness of colloidal drug delivery systems," *Biomaterials*, vol. 27, no. 24, pp. 4356–4373, 2006.
- [30] L. Juillerat-Jeanneret and F. Schmitt, "Chemical modification of therapeutic drugs or drug vector systems to achieve targeted therapy: looking for the grail," *Medicinal Research Reviews*, vol. 27, no. 4, pp. 574–590, 2007.
- [31] B. M. Moskowitz, R. B. Frankel, P. J. Flanders, R. P. Blakemore, and B. B. Schwartz, "Magnetic properties of magnetotactic bacteria," *Journal of Magnetism and Magnetic Materials*, vol. 73, no. 3, pp. 273–288, 1988.
- [32] R. E. Dunin-Borkowski, M. R. McCartney, R. B. Frankel, D. A. Bazylinski, M. Pósfai, and P. R. Buseck, "Magnetic microstructure of magnetotactic bacteria by electron holography," *Science*, vol. 282, no. 5395, pp. 1868–1870, 1998.
- [33] M. Timko, A. Džarová, P. Kopčanský et al., "Magnetic properties of magnetite formed by biomineralization and chemical synthesis," *Acta Physica Polonica A*, vol. 113, no. 1, pp. 573–576, 2008.
- [34] R. Hergt, R. Hiergeist, M. Zeisberger et al., "Magnetic properties of bacterial magnetosomes as potential diagnostic and therapeutic tools," *Journal of Magnetism and Magnetic Materials*, vol. 293, no. 1, pp. 80–86, 2005.
- [35] O. Felfoul, M. Mohammadi, and S. Martel, "Magnetic resonance imaging of Fe₃O₄ nanoparticles embedded in living magnetotactic bacteria for potential use as carriers for in vivo applications," in *Proceedings of the 29th Annual International Conference of IEEE-EMBS, Engineering in Medicine and Biology Society (EMBC '07)*, pp. 1463–1466, August 2007.
- [36] F. C. Meldrum, S. Mann, B. R. Heywood, R. B. Frankel, and D. A. Bazylinski, "Electron microscopy study of magnetosomes in two cultured vibrioid magnetotactic bacteria," *Proceedings of the Royal Society B*, vol. 251, no. 1332, pp. 237–242, 1993.
- [37] A. R. Muxworthy and W. Williams, "Critical superparamagnetic/single-domain grain sizes in interacting magnetite particles: implications for magnetosome crystals," *Journal of the Royal Society Interface*, vol. 6, no. 41, pp. 1207–1212, 2009.
- [38] I. Penninga, H. de Waard, B. M. Moskowitz, D. A. Bazylinski, and R. B. Frankel, "Remanence measurements on individual magnetotactic bacteria using a pulsed magnetic field," *Journal of Magnetism and Magnetic Materials*, vol. 149, no. 3, pp. 279–286, 1995.
- [39] C. U. Herborn, N. Papanikolaou, R. Reszka, K. Grünberg, D. Schüler, and J. F. Debatin, "Magnetosomes as biological model for iron binding: relaxivity determination with MRI," *Fortschr Röntgenstr.*, vol. 175, no. 6, pp. 830–834, 2003.
- [40] D. Eberbeck, V. Janke, S. Hartwig et al., "Blocking of magnetic moments of magnetosomes measured by magnetorelaxometry and direct observation by magnetic force microscopy," *Journal of Magnetism and Magnetic Materials*, vol. 289, pp. 70–73, 2005.
- [41] R. Hergt, S. Dutz, R. Müller, and M. Zeisberger, "Magnetic particle hyperthermia: nanoparticle magnetism and materials development for cancer therapy," *Journal of Physics Condensed Matter*, vol. 18, no. 38, article S26, pp. S2919–S2934, 2006.
- [42] E. Alphandéry, S. Faure, L. Raison, E. Duguet, P. A. Howse, and D. A. Bazylinski, "Heat production by bacterial magnetosomes exposed to an oscillating magnetic field," *The Journal of Physical Chemistry C*, vol. 115, no. 1, pp. 18–22, 2011.
- [43] L. L. Hu, F. Zhang, Z. Wang et al., "Comparison of the ¹H NMR relaxation enhancement produced by bacterial magnetosomes and synthetic iron oxide nanoparticles for potential use as MR molecular probes," *IEEE Transactions on Applied Superconductivity*, vol. 20, no. 3, pp. 822–825, 2010.
- [44] U. O. Häfeli and G. J. Pauer, "In vitro and in vivo toxicity of magnetic microspheres," *Journal of Magnetism and Magnetic Materials*, vol. 194, no. 1, pp. 76–82, 1999.
- [45] V. Wagner, A. Dullaart, A. K. Bock, and A. Zweck, "The emerging nanomedicine landscape," *Nature Biotechnology*, vol. 24, no. 10, pp. 1211–1217, 2006.
- [46] L. Xiang, J. Wei, S. Jianbo, W. Guili, G. Feng, and L. Ying, "Purified and sterilized magnetosomes from Magnetospirillum gryphiswaldense MSR-1 were not toxic to mouse fibroblasts in vitro," *Letters in Applied Microbiology*, vol. 45, no. 1, pp. 75–81, 2007.
- [47] J. Sun, T. Tang, J. Duan et al., "Biocompatibility of bacterial magnetosomes: acute toxicity, immunotoxicity and cytotoxicity," *Nanotoxicology*, vol. 4, no. 3, pp. 271–283, 2010.
- [48] J. A. Kim, H. J. Lee, H. J. Kang, and T. H. Park, "The targeting of endothelial progenitor cells to a specific location within a microfluidic channel using magnetic nanoparticles," *Biomedical Microdevices*, vol. 11, no. 1, pp. 287–296, 2009.
- [49] A. Fischer, M. Schmitz, B. Aichmayer, P. Fratzl, and D. Favre, "Structural purity of magnetite nanoparticles in magnetotactic

- bacteria," *Journal of the Royal Society Interface*, vol. 8, no. 60, pp. 1011–1018, 2011.
- [50] J. B. Sun, F. Zhao, T. Tang et al., "High-yield growth and magnetosome formation by *Magnetospirillum gryphiswaldense* MSR-1 in an oxygen-controlled fermentor supplied solely with air," *Applied Microbiology and Biotechnology*, vol. 79, no. 3, pp. 389–397, 2008.
- [51] Y. Liu, G. R. Li, F. F. Guo, W. Jiang, Y. Li, and L. J. Li, "Large-scale production of magnetosomes by chemostat culture of *Magnetospirillum gryphiswaldense* at high cell density," *Microbial Cell Factories*, vol. 9, article 99, 2010.
- [52] T. Matsunaga, R. Sato, S. Kamiya, T. Tanaka, and H. Takeyama, "Chemiluminescence enzyme immunoassay using ProteinA-bacterial magnetite complex," *Journal of Magnetism and Magnetic Materials*, vol. 194, no. 1, pp. 126–131, 1999.
- [53] G. Hermanson, *Bioconjugate Techniques*, Academic Press, New York, NY, USA, 2nd edition, 2008.
- [54] N. Nakamura, J. G. Burgess, K. Yagiuda, S. Kudo, T. Sakaguchi, and T. Matsunaga, "Detection and removal of *Escherichia coli* using fluorescein isothiocyanate conjugated monoclonal antibody immobilized on bacterial magnetic particles," *Analytical Chemistry*, vol. 65, no. 15, pp. 2036–2039, 1993.
- [55] N. Nakamura and T. Matsunaga, "Highly sensitive detection of allergen using bacterial magnetic particles," *Analytica Chimica Acta*, vol. 281, no. 3, pp. 585–589, 1993.
- [56] Y. Kato, N. Umemoto, Y. Kayama et al., "A novel method of conjugation of daunomycin with antibody with a poly-L-glutamic acid derivative as intermediate drug carrier. An anti- α -fetoprotein antibody-daunomycin conjugate," *Journal of Medicinal Chemistry*, vol. 27, no. 12, pp. 1602–1607, 1984.
- [57] B. Yoza, M. Matsumoto, and T. Matsunaga, "DNA extraction using modified bacterial magnetic particles in the presence of amino silane compound," *Journal of Biotechnology*, vol. 94, no. 3, pp. 217–224, 2002.
- [58] B. Yoza, A. Arakaki, and T. Matsunaga, "DNA extraction using bacterial magnetic particles modified with hyperbranched polyamidoamine dendrimer," *Journal of Biotechnology*, vol. 101, no. 3, pp. 219–228, 2003.
- [59] T. Matsunaga, A. Arakaki, and M. Takahoko, "Preparation of luciferase-bacterial magnetic particle complex by artificial integration of MagA-luciferase fusion protein into the bacterial magnetic particle membrane," *Biotechnology and Bioengineering*, vol. 77, no. 6, pp. 614–618, 2002.
- [60] I. M. Tomlinson, "Next-generation protein drugs," *Nature Biotechnology*, vol. 22, no. 5, pp. 521–522, 2004.
- [61] T. Matsunaga and S. Kamiya, "Use of magnetic particles isolated from magnetotactic bacteria for enzyme immobilization," *Applied Microbiology and Biotechnology*, vol. 26, no. 4, pp. 328–332, 1987.
- [62] T. Tanaka and T. Matsunaga, "Detection of HbA1c by boronate affinity immunoassay using bacterial magnetic particles," *Biosensors and Bioelectronics*, vol. 16, no. 9–12, pp. 1089–1094, 2001.
- [63] T. Yoshino and T. Matsunaga, "Development of efficient expression system for protein display on bacterial magnetic particles," *Biochemical and Biophysical Research Communications*, vol. 338, no. 4, pp. 1678–1681, 2005.
- [64] T. Yoshino, F. Kato, H. Takeyama, M. Nakai, Y. Yakabe, and T. Matsunaga, "Development of a novel method for screening of estrogenic compounds using nano-sized bacterial magnetic particles displaying estrogen receptor," *Analytica Chimica Acta*, vol. 532, no. 2, pp. 105–111, 2005.
- [65] T. Yoshino, H. Hirabe, M. Takahashi, M. Kuhara, H. Takeyama, and T. Matsunaga, "Magnetic cell separation using nano-sized bacterial magnetic particles with reconstructed magnetosome membrane," *Biotechnology and Bioengineering*, vol. 101, no. 3, pp. 470–477, 2008.
- [66] J. B. Sun, J. H. Duan, S. L. Dai et al., "Preparation and anti-tumor efficiency evaluation of doxorubicin-loaded bacterial magnetosomes: magnetic nanoparticles as drug carriers isolated from *Magnetospirillum gryphiswaldense*," *Biotechnology and Bioengineering*, vol. 101, no. 6, pp. 1313–1320, 2008.
- [67] H. Takeyama, A. Yamazawa, C. Nakamura, and T. Matsunaga, "Application of bacterial magnetic particles as novel DNA carriers for ballistic transformation of a marine cyanobacterium," *Biotechnology Techniques*, vol. 9, no. 5, pp. 355–360, 1995.
- [68] H. Ota, H. Takeyama, H. Nakayama, T. Katoh, and T. Matsunaga, "SNP detection in transforming growth factor- β 1 gene using bacterial magnetic particles," *Biosensors and Bioelectronics*, vol. 18, no. 5–6, pp. 683–687, 2003.
- [69] K. Maruyama, H. Takeyama, E. Nemoto, T. Tanaka, K. Yoda, and T. Matsunaga, "Single nucleotide polymorphism detection in aldehyde dehydrogenase 2 (ALDH2) gene using bacterial magnetic particles based on dissociation curve analysis," *Biotechnology and Bioengineering*, vol. 87, no. 6, pp. 687–694, 2004.
- [70] B. Ceyhan, P. Alhorn, C. Lang, D. Schüler, and C. M. Niemeyer, "Semisynthetic biogenic magnetosome nanoparticles for the detection of proteins and nucleic acids," *Small*, vol. 2, no. 11, pp. 1251–1255, 2006.
- [71] T. Matsunaga, K. Maruyama, H. Takeyama, and T. Katoh, "High-throughput SNP detection using nano-scale engineered biomagnetite," *Biosensors and Bioelectronics*, vol. 22, no. 9–10, pp. 2315–2321, 2007.
- [72] C. A. Boswell and M. W. Brechbiel, "Development of radioimmunotherapeutic and diagnostic antibodies: an inside-out view," *Nuclear Medicine and Biology*, vol. 34, no. 7, pp. 757–778, 2007.
- [73] A. V. S. Anil Kumar, P. G. Kumar, and S. Shankar, "Role of nuclear medicine in evaluation and management of joint diseases," *Indian Journal of Rheumatology*, vol. 4, no. 2, pp. 61–68, 2009.
- [74] J. Hirsch, "An anniversary for cancer chemotherapy," *Journal of the American Medical Association*, vol. 296, no. 12, pp. 1518–1520, 2006.
- [75] M. J. Camp, J. W. Gilmore, M. M. Gullatte et al., "Antineoplastic agents," in *Clinical Guide to Antineoplastic Therapy: A Chemotherapy Handbook*, M. M. Gullatte, Ed., pp. 81–356, Oncology Nursing Society, Pittsburgh, Pa, USA, 2nd edition, 2007.
- [76] B. R. Mineev, *Cancer Management in Man: Chemotherapy, Biological Therapy, Hyperthermia and Supporting Measures*, vol. 13, Springer, Dordrecht, The Netherlands, 1st edition, 2011.

Korotcov AV¹, PhD; Wang T^{1,2,*}, PhD; Chen Y¹, BS; Sridhar R³, PhD; Mitchell J², PhD; Wang PC^{1,*}, PhD

¹ Molecular Imaging Laboratory, Department of Radiology, Howard University, Washington, DC

² Nanomaterials Characterization Science Center, Howard University, Washington, DC

³ Department of Radiation Oncology, Howard University, Washington, DC

PURPOSE: Fluorescent nanocrystalline semiconductor quantum dots (QDs) are suitable for biomedical imaging. Commonly used trioctylphosphine oxide (TOPO) based QDs may be unstable under physiological conditions because of ligand exchange between QDs and reactive nucleophilic biomolecules. This exchange may alter the biochemical structure of proteins, and may degrade QDs to release TOPO and toxic cadmium ions. Degradation of QDs by the action of mercaptoethanol was monitored using ³¹P NMR spectroscopy. The broad ³¹P NMR peak of intact QDs becomes progressively sharper as TOPO gradually detaches from the QDs.

METHODS: The QDs were prepared using a core obtained by the reaction between cadmium oxide and selenium followed by ZnS coating produced by the action of dimethyl zinc with hexamethyldisilathiane and finally coated with TOPO. Mercaptoethanol was selected to mimic biologically abundant nucleophilic mercaptoproteins, which may degrade QDs.

RESULTS: The ³¹P NMR signal related to TOPO cleavage increased with increasing concentration of mercaptoethanol, indicating gradual TOPO release and detachment from the surface of QDs. This was further confirmed by the dependence of chemical shift on mercaptoethanol concentration.

CONCLUSIONS: This study demonstrates that TOPO coated QDs are unstable in the presence of mercaptoethanol and suggests that biologically occurring mercapto compounds may also destabilize QDs. TOPO coated QDs may be unsafe for *in vivo* applications in humans and animals because of the potential for release of toxic cadmium ions under physiological conditions. Research supported by Howard University Seed grant U400007, 2G12 RR003048 from the RCMI Program NIH/NCRR, and DOD BC094936.

TUMOR OPTICAL IMAGING OF GLUCOSAMINE LINKED FLUORESCENT PROBES IN MICE

03.01.26

Korotcov AV¹, PhD; Ye Y^{1,2}, PhD; Chen Y¹, BS; Zhang F¹, PhD; Huang S¹, BS; Sridhar R³, PhD; Achilefu S², PhD; Wang PC^{1,*}, PhD

¹ Molecular Imaging Laboratory, Department of Radiology, Howard University, Washington, DC

² Optical Radiology Laboratory, Department of Radiology, Washington University, St. Louis MO

³ Department of Radiation Oncology, Howard University, Washington, DC

PURPOSE: The near-infrared fluorescence (NIRF) is an attractive noninvasive imaging modality for studying diseases at the molecular level. Glucose derivative transporters are often used as targets for *in vivo* NIRF. The linkage of more than one glucosamine (GlcN) to an imaging fluorophore may improve molecular probe's specificity. The suitability of two newly developed GlcN linked NIRF probes for optical imaging was evaluated and compared *in vitro* and *in vivo*.

METHODS: Cellular uptakes of the probes were investigated in PC-3-luc cells. *In vivo* NIRF imaging was performed on PC-3-luc tumor xenografts in nude mice. Cellular uptake, biodistribution (24 hours post injection) and tumor targeting specificity of cypate (cyp), cypate conjugated to a single GlcN (cyp-GlcN), and to two GlcNs (cyp-2GlcN) were studied.

RESULTS: The uptake of cyp-2GlcN (1 μ M) *in vitro* was higher than the uptake of cyp-GlcN and cyp. *In vivo* cyp-2GlcN demonstrated the highest maximum fluorescence intensity and lasted longer in the tumors (10nmol probe/mouse). The uptake of cyp-2GlcN/cyp-GlcN was inhibited by N-Acetyl-D-Glucosamine and enhanced by D-Glucosamine. The *ex-vivo* analysis revealed that tumor uptakes of cyp-2GlcN and cyp-GlcN were 4 and 2-fold higher than that of cyp.

CONCLUSIONS: Both cyp-GlcN and cyp-2GlcN NIRF probes have good tumor-targeting properties but tumor specific uptake of cyp-2GlcN was higher. The uptake mechanism is being explored further for developing cypate-glucosamine based probes for *in vivo* biomedical imaging in human subjects.

Research supported by Howard University Seed grant U400007, 2G12 RR003048 from the RCMI Program NIH/NCRR, and DOD BC094936.

INTEGRIN TARGETING AND TUMOR IMAGING: COMPARISON OF TWO RGD PEPTIDES 12.07.06

Y Ye, PhD; L Zhu, MS; B Xu, BS; P Wang, PhD; S Achilefu, PhD; X Chen, PhD

Laboratory of Molecular Imaging & Nanomedicine, NIBIB/NIH, Bethesda, MD (YY, LZ, XC); Optical Radiology Laboratory, Department of Radiology, Washington University, St. Louis (YY, BX, SA); Molecular Imaging Laboratory, Department of Radiology, Howard University, Washington, DC (YY, PW)

PURPOSE: Integrins are attractive targets for tumor imaging, diagnosis, and therapy due to their important roles in tumor pathogenesis, metastasis, and angiogenesis. Recently, an iRGD peptide has been reported for improving the imaging sensitivity and therapeutic efficacy due to its integrin targeting and deep tissue penetration. In this study, we compared iRGD with a conventional cyclic RGD i.e. c(RGDfK) by *in vitro* and *in vivo* studies.

DESIGN METHODS: The two peptide analogs were synthesized and labeled with near-infrared fluorescent dyes such as a synthetic dicarboxylic acid-containing carbocyanine (cypate) and a commercially available dye IRDye[®]800CW. They were evaluated by several methods including receptor binding, fluorescent microscopy, confocal microscopy, and noninvasive optical imaging in nude mice.

RESULTS: a series of such dye conjugates were obtained. The cypate-labeled iRGD (1) showed better cellular internalization than its counterpart labeled with the IRDye[®]800CW (2). Both 1 and 2 could not compete with the c(RGDfK) analogs in the integrin $\alpha v \beta 3$ binding affinity. The optical imaging showed the significant tumor localization of all the compounds in tumor xenograft-bearing nude mice. Nevertheless, 1 had longer liver retention while 2 had quicker kidney excretion.

CONCLUSIONS: The iRGD compounds have lower integrin $\alpha v \beta 3$ binding affinity than the corresponding c(RGDfK) analogs, but showed significant tumor localization *in vivo*. The conjugated dye motifs and related linkages have certain effects on their activities. Our results provide insights into discovery of novel integrin-targeted agents for tumor imaging and therapy.

Research supported by NIBIB/NIH intramural research, NIH/NCRR/RCM I 2G12 RR003048, DOD BC094936, and R01 CA109754.



31P NMR STUDY OF Thiol Mediated Degradation of Topo-Quantum Dots. Alexandru Korotcov, Howard University; Tongxin Wang, Dentistry/Nanocenter@Engineer; Yue Chen; Rajagopalan Sridhar, Department of Radiation Oncology, Howard University, Washington, DC; James Mitchell, College of Engineering; Paul Wang, Howard University, Cancer Center

Background: Semiconductor quantum dot nanocrystals (QDs) are useful as optical probes for biomedical imaging. However, the commonly used trioctylphosphine oxide (TOPO) coated QDs may be unstable under physiological conditions because of ligand exchange between QDs and reactive nucleophilic biomolecules. This exchange may alter the biochemical structure of proteins, and possibly degrade QDs to release TOPO and toxic cadmium ions. In this research, ^{31}P NMR spectroscopy was used to study the interaction between TOPO-QDs and biologically abundant mercapto (-SH) group. **Methods:** The QDs cores were prepared using the reaction between CdO and Se, and then coated with ZnS followed by TOPO. Mercaptoethanol was selected to mimic nucleophilicity of biologically abundant protein thiols. In order to monitor the ligand exchange reaction between QDs and thiol, mercaptoethanol (1 mM - 90 mM) was added to the suspension of QDs (56 mg/mL). **Results:** In the absence of thiol or low thiol concentration (less than 10 mM), no significant ^{31}P NMR signal related to TOPO was observed from QDs. Upon increasing the concentration of added thiol to 15 mM, a sharp peak around 45.5 ppm was observed, indicating that a small amount of a phosphorus containing species was cleaved from QDs by the action of thiol. The chemical shift of the cleaved phosphorus containing species was close to that of free TOPO, and the peak around 45.5 ppm was assigned to the cleaved TOPO from the surface of QDs. **Conclusions:** This study demonstrates that TOPO-QDs are relatively unstable and the TOPO can be cleaved from QDs in the presence of a nucleophilic agent such as thiol, which is widely distributed in tissues and physiological fluids. This research provides preliminary information about the potential risk presented by the degradation of TOPO-QDs in physiological systems. This research was supported by grants: DOD BC094936 and BC094963, HU Seed grant U400007, and NIH/NCRR/RCMI 2G12 RR003048.

Poster P32-6

BC094963-3159

MONITORING THIOL-MEDIATED DEGRADATION OF TOPO-QUANTUM DOTS BY ³¹P NUCLEAR MAGNETIC RESONANCE SPECTROSCOPY**Paul Wang, Tongxin Wang, Alexandru V. Korotcov, Yue Chen, Rajagopalan Sridhar, and James W. Mitchell**

Howard University, Washington

Background: Semiconductor quantum dot nanocrystals (QDs) are useful as optical probes for biomedical imaging. However, the potential release of toxic Cd²⁺ ions from QDs may preclude safe clinical use of QDs. Recent studies suggest that commonly used trioctylphosphine oxide (TOPO)-coated QDs may be unstable under physiological conditions because of ligand exchange between QDs and reactive nucleophilic biomolecules. This exchange may alter the biochemical structure of proteins and possibly degrade QDs to release TOPO and toxic cadmium ions. In this research, ³¹P nuclear magnetic resonance (NMR) spectroscopy was used to study the interaction between TOPO QDs and the biologically abundant mercapto (-SH) group.

Methods: The QDs were prepared using a core obtained by the reaction between cadmium oxide and selenium, coated by ZnS, produced by the reaction of dimethyl zinc with hexamethyldisilathiane, and then coated with TOPO. Transmission electron microscopy indicated the diameter of QDs was 6.2 nm. The optical properties of QDs were confirmed by fluorescent emission and ultraviolet and visible absorption spectra. To monitor the ligand exchange reaction between QDs and thiol, mercaptoethanol (from 1 mM to 90 mM) was added to the suspension of QDs (56 mg/mL). The ³¹P NMR spectra were obtained with a 400 MHz Bruker spectrometer. Chloroform (CDCl₃) was used as a solvent and phosphoric acid (H₃PO₄) as the external standard. Mercaptoethanol was selected to mimic biologically abundant nucleophilic mercaptoproteins, which may degrade QDs.

Results: In the absence of thiol, no significant ³¹P NMR signal related to TOPO was observed from QDs. Similar to the spectrum of QDs in the absence of thiol, the spectra did not display any significant peak related to phosphorus-containing species when the concentration of thiol was low (less than 10 mM). Upon increasing the concentration of added thiol to 15 mM, a sharp peak around 45.5 ppm was observed, indicating that a small amount of a phosphorus-containing species was cleaved from QDs by the action of thiol. As the thiol concentration was increased further, the related sharp peak became more prominent with increased intensity. The chemical shift of the cleaved phosphorus-containing species was close to that of free TOPO measured at the present condition (48.4 ppm), and the peak around 45.5 ppm was assigned to the cleaved TOPO from the surface of QDs.

Conclusions: This study demonstrates that TOPO QDs are relatively unstable and that TOPO can be cleaved from QDs upon the addition of a nucleophilic agent such as thiol. The signal strength of ³¹P NMR spectra indicates that the amount of TOPO cleaved from the surface of QDs is dependent on the amount of added thiol. Moreover, the cleavage of TOPO from QDs by thiol, as well as their interaction, was confirmed by the dependence of chemical shift of cleaved TOPO on the concentration of thiol. Thiols are widely distributed in tissues and physiological fluids. Surface exchange reaction or the binding of QDs with thiol groups on a variety of intracellular proteins may cause decreased functionality of biomolecules. This research provides preliminary information about the potential risk presented by the degradation of TOPO QDs in physiological systems.

This work was supported by the U.S. Army Medical Research and Materiel Command under W81XWH-10-1-0767, the National Institutes of Health (NIH/NCRR/RCMI 2G12 RR003048), and Howard University (U400007).

Applications of Nanoparticles for In Vivo ImagingPaul C. Wang^{1*}, Xing-Jie Liang²¹Molecular Imaging Laboratory, Howard University, Washington, DC 20060, USA²National Center for Nanoscience and Technology, China, Beijing 100080, China¹pwang@howard.edu, ²liangxj@nanocr.cn**Keywords:** nanoparticle, in vivo imaging, imaging modalities, nanomaterial, physicochemical property**Abstract:** Nanoparticles, which hold many unique properties, including versatility, tunable size, and highly adaptable surface chemistry, have been used successfully as imaging agents for in vivo imaging of various diseases. Using nanoparticles as imaging agents has significantly improved the detection sensitivity and specificity. Nanoparticles have great potential for early detection of cancer, genetic defects, cardiovascular and neurodegenerative diseases [1].

Using nanoparticles as an imaging agent provides new paradigms for every imaging modality: CT, MRI, PET, SPECT, Ultrasound, and Optical Imaging. Each imaging modality differs in detection sensitivity, depth penetration, spatial resolution, temporal resolution, costs, and whether it involves ionization radiation. Various materials, including liposome, dendrimer, micelle, polymer, gold nanoshell, colloidal gold, and fullerene, have been used to compose nanoparticles as imaging agents suitable for different imaging modalities. The physicochemical properties such as size, charge, shape, flexibility, hydrophilicity, and surface modification greatly influence the pharmacokinetics of nanoparticles, affecting their success as imaging agents [2]. The nano-sized imaging agents need to stay within the system for a sufficient time in order to produce the desired image enhancement effects. Reducing exposure to foreign material by optimizing clearance is a central principle for minimizing unwanted effects of any foreign materials within the human body. Nanoparticles are cleared from the vascular compartment through three primary mechanisms: renal clearance with excretion into the urine, hepatic clearance with biliary excretion, or uptake by macrophages into the reticuloendothelial system. For clinical application, renal clearance will be a preferred route for nanoparticles as imaging agents.

Although many studies have accomplished making nanoparticles to be more effective imaging agents, there are still challenges ahead for nano imaging agents to be translational into routine clinical practice, including further improvement of targeting efficiency and specificity, and how to overcome the associated toxicity to the patients [3].

References:

- [1] T.F. Massoud and S.S. Gambhir: Gene & Develop Vol.17 (2003), p.545-580
- [2] M.R. Longmire, M.Ogawa, P.L. Choyke and H. Kobayashi: Bioconjugate Chem (2011) DOI:10.1021/bc200111p
- [3] W.R. Sanhai, J.H. Sakamoto, R. Canady and M. Farrari: Nat Nanotechnology Vol.3 (2008), p.242-244

Topics: (6)

6. Nanobiotechnology and nanomedicine

Presentation Number **P159**

Poster Session 2

September 8, 2011 / 15:15-16:45 / Room: Hall F

Study of TOPO-Quantum Dot Degradation by ^{31}P NMR

Alexandru V. Korotcov¹, Tongxin Wang^{2,3}, Yue Chen¹, Rajagopalan Sridhar⁴, James Mitchell², Paul C. Wang¹, ¹Molecular Imaging Laboratory, Department of Radiology, Howard University, Washington, DC, USA; ²CREST Center for Nanomaterials, Howard University, Washington, DC, USA; ³College of Dentistry, Howard University, Washington, DC, USA; ⁴Department of Radiation Oncology, Howard University, Washington, DC, USA. Contact e-mail: akorotcov@howard.edu

BACKGROUND/HYPOTHESIS: Semiconductor quantum dot nanocrystals (QDs) are useful as optical probes for biomedical imaging. However, the commonly used trioctylphosphine oxide (TOPO) coated QDs may be unstable under physiological conditions because of ligand exchange between QDs and reactive nucleophilic biomolecules. This exchange may alter the biochemical structure of proteins, and possibly degrade QDs, causing them to release TOPO and toxic cadmium ions. In this study, ^{31}P NMR spectroscopy was used to monitor the interaction between TOPO-QDs and biologically abundant mercapto (-SH) group. **METHODS:** The cores of the QDs were prepared using the reaction between cadmium oxide and selenium and were then coated with ZnS followed by TOPO. Transmission electron microscopy showed that the QDs had a diameter of ~ 6.2 nm. The optical properties of QDs were confirmed by fluorescent emission and UV-Vis absorption spectra. UV-Vis spectrum showed broad absorption centered around 500 nm. Fluorescent spectrum showed an emission peak at 617 nm. Mercaptoethanol was selected to mimic nucleophilicity of biologically abundant protein thiols (Figure 1A). In order to monitor the ligand exchange reaction between QDs and thiol, mercaptoethanol (1 mM - 90 mM) was added to the suspension of QDs (56 mg/mL). The ^{31}P NMR spectra were obtained with a 400 MHz Bruker Advance spectrometer. Deuteriochloroform (CDCl_3) was used as a solvent, and phosphoric acid served as an external standard. **RESULTS:** Figure 1B shows representative ^{31}P NMR spectra of QDs in the absence and presence of mercaptoethanol (thiol) as well as a spectrum of pure TOPO in CDCl_3 . The spectra of QDs did not display any obvious peak related to phosphorus containing species when the concentration of thiol is very low (less than 10 mM). With increasing concentration of added thiol, sharp peaks related to free phosphorus containing species were observed. When the concentration of thiol was 15 mmol/L, a sharp peak around 45.5 ppm could be detected indicating that a phosphorus containing species was cleaved from QDs by the action of thiol. The chemical shift of cleaved phosphorus containing species is close to that of free TOPO measured at the present condition (48.4 ppm). Thus, the peak around 45.5 ppm was tentatively assigned to the cleaved TOPO from the surface of QDs. **CONCLUSIONS:** ^{31}P NMR was used to detect the ligand exchange reaction between thiol and TOPO stabilized QDs. This study demonstrates that TOPO-QDs are relatively unstable and that TOPO can be cleaved from QDs in the presence of a nucleophilic agent such as thiol, which is widely distributed in tissue and physiological fluids. Thus, TOPO coated QDs may be unsafe for *in vivo* applications in humans and animals because of the potential release of toxic cadmium ions under physiological conditions. This research provides preliminary information about the potential risk presented by the degradation of TOPO-QDs in physiological systems. Further, ^{31}P NMR may be employed to monitor the cleavage of TOPO from TOPO-QDs and assess their stability *in vivo*.

ACKNOWLEDGMENT: This work was supported by DOD BC094936 and BC094963, and NIH/NCRR/RCMI 2G12 RR003048.

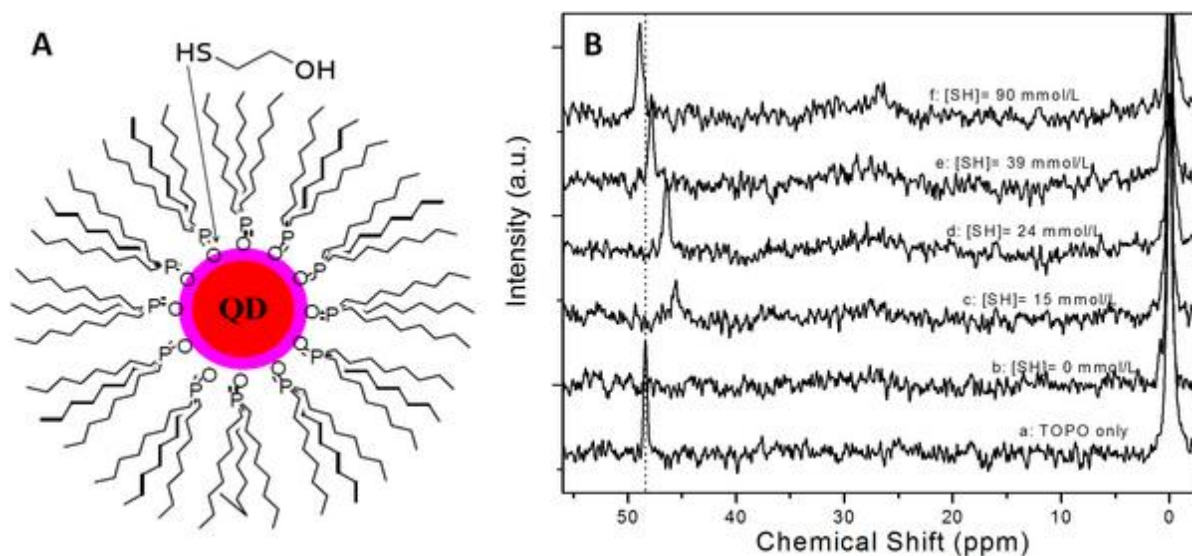


Figure 1. A: Nucleophilic attack of thiol on TOPO-QDs which leads to cleavage of TOPO from the surface of QDs. B: ^{31}P NMR spectra of QDs in the absence and presence of different concentration of thiol as well as that of pure TOPO in CDCl_3 .

Disclosure of author financial interest or relationships:

A.V. Korotcov, None; **T. Wang**, None; **Y. Chen**, None; **R. Sridhar**, None; **J. Mitchell**, None; **P.C. Wang**, None.

Anti-PSMA Fold-back Diabody Fusion Diphtheria Immunotoxin Expresses Selectivity for Prostate Cancer Imaging and Therapy

Fayun Zhang^{1,2}, Liang Shan^{1,3}, Yuanyi Liu⁴, David Neville⁴, Yue Chen¹, Alexandru Korotcov¹, Stephen Lin¹, Sophia Huang¹, Rajagopalan Sridhar¹, Wei Liang², Paul C Wang¹

¹Molecular Imaging Lab, Radiology, Howard University, Washington, D.C., 20060.

²Protein & Peptide Pharmaceutical Laboratory, National Laboratory of Biomacromolecules, Institute of Biophysics, Chinese Academy of Sciences, Beijing, China, 100101.

³National Institutes of Health, Bethesda, Maryland, 20892.

⁴Angimmune LLC, Bethesda, Maryland, 20852

Abstract

Over expression of prostate specific membrane antigen (PSMA) is characteristic of certain prostate, breast and ovarian tumors. PSMA expression occurs in tumor cells and in the neovascular endothelium of certain solid tumors. An immunotoxin generated by fusing the fold-back of two single chain Fv fragments of anti-PSMA monoclonal antibody with the catalytic and translocation domains of diphtheria toxin (A-dmDT(390)-scfbDb(PSMA)), may be suitable for targeted therapy of tumors that overexpress PSMA. In this study, two types of prostate cancer, a PSMA positive and a PSMA negative cancers, were treated with (A-dmDT(390)-scfbDb(PSMA) in order to study the tumor targeting and therapeutic potential of the immunotoxin. Cellular uptake and selective toxicity of A-dmDT(390)-scfbDb(PSMA) was evident in monolayer cultures of PSMA-positive LNCap prostate cancer cells but not in cultures of PSMA-negative PC-3 prostate cancer cells. Cellular accumulation of A-dmDT(390)-scfbDb(PSMA) increased with increasing incubation time or concentration in LNCaP cells and an increase in proportion of apoptotic LNCaP cells occurred with increasing dose of the fold-back immunotoxin. A-dmDT(390)-scfbDb(PSMA) labeled with Alexa 680 was utilized in conjunction with MRI and optical imaging *in vivo* to non invasively demonstrate the specific targeting and therapeutic efficacy towards PSMA positive LNCaP solid tumor xenografts in athymic nude mice.

Keywords:

prostate-specific membrane antigen (PSMA); fold back single chain Fv antibody fragments diabody (scfbDb); diphtheria immunotoxin DT390; prostate cancer therapy; optical imaging; specific tumor targeting

I. INTRODUCTION

Prostate cancer is the most common solid tumor and one of the leading causes of cancer-related death among American men^[1]. Radiotherapy and/or surgery with or without androgen deprivation are used for management of early stage organ confined prostate cancer. A subset of patients diagnosed with early stage cancer may progress to a more aggressive metastatic stage of the disease, which does not respond to androgen deprivation. Chemotherapeutic approaches are used for treating metastatic prostate cancer. The development of androgen resistance and systemic off-target toxicities of conventional cancer chemotherapeutic drugs such as docetaxel and mitoxantrone are major clinical challenges^[2-3]. There is a need for safe and effective therapies based on specific and selective targeting of tumor. Tumor cells often express surface receptors or other molecules that distinguish them from other cells. Ligands designed to bind tumor specific receptors can be conjugated to cytotoxic drugs or toxins and the resulting conjugates provide a tumor targeted drug delivery system for safe and effective therapy^[4]. Further research along these lines may lead to molecularly targeted individualized therapy. Prostate-specific membrane antigen (PSMA) is overly expressed on the surface of certain prostate, breast and ovarian cancer cells. It is noteworthy that PSMA expression particularly pronounced when prostate cancer enters late stage and becomes androgen-independent and metastatic^[5]. PSMA expressed in certain prostate cancer cells is 1000-fold higher than in normal prostate tissue^[6]. PSMA is also expressed on the neovascular endothelium in a wide variety of human solid tumors, but is not expressed in the blood vessels of normal tissue^[7]. These findings have prompted the use of monoclonal antibody of PSMA for sensitive and specific tumor imaging techniques^[8] as well as specific targeted drug delivery for treatment of prostate cancer^[9]. PSMA antibody or its fragments, such as single-chain antibody fragments (scFv), can deliver cytotoxic agents to be internalized in PSMA-expressing cells^[10]. scFv is the smallest functional component of an antibody, which consists of the heavy chain (V_H) and the light chain (V_L) connected by a flexible peptide linker. Due to the small size of scFv, it has shown better tumor penetration, improved tumor distribution, and faster blood clearance characteristics than a full antibody. It has been used as a ligand for targeted drug delivery^[11].

The truncated form of diphtheria toxin (DT390) construct incorporated in the immunotoxin has shown targeted cellular toxicity^[12-13] and bioactivity *in vivo*^[14-15]. The anti-T cell immunotoxin A-dmDT390-bisFv(UCHT1), which is based on DT390, shows binding activity to T cells^[16] and has undergone preclinical studies and clinical trial^[17-18]. The immunotoxin of the fold-back single-chain diabody format of anti-monkey CD3 fused with DT390 was constructed based on the established DT390/*Pichia* expression platform (U.S. Patent Application No. 60/953,416), and has shown a 5 to 7-fold enhanced bioactivity over DT390-bisFv to T cells^[19]. To effectively deliver DT390 and enhance the specificity of its targeting for PSMA expressing cells, we have constructed an anti-PSMA bisFv fold-back format diabody (scfbDb) and immunotoxin (A-dmDT390-scfbDb) using a similar approach. The scfbDb construction was based on the scFv fragment sequences of murine J591 anti-PSMA mAb. As shown in Fig. 1A, the anti-PSMA diabody consists of two scFv fragments separated by optimized lengths of Gly-Ser linkers. The immunotoxin is composed of a dmDT moiety and the anti-PSMA scfbDb, in the sequence of dmDT-L1- V_L -L1- V_H -L2- V_L -L1- V_H . The G_4S and $(G_4S)_3$ are the linkers, L1 and L2. V_L and V_H are the variable domains of light and heavy chains (Fig. 1B). The structure of the A-dmDT390-scfbDb immunotoxin is shown in Fig. 1C. Preliminary studies showed that scfbDb

binds to the extracellular domain of PSMA with a higher affinity than bscFv and scFv formats at a ratio of 7:2.5:1 (scfbDb:bscFv:scFv). This finding indicates that the scfbDb has greater potential to be more sensitive and specific for targeted imaging and therapy applications. Earlier *in vitro* study has demonstrated that the diabody efficiently mediates the entry of the truncated toxin across the cell membrane into the cytosol. The fold-back format immunotoxin was 18-30 fold more potent than the bscFv format against monolayer LNCaP cancer cells.

In this study, A-dmDT(390)-scfbDb(PSMA) was conjugated to Alexa Fluor 680 dye to obtain near infrared labeled immunotoxin. The near infrared labeled immunotoxin was then used to investigate its utility for tumor specific imaging and tumor inhibitory efficacy against prostate cancer cells grown as monolayer cultures and as solid tumor xenografts in athymic nude mice. The results demonstrate that A-dmDT(390)-scfbDb(PSMA) immunotoxin has selective tumor targeting property in addition to a distinct and potent anticancer activity against PSMA-positive prostate cancer.

II. MATERIALS AND METHODS

Cell Lines

Human prostate cancer cell lines LNCaP and PC-3 were purchased from ATCC (American Type Culture Collection, Manassas, VA). LNCaP and PC-3 cells were maintained as exponentially growing monolayer cultures in RPMI 1640 medium and DMEM medium, respectively. Both media were supplemented with L-glutamine (2mM), 50µg/ml each of penicillin and streptomycin, and 10% heat-inactivated fetal bovine serum. The cells were maintained in culture at 37 °C with 5% CO₂ and 95% humidity.

Cellular PSMA staining

LNCaP and PC-3 cells were suspended in 8-well chamber slide with 1×10^4 cells in 0.5 ml medium in each well. After 24 hours, the cells were washed with DPBS and fixed in 3.7% paraformaldehyde. The cells were permeabilized with 0.2% Triton-X 100 and blocked with 1% bovine serum albumin in HBSS for 1 hour. The cells were then incubated with a rabbit monoclonal anti-PSMA antibody (Abcam, Cambridge, MA) at a dilution of 1:200 to a final concentration of 1 µg/ml. After washing the cells with HBSS, goat anti-rabbit immunoglobulin G conjugated with Alexa Fluor 488 (Invitrogen, Carlsbad, CA) was added to the blocking solution at a final concentration of 2 µg/ml and incubated at room temperature for 1 hour in dark. The slides were washed three times in PBS, and examined by fluorescent microscopy.

Western Blot Analysis

LNCaP and PC3 cells were washed with DPBS and lysed with RIPA lysis and extraction buffer (Pierce Biotech, Rockford, IL). Protein concentrations were determined using the Bio-Rad Protein Assay Dye Reagent Concentrate (Bio-Rad, Hercules, CA). Whole-cell lysate (50 µg) was separated by 8% SDS gel electrophoresis and transferred to PVDF membranes. The membranes were blocked using 5% nonfat milk and probed separately for two hours at room temperature with primary antibodies for PSMA (Abcam, Cambridge, MA) and β-Actin (Santa Cruz Biotechnology, Santa Cruz, CA). Then the membranes were washed and probed with a 1:2,000

dilution of peroxidase-conjugated secondary antibody, and detected by enhanced chemiluminescence (Amersham Life Sciences, Amersham, UK).

Cell Viability Assays

Cells were seeded in 96-well plates and cultured for 24 hours. The cells were then exposed to a graded range of concentrations (from 0 nM to 5 nM) of A-dmDT90(390)-scfbDb(PSMA) for 48 hours. The viability of cells was measured using the methylthiazole tetrazolium (MTT) assay. One hundred microliters of MTT solution (0.5 mg/ml in PBS) were added to each well. The plates were incubated for 4 hours at 37 °C, and then 100 µl of dimethyl sulfoxide were added to each well for 10 minutes at room temperature. The absorbance was measured at 570 nm using a plate reader. IC₅₀ of immunotoxin was calculated using the SPSS software for performing statistical analysis.

Endocytosis and quantification of A-dmDT90(390)-scfbDb(PSMA) in cells

A-dmDT90(390)-scfbDb(PSMA) was labeled with Invitrogen Alexa Fluor 680 Protein labeling kit A20172 to determine the endocytosis and quantification of A-dmDT90(390)-scfbDb(PSMA) in the cells. LNCaP and PC-3 prostate cancer cells grown to 60 to 70% confluence on four-chamber glass slides were used for endocytosis analysis. The cells were incubated with 0.1 µM of Alexa Fluor 680-labeled A-dmDT90(390)-scfbDb(PSMA) in complete medium for different durations (from 10 minutes to 3 hours), or incubated with a different concentrations of Alexa Fluor 680-labeled A-dmDT90(390)-scfbDb(PSMA) (from 0.01 µM to 0.1 µM) for 3 hours. After removal of the media, the cells were washed three times using DPBS, fixed with 10% formalin for 10 minutes, stained with DAPI for 5 minutes, and rinsed 3 times with DPBS. The cells were then observed under the fluorescent microscope. For the quantitative measurement of Alexa Fluor 680-labeled A-dmDT90(390)-scfbDb(PSMA), a BD flow cytometer (Becton Dickinson, San Jose, CA) with excitation/emission: 635 nm/679 nm was used.

Assessment of apoptosis

Annexin V binding was used for estimating apoptosis in cells using fluorescence microscopy. Cells were first exposed to a DNA-binding dye, propidium iodide (PI), to detect sub-diploid population. The two prostate cancer cell lines (LNCaP and PC-3) were treated with 0.1, 0.5, and 1 nM of A-dmDT90(390)-scfbDb(PSMA) immunotoxin for 24 hours. Then the cells were harvested by trypsinization, collected by centrifugation, and washed with DPBS. The collected cells were fixed with 70% ethanol for 1 hour at 4°C. The fixed cells were washed twice in PBS and then incubated with a solution containing 100 µg/mL RNase at 37°C water bath for 30 minutes, and then gently resuspended in 1 mL of PI solution (50 µg/mL with 3.8 mM sodium citrate in PBS). Lastly the cells were incubated for 15 minutes in the dark at room temperature and analyzed using flow cytometry. The red fluorescence due to the PI staining of individual cells was collected. Ten thousand cells of each sample were counted. For fluorescence microscopy detection, 10,000 LNCaP cells were planted onto a 8-well chamber slide for 24 hours. After incubation with different concentrations of A-dmDT90(390)-scfbDb(PSMA) for 48 hours, the cells were incubated with 500 µl of 1X Annexin V Binding Buffer. 5 µl of Annexin V-FITC and 5 µl of PI (Abcam, Cambridge, MA) were added onto the cells, and cells were fixed in 2% formaldehyde before visualization. The fixed cells were examined under a fluorescence microscope using separate filters for FITC and rhodamine/PI. The cells that had bound Annexin V-FITC, which had undergone apoptosis, showed green staining on the plasma membrane,

whereas the cells that had lost membrane integrity due to necrosis showed red PI staining throughout the nuclei. To further determine cytotoxicity of A-dmDT90(390)-scfDb(PSMA), the cells were routinely examined using trypan blue staining and light microscopy. The cells permeable to trypan blue were considered nonviable.

Animal Tumor Model and Optical Imaging

All animal studies were carried out in accordance with the guidelines of the Howard University Institutional Animal Care and Use Committee. Five-week-old athymic male nude mice were inoculated subcutaneously of 5×10^6 LNCaP cells or 2×10^6 PC-3 cells mixed with 0.2 ml of matrigel (BD Biosciences, Bedford, MA) into the lower left flank. The tumors were grown to reach 5-7 mm in diameter for imaging study. Six mice with LNCaP tumors and four mice with PC-3 tumors were used for testing the detection sensitivity of imaging and dynamic uptake of Alexa Fluor 680-labeled A-dmDT90(390)-scfDb(PSMA) *in vivo*. Three mice with LNCaP tumors and three mice with PC-3 tumors were used to test specific targeting of Alexa Fluor 680-labeled A-dmDT90(390)-scfDb(PSMA). Two mice with LNCaP tumors and two mice with PC-3 tumors were given sham injections of PBS and served as controls.

In vivo fluorescence imaging of tumor bearing mice was performed using the IVIS 200 Imaging System and Living Image software (Caliper Life Sciences, Hopkinton, MA). The mice were placed on a warmed (25°C) stage inside a light-tight camera box with continuous exposure to 2% isoflurane. The mice were given 100 μL (200 $\mu\text{g/mL}$; 2.06 μM) of the Alexa Fluor 680 labeled A-dmDT90(390)-scfDb(PSMA) or 100 μL (4.12 μM ; one molecule of immunotoxin labeled with two molecules of Alexa Fluor 680 dye) of Alexa Fluor 680 dye *via* tail vein injection. The mouse was imaged every 10 minutes for the first hour and then imaged every hour for 24 hours. The acquisition time for each image was 2 seconds. Regions of interest around tumor sites from the displayed images were identified and emitted light was measured. The signal intensity was expressed as mean flux in photons/second/ cm^2 /steradian (p/s/ cm^2 /sr). The contralateral non tumor bearing leg muscle was selected as a normal background.

Evaluation of Therapeutic Efficacy

Tumor xenograft models were developed by subcutaneous inoculation of 5×10^6 LNCaP cells or 2×10^6 PC-3 cells mixed with 0.2 ml of matrigel (BD Biosciences, Bedford, MA) into the lower left flank of five weeks old male athymic nude mice. LNCaP tumors were allowed to develop for six weeks and PC-3 tumors for 3 weeks to reach the diameter of about 5 mm. The mice with LNCaP tumors or PC-3 tumors were divided randomly into two groups ($n = 10$), respectively. 5 μg of A-dmDT90(390)-scfDb(PSMA) immunotoxin or BSA diluted in DPBS was administered via *i.p.* injection to the animals twice a day at 6 hour intervals (10 am and 4 pm) for 6 days. Tumor growth was monitored with MR imaging twice a week. The mice were anesthetized with a 2% Isoflurane with oxygen, positioned in the MR probe, and taped with polyurethane foam to avoid involuntary motion. A Bruker 400MHz NMR machine (Bruker-Biospin, Billerica, MA) was used for MRI. A rapid acquisition with refocused echoes (RARE) sequence (TE=39.19ms, TR=3600ms, 12 averages) was used to acquire T2-weighted coronal images. The imaging parameters were: echo time (TE) 7.838 ms, RARE factor 16, effective TE 39.19 ms, repetition time (TR) 3600 ms, number of averages 12, field-of-view 27.0 mm x 25.6 mm, matrix size 192 x 256, and slice thickness 0.5 mm. The MIPAV software (CIT/NIH, Bethesda, MD) was used for image analysis. The tumor was manually segmented in each MR

image, the numbers of voxels within the boundary of tumor were counted and the total tumor volume was calculated. The life span of the mice given different treatment regimen was recorded.

Statistical Analysis

Statistical analysis tests were performed with the Student's *t*-test. Survival was assessed with the Kaplan – Meier method. A significant correlation was inferred if a *p* value was < .05 by correlation analysis. All statistical tests were two-sided.

III. RESULTS

PSMA expression is strong in LNCaP but not in PC-3 Cells

The expression of PSMA was determined by immunofluorescence staining and Western blotting in LNCaP and PC-3 cells. The results showed high levels of PSMA expression in LNCaP cells, but not in PC-3 cells (Figure 2).

A-dmDT90(390)-scfbDb(PSMA) Inhibits Proliferation of LNCaP Cells.

The inhibitory effects of A-dmDT90(390)-scfbDb(PSMA) on the growth and viability of LNCaP cells and PC-3 cells were investigated using MTT assay. Cells were treated with different concentrations of A-dmDT90(390)-scfbDb(PSMA) immunotoxin for 48 hours. LNCaP cells were found to be very sensitive to A-dmDT90(390)-scfbDb(PSMA) immunotoxin; administration of a low concentration (0.57 nM) resulted in 50% cell death (Fig. 3). However, the viability of PC-3 cells was not affected by the immunotoxin even at a relatively high concentration of 100 nM.

Cellular Uptake and Accumulation is High in LNCaP cells but not in PC3 Cells

A-dmDT90(390)-scfbDb(PSMA) was labeled with a near infrared (NIR) tag using an Alexa Fluor 680 Protein Labeling Kit (Invitrogen Co.). The cellular uptakes and accumulations of the resulting Alexa Fluor 680 labeled immunotoxin by LNCaP cells or PC-3 cells were detected by incubating cell cultures with the near infrared (NIR) labeled immunotoxin followed by imaging with fluorescence microscopy and flow cytometry assays. As shown in Fig. 4, the intensity of Alexa Fluor 680 fluorescence in red color increased with increasing concentration of NIR labeled A-dmDT90(390)-scfbDb(PSMA) from 0.01 μ M to 0.1 μ M. Similarly, increased red fluorescence was observed in LNCaP cells treated with 0.1 μ M of labeled A-dmDT90(390)-scfbDb(PSMA) when incubated for longer periods (Fig. 5). However, no red fluorescence could be detected in PC-3 cells after incubation with labeled A-dmDT90(390)-scfbDb(PSMA), even with a relatively high concentration 0.2 μ M for 4 hours (Fig. S1). The flow cytometry assay was used to quantify the cellular uptake of the immunotoxin. As shown in Fig. 6, an increase in concentration or incubation time caused more accumulation of A-dmDT90(390)-scfbDb(PSMA) in LNCaP cells. LNCaP cells showed a significant shift in the flow cytometry profile after incubation with 0.1 μ M of A-dmDT90(390)-scfbDb(PSMA) for 6 hours but not in PC-3 cells (Fig. S2).

A-dmDT90(390)-scfbDb(PSMA) induces apoptosis of LNCaP prostate cancer cells.

LNCaP cell cultures were incubated with A-dmDT90(390)-scfbDb(PSMA) (from 0 to 5 nM) for 24 hours and stained with PI, which binds to DNA. The fraction of cells with sub-

diploid DNA content was measured by PI fluorescence. As shown in Fig. 7A, the treatment with increasing doses of unlabeled immunotoxin resulted in dose dependent increases in the S phase population with concomitant decreases in the G2 phase population of LNCaP cells. However, this effect of the immunotoxin was not evident in PC-3 cells. Similarly, trypan blue dye staining showed a significantly increased staining of nonviable cells in LNCaP cultures, but not in PC-3 cell cultures treated with the immunotoxin. FITC labeled annexin V antibody was used for staining apoptotic cells. Light microscopy also showed a higher rate of apoptosis in the LNCaP cells after incubation with increased amount of A-dmDT90(390)-scfbDb(PSMA) (Fig. 7B). Fluorescence microscopy showed an increase of green fluorescence on the cell membrane due to apoptosis (FITC labeled annexin V antibody binding by cell membranes of apoptotic cells) as the concentration of the immunotoxin was increased from 0.1 nM to 1 nM. The green fluorescence decreased and red fluorescence (due to DNA binding to PI in necrotic cells) increased when cells were treated at 5 nM and 10 nM immunotoxin (Fig. 7B).

A-dmDT90(390)-scfbDb(PSMA) is better for targeting LNCaP than PC-3 solid tumor xenografts in live mice.

LNCaP cells and PC-3 cells were implanted on the lower left flank of athymic nude mice to test the imaging efficiency of A-dmDT90(390)-scfbDb(PSMA) in prostate tumors. The tumor was allowed to grow to about 5 mm in diameter. One hundred microliters (200 µg/mL) of Alexa Fluor 680 labeled A-dmDT90(390)-scfbDb(PSMA) or Alexa Fluor 680 dye was administrated as a single bolus via the tail vein injection. The whole animal was then imaged at different time points. As shown in Figure 8, an increased accumulation of the fluorescence from the labeled immunotoxin was detectable as early as 30 minutes in most LNCaP tumors. The near infrared fluorescent signal in LNCaP tumors showed an increase during the first 6 hours, followed by a gradual decrease (Fig. 8A). The signal from the Alexa Fluor 680 dye was rapidly detectable around the whole body. However, no obvious accumulation of Alexa Fluor 680 dye was observed in the tumors (Fig. 8B). In PC-3 tumors, neither Alexa Fluor 680 labeled A-dmDT90(390)-scfbDb(PSMA) nor Alexa Fluor 680 dye showed any targeting to and accumulation in the tumors (Fig. S3).

A-dmDT90(390)-scfbDb(PSMA) inhibition LNCaP tumor growth

The selective tumor specific inhibitory effect of A-dmDT90(390)-scfbDb(PSMA) was studied on the PSMA positive LNCaP tumors and the PSMA negative PC-3 tumors grown as solid tumor xenografts in athymic nude mice. Each mouse was given 10 µg A-dmDT90(390)-scfbDb(PSMA) *via* i.p. injection for six consecutive days. MRI was used to monitor the tumor growth twice a week after the injection. A-dmDT90(390)-scfbDb(PSMA) significantly inhibited LNCaP tumor growth, however, it did not affect PC-3 (Fig. 9 A and B). The average LNCaP tumor weight for the treatment group was 0.27 ± 0.09 g, which was significantly lower than the tumor weight of the untreated control group 0.67 ± 0.11 g (Fig. 9 C). The average weight of the treated PC-3 tumors were not significantly different from the average weight of sham treated PC-3 tumors in the control group (Fig. 9C). There was no difference in body weights between the LNCaP tumor bearing mice and PC-3 tumor bearing mice whether the animals were treated or not with the immunotoxin.

IV. DISCUSSION

PSMA is known to be highly expressed and rapidly internalized in malignant prostate cancer. However, it is minimally expressed in benign cancer or in normal tissues. The PSMA antibody fragment scFv has been used to bind specifically to prostate cancer cells for prostate cancer therapy^[20-21] and some PSMA targeted therapeutics have been investigated in clinical trials^[22-23]. In this study, we have demonstrated that the conjugate of a fold-back single chain Fv fragments of anti-PSMA monoclonal antibody with the catalytic and translocation domains of diphtheria toxin (A-dmDT90(390)-scfbDb(PSMA)) exhibits growth inhibitory effect on PSMA-positive LNCaP cancer cells both *in vitro* and *in vivo* but not in PSMA negative PC-3 cells. The selective toxicity towards LNCaP cells indicates that the fold back scFv of anti-PSMA antibody binds specifically to the PSMA antigen on cell membrane and effectively delivers DT390 into PSMA expressing cells to induce cytotoxicity. Diphtheria toxin (DT) exerts its toxicity towards eukaryotic organisms through inactivation of the polypeptide chain EF-2 (Elongation Factor 2). The inactivation results in inhibition protein synthesis and induction of apoptosis^[24]. As a truncated form of diphtheria toxin, DT390 is widely known for inducing cellular toxicity through targeted delivery via a ligand component. The immunotoxins constructed with DT390 are reported to have high toxicity to activated T cells^[14, 25]. However, little is known about the process of targeted cell apoptosis induced by DT390 in tumor cells. In this study, the immunotoxin of A-dmDT90(390)-scfbDb(PSMA) induced more apoptosis in PSMA positive LNCaP cells. The sub-diploid population assay showed that the immunotoxin induced an increase in S phase population and a decrease in G2 phase population in LNCaP cell cultures. These data provide a better understanding of the mechanism of tumor specific toxicity of the immunotoxin *in vitro*.

In this study, near infrared fluorescent imaging has been used to confirm the specific *in vivo* tumor targeting effectiveness of the immunotoxin in LNCaP tumors that are known to over express PSMA. Optical imaging provides a dynamic, noninvasive real-time *in vivo* imaging technique for monitoring the uptake of fluorescent probes in tumor bearing animals. It can be used for monitoring gene delivery and tumor detection^[26-27]. As Figure 8 shows, fluorescence emission from A-dmDT90(390)-scfbDb(PSMA) immunotoxin indicated fast accumulation of immunotoxin in LNCaP tumors, while no signal was detected in PC-3 tumors which are deficient in PSMA. High intensity of fluorescent signals from Alexa Fluor 680 labeled A-dmDT90(390)-scfbDb(PSMA) immunotoxin were also observed in the kidneys and liver, which indicates the potential for systemic off-target toxicity. However, the *in vivo* study showed although the A-dmDT90(390)-scfbDb(PSMA) immunotoxin significantly inhibited LNCaP tumor growth it does not induce weight loss (Fig. 9). The selective cytotoxicity of A-dmDT90(390)-scfbDb(PSMA) immunotoxin both *in vitro* (Fig. 3) and *in vivo* (Fig. 9) demonstrates the immunotoxin can only selectively bind to, and be internalized into PSMA-expressing cells. Non-PSMA expressing cells such as in kidney or liver do not internalize the immunotoxin and did not cause systemic toxicity or adverse effects in mice.

This selective targeting is considered to be the reason for A-dmDT90(390)-scfbDb(PSMA) having an inhibitory effect on PSMA positive LNCaP tumor growth but not on PSMA negative PC-3 tumor. The findings suggest this immunotoxin construct incorporating fold-back of two single chain Fv fragments of anti-PSMA antibody and diphtheria toxin attached with fluorophore has considerable promise and potential in the clinic for prostate cancer

treatment and non invasive *in vivo* therapeutic monitoring of the NIR labeled immunotoxin delivery and distribution.

Although there are a few clinical trials evaluating clinical potentials of immunotoxins derived from PSMA antibody, there is none that explores the clinical potential of the immunotoxin used in this study for treatment of prostate cancer. An important finding of this study is the efficacy of the immunotoxin against PSMA positive prostate cancer cells and the lack of binding and therapeutic effect against PSMA negative prostate cancer cells. This suggests that inappropriate use of this immunotoxin for treating PSMA negative tumors may run the risk of unintended systemic toxicity. It is imperative to confirm the presence of PSMA positive tumors before initiating therapy with the immunotoxin used in our studies. It is interesting to note that not all prostate cancer cells respond to the cytotoxic effects of A-dmDT90(390)-scfbDb(PSMA) , the immunotoxin with specificity for PSMA positive tumors.

ACKNOLEGEMENT

This work was supported in part by grant 2 G12 RR003048 from the RCMI Program, Division of Research Infrastructure, and the DOD USAMRMC W81XWH-10-1-0767 grant.

REFERENCES

1. Jemal A, Siegel R, Ward E, Hao Y, Xu J, Murray T, Thun MJ. Cancer statistics, 2008. *CA Cancer J. Clin.* 2008;58(2):71–96.
2. Sternberg CN. Systemic chemotherapy and new experimental approaches in the treatment of metastatic prostate cancer. *Ann. Oncol.* 2008; 19 Suppl 7: vii91–5.
3. Pronk LC, Hilken PH, van den Bent MJ, van Putten WL, Stoter G et al. Corticosteroid co-medication does not reduce the incidence and severity of neurotoxicity induced by docetaxel. *Anticancer Drugs* 1998; **9**: 759–64.
4. Allen, T. M. Ligand-targeted therapeutics in anticancer therapy. *Nat. Rev. Cancer* 2002; 2:750–63.
5. Fair WR, Israeli RS, Heston WD. Prostate-specific membrane antigen. *Prostate* 1997;32(2):140–8.
6. Slovin SF. Targeting novel antigens for prostate cancer treatment: focus on prostate-specific membrane antigen. *Expert Opin Ther Targets* 2005;9(3):561–70.
7. Chang SS, O’Keefe DS, Bacich DJ, Reuter VE, Heston WD, Gaudin PB. Prostate-specific membrane antigen is produced in tumor-associated neovasculature. *Clin Cancer Res.* 1999;5(10):2674–81.
8. Foss CA, Mease RC, Fan H, Wang Y, Ravert HT, Dannals RF, Olszewski RT, Heston WD, Kozikowski AP, Pomper MG. Radiolabeled small-molecule ligands for prostate-specific membrane antigen: in vivo imaging in experimental models of prostate cancer. *Clin Cancer Res* 2005;11(11):4022–8.
9. Fracasso G, Bellisola G, Cingarlini S, Castelletti D, Prayer-Galetti T, Pagano F, Tridente G, Colombatti M. Anti-tumor effects of toxins targeted to the prostate specific membrane antigen. *Prostate* 2002;53(1):9–23.
10. Schulke N, Varlamova OA, Donovan GP, Ma D, Gardner JP, Morrissey DM, Arrigale RR, Zhan C, Chodera AJ, Surowitz KG, MaddonPJ, HestonWD,OlsonWC. The homodimer of prostatespecific membrane antigen is a functional target for cancer therapy. *Proc Natl Acad Sci USA* 2003;100(22):12590–5.
11. Wu AM, Senter PD. Arming antibodies: Prospects and challenges for immunoconjugates. *Nat Biotechnol* 2005;23(9):1137–46.
12. Arora N, Masood R, Zheng T, Cai J, Smith DL, Gill PS. Vascular endothelial growth factor chimeric toxin is highly active against endothelial cells. *Cancer Res.* 1999;59(1):183-8.
13. Liu YY, Gordienko I, Mathias A, Ma S, Thompson J, Woo JH, Neville DM.. Expression of an anti-CD3 single-chain immunotoxin with a truncated diphtheria toxin in a mutant CHO cell line. *Protein Expr Purif.* 2000;19:304–11.
14. Jia Y, Li H, Chen W, Li M, Lv M, Feng P, Hu H, Zhang L. Prevention of murine experimental autoimmune encephalomyelitis by in vivo expression of a novel recombinant immunotoxin DT390-RANTES. *Gene Therapy.* 2006;13:1351–9
15. Chan CH, Blazar BR, Greenfield L, Kreitman RJ, Vallera DA. Reactivity of murine cytokine fusion toxin, diphtheria toxin390-murine interleukin-3 (DT390-mIL-3), with bone marrow progenitor cells. *Blood.* 1996;88(4):1445-56.
16. Wang Z, Kim GB, Woo JH, Liu YY, Mathias A, Stavrou S, Neville DM Jr. Improvement of a recombinant anti-monkey anti-CD3 diphtheria toxin based immunotoxin by yeast display affinity maturation of the scFv. *Bioconjug Chem.* 2007;18(3):947-55.

17. Woo JH, Bour SH, Dang T, Lee YJ, Park SK, Andreas E, Kang SH, Liu JS, Neville DM Jr, Frankel AE. Preclinical studies in rats and squirrel monkeys for safety evaluation of the bivalent anti-human T cell immunotoxin, A-dmDT390-bisFv(UCHT1). *Cancer Immunol Immunother.* 2008;57(8):1225-39.
18. Woo JH, Lee YJ, Neville DM, Frankel AE. Pharmacology of anti-CD3 diphtheria immunotoxin in CD3 positive T-cell lymphoma trials. *Methods Mol Biol.* 2010;651:157-75.
19. Kim GB, Wang Z, Liu YY, Stavrou S, Mathias A, Goodwin KJ, Thomas JM, Neville DM A fold-back single-chain diabody format enhances the bioactivity of an anti-monkey CD3 recombinant diphtheria toxin-based immunotoxin. *Protein Eng Des Sel.* 2007;20(9):425-32.
20. Liu C, Hasegawa K, Russell SJ, Sadelain M, Peng KW. Prostate-specific membrane antigen retargeted measles virotherapy for the treatment of prostate cancer. *Prostate.* 2009;69(10):1128-41.
21. Fortmüller K, Alt K, Gierschner D, Wolf P, Baum V, Freudenberg N, Wetterauer U, Elsässer-Beile U, Bühler P. Effective targeting of prostate cancer by lymphocytes redirected by a PSMA \times CD3 bispecific single-chain diabody. *Prostate.* 2011;71(6):588-96.
22. Nanus DM, Milowsky MI, Kostakoglu L, Smith-Jones PM, Vallabahajosula S, Goldsmith SJ, Bander NH. Clinical use of monoclonal antibody HuJ591 therapy: Targeting prostate specific membrane antigen. *J Urol* 2003;170(6 Pt 2):S84–8; discussion S88–9.
23. Olson WC, Heston WD, Rajasekaran AK. Clinical trials of cancer therapies targeting prostate-specific membrane antigen. *Rev Recent Clin Trials* 2007;2(3):182–190.
24. Kochi SK, Collier RJ. DNA fragmentation and cytolysis in U937 cells treated with diphtheria toxin or other inhibitors of protein synthesis. *Exp Cell Res.* 1993;208(1):296-302.
25. Jia J, Li H, Tai S, Lv M, Liao M, Yang Z, Zhang B, Zhou B, Zhang G, Zhang L. Construction and preliminary investigation of a plasmid containing a novel immunotoxin DT390-IL-18 gene for the prevention of murine experimental autoimmune encephalomyelitis. *DNA Cell Biol.* 2008;27(5):279-85.
26. Veiseh M, Gabikian P, Bahrami SB, et al. Tumor paint: a chlorotoxin: Cy5.5 bioconjugate for intraoperative visualization of cancer foci. *Cancer Res* 2007;67:6882–8.
27. Kaijzel EL, van der Pluijm G, Lowik CW. Whole-body optical imaging in animal models to assess cancer development and progression. *Clin Cancer Res* 2007;13:3490–7.

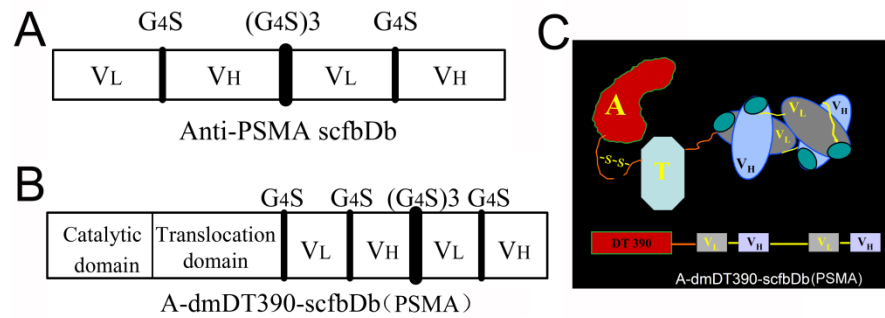


Figure. 1 The scheme of A-dmDT390-scfbDb comprising a dmDT moiety and the anti-PSMA scfbDb. (A): The diabody consists of two scFv fragments separated by optimized lengths of Gly-Ser linkers. (B): The immunotoxin comprises a dmDT moiety and the anti-PSMA scfbDb. The sequence from left to right is dmDT- VL-L1-VH-L2-VL-L1-VH. Here G4S are linkers, and VL and VH are the variable domains of light and heavy chains. (C): The 3D structures of A-dmDT390-scfbDb immunotoxin.

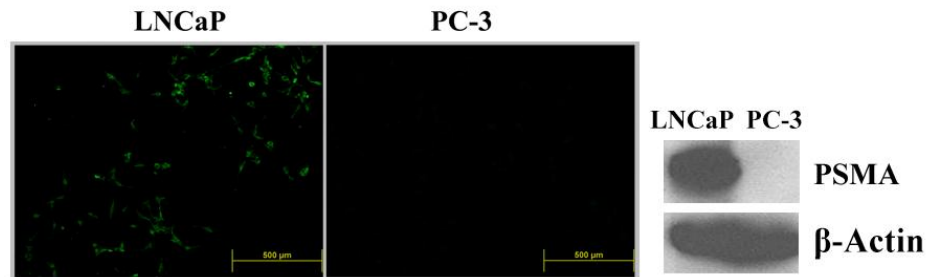


Figure. 2 Expression of PSMA in prostate cancer cells. Left: LNCaP and PC-3 cells were fixed on slides, incubated with PMSA antibody and then with FITC labeled second antibody (Green). Right: Total cell lysates from LNCaP and PC-3 cells were analyzed by Western blot.

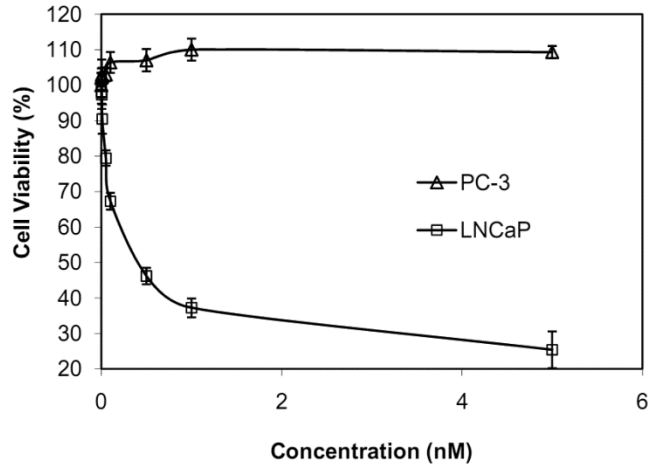


Figure 3. Cytotoxic effect of A-dmDT90(390)-scfbDb(PSMA) towards LNCaP cells and PC-3 cells. The viability of PSMA-positive (LNCaP) and PSMA-negative (PC-3) cells was determined by MTT assay after 48-hr treatment with A-dmDT90(390)-scfbDb(PSMA). Data represent the mean \pm SD of triplicate determinations.

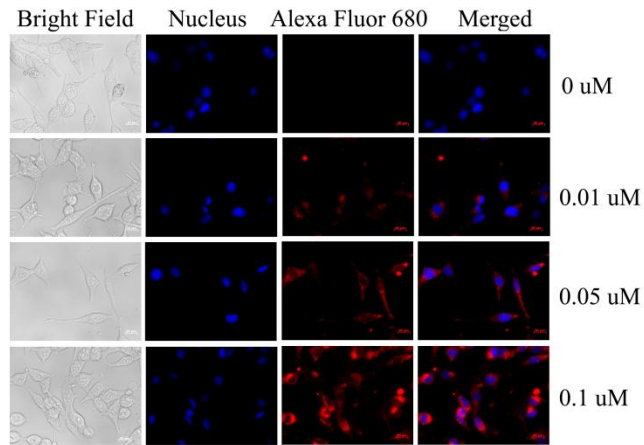


Figure 4. Fluorescence microscopy of A-dmDT90(390)-scfbDb(PSMA) internalization in LNCaP cells. Cells were treated with 0.01, 0.05 or 0.1 μ M of Alexa Fluor 680 -labeled A-dmDT90(390)-scfbDb(PSMA) for 3 hours. After washing with DPBS, cells were fixed and incubated with DAPI, and observed under a fluorescence microscope (magnification 400 \times).

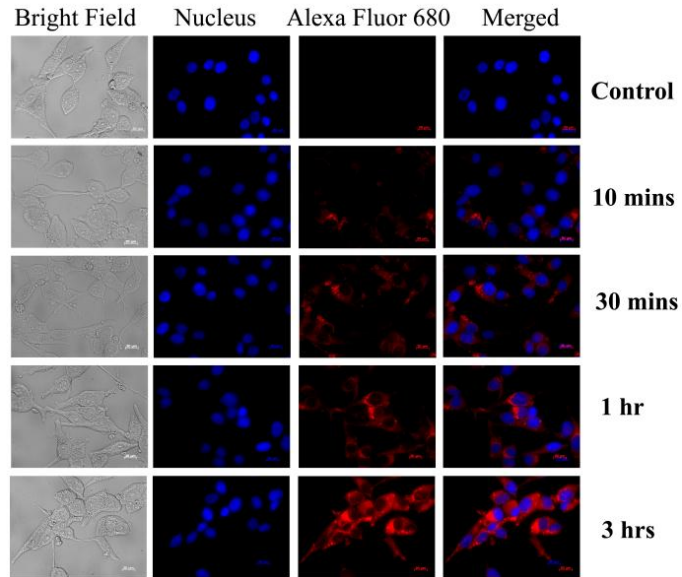


Figure 5. Fluorescence microscopy of the time course of A-dmDT90(390)-scfbDb(PSMA) internalization in LNCaP cells. Cells were treated with 0.1 μ M of Alexa Fluor 680 -labeled A-dmDT90(390)-scfbDb(PSMA) for different duration, *i.e.*, 10 min, 30 min, 1 h and 3 h . After washing with DPBS, cells were fixed and incubated with DAPI, and observed under fluorescence microscope (magnification 400 \times).

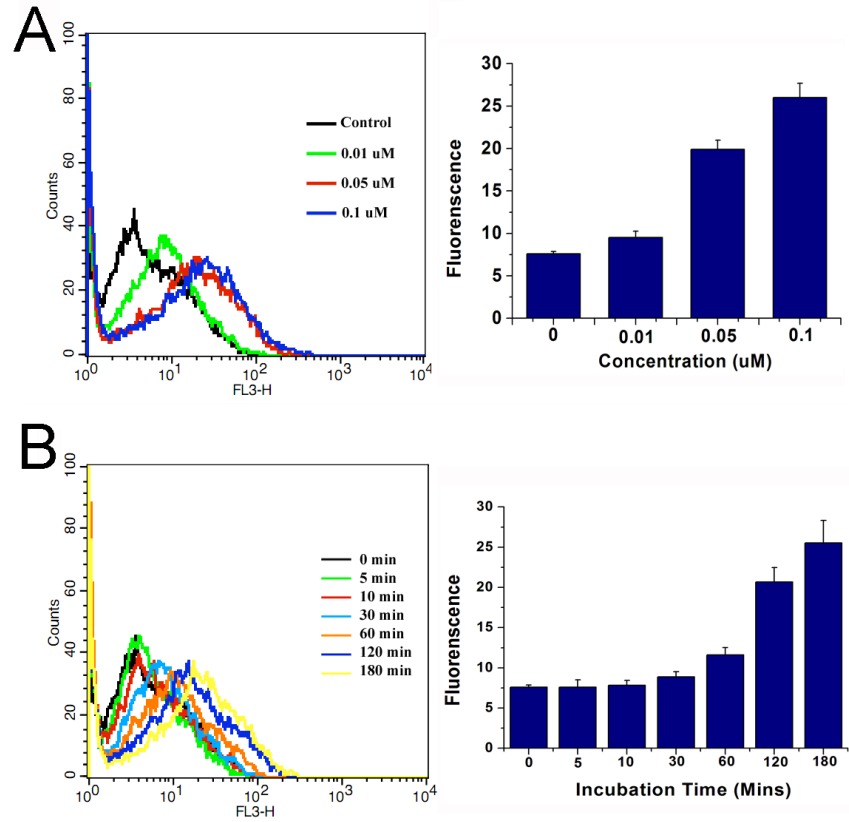


Figure 6. Flow cytometry quantification of A-dmDT90(390)-scfbDb(PSMA) accumulation in LNCaP cells. Cells were treated with 0.01, 0.05 or 0.1 μ M of Alexa Fluor 680 -labeled A-dmDT90(390)-scfbDb(PSMA) for 3 hours (A) or with 0.1 μ M of Alexa Fluor 680 -labeled A-dmDT90(390)-scfbDb(PSMA) for different duration, *i.e.*, 5, 10, 30, 60, 120 and 180 min (B). After washing with DPBS, cells were collected and analyzed by flow cytometry.

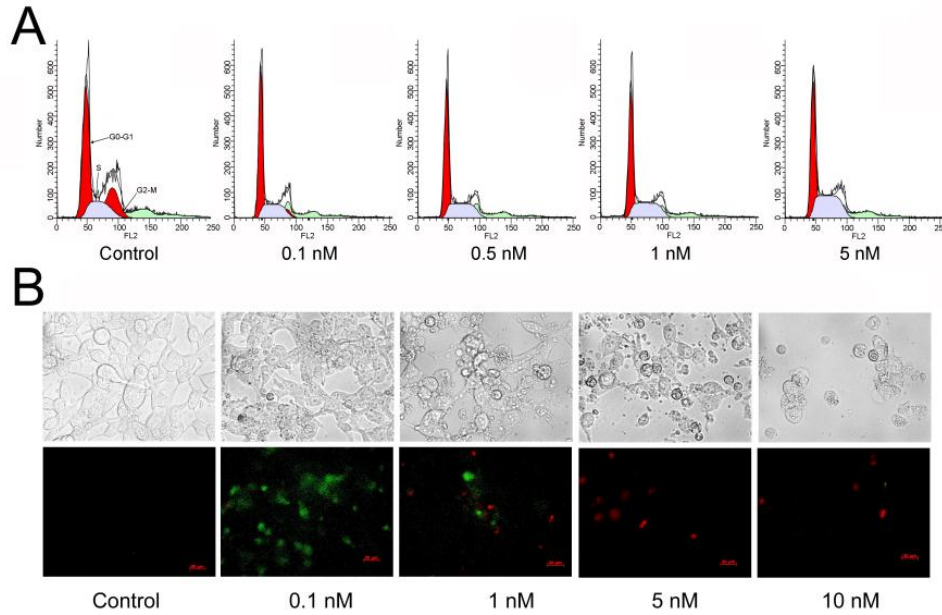


Figure 7. Cell cycle analysis and Apoptosis assay of LNCaP cells after A-dmDT90(390)-scfbDb(PSMA) treatment. (A) LNCaP cells were treated with 0.1, 0.5, 1 and 5 nM of A-dmDT90(390)-scfbDb(PSMA) for 24 hours, then stained with PI. Cell cycle distributions were analyzed with flow cytometry. (B) LNCaP cells treated with 0 to 10 nM of A-dmDT90(390)-scfbDb(PSMA) for 48 hours were stained using Annexin V-FITC antibody and washed with buffer and observed under a fluorescent microscope (magnification $400\times$).

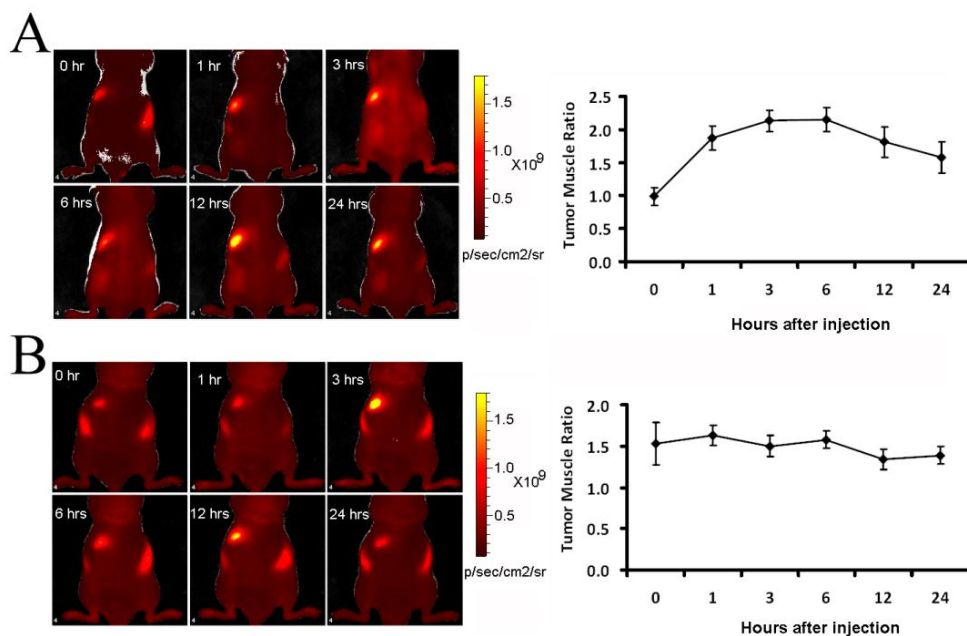


Figure 8. Whole-animal imaging following intravenous injection of Alexa Fluor 680 -labeled A-dmDT90(390)-scfbDb(PSMA) into LNCaP tumor bearing mice showing preferential accumulation of fluorescent signals in tumors. (A) Images obtained after injection of Alexa Fluor 680 -labeled A-dmDT90(390)-scfbDb(PSMA) (100 μl) into mice. (B) Images obtained after injection of Alexa Fluor 680 dye (100 μl) into mice. Images were taken at 0, 1, 3, 6, 12 and 24 hours, separately. The chart on the right shows change in the tumor to muscle ratio of fluorescence intensities over time.

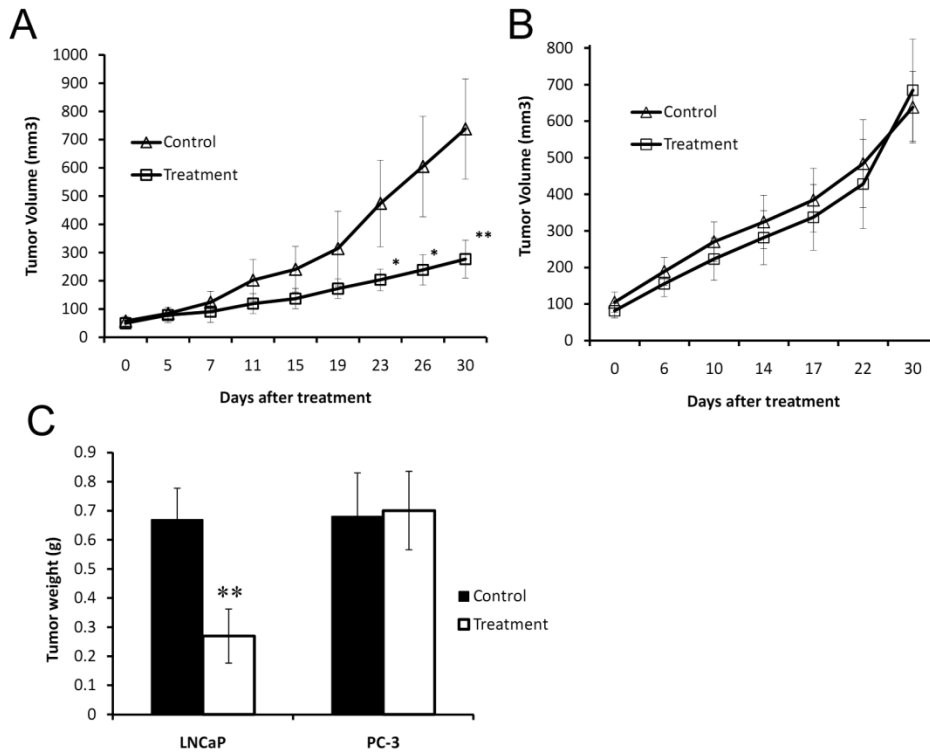


Figure 9. Effect of A-dmDT90(390)-scfbDb(PSMA) immunotoxin on LNCaP and PC-3 prostate carcinomas. 5 $\mu\text{g}/\text{mice}$ per dose of A-dmDT90(390)-scfbDb(PSMA) immunotoxin was given via intraperitoneal injection, two doses a day with 6 hour interval for 6 days, compared to equivalent dose of BSA diluted in DPBS ($n = 10$ mice per group, $*p < 0.1$, $**p < 0.01$). (A) LNCaP tumor volume measurement by MRI. (B) PC-3 tumor volume measurement by MRI. (C) Tumor weight at 30 days after treatment.

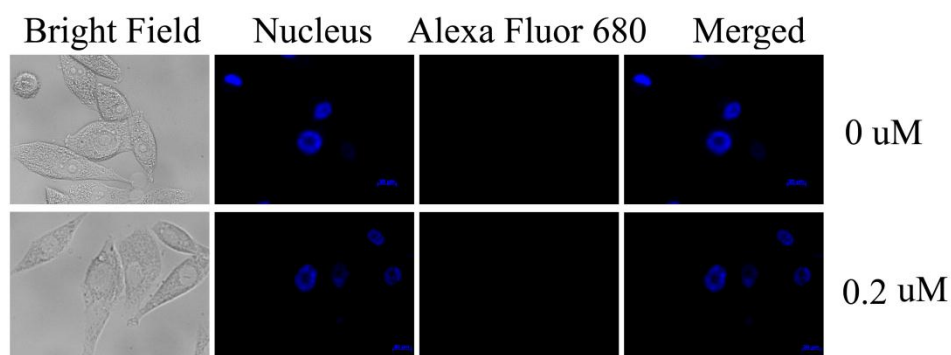


Figure S1. Fluorescence microscopy of A-dmDT90(390)-scfbDb(PSMA) internalization in PC-3 cells. Cells were treated with 0.2 μ M of Alexa Fluor 680 -labeled A-dmDT90(390)-scfbDb(PSMA) for 4 h. After washing with DPBS, cells were fixed and incubated with DAPI, and observed under fluorescence microscope (magnification 1000 \times).

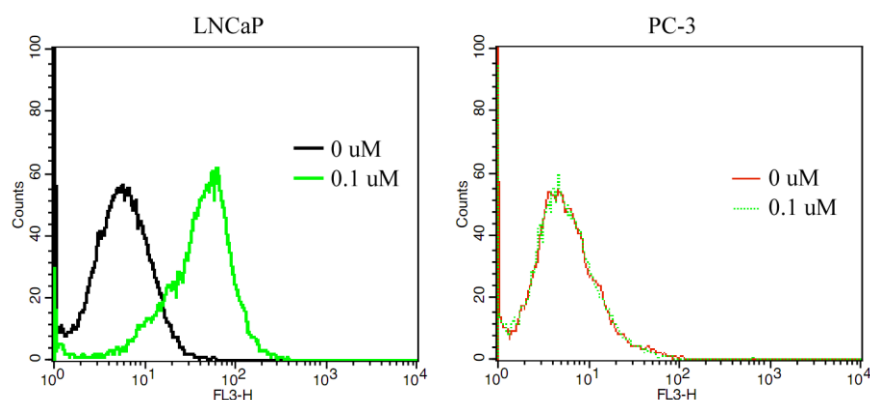


Figure S2. Flow cytometry quantification of A-dmDT90(390)-scfbDb(PSMA) accumulation in PC-3 and LNCaP cells. Cells were treated with 0.1 μ M of Alexa Fluor 680 -labeled A-dmDT90(390)-scfbDb(PSMA) for 6 hours. After washing with DPBS, cells were collected and analyzed by flow cytometry.

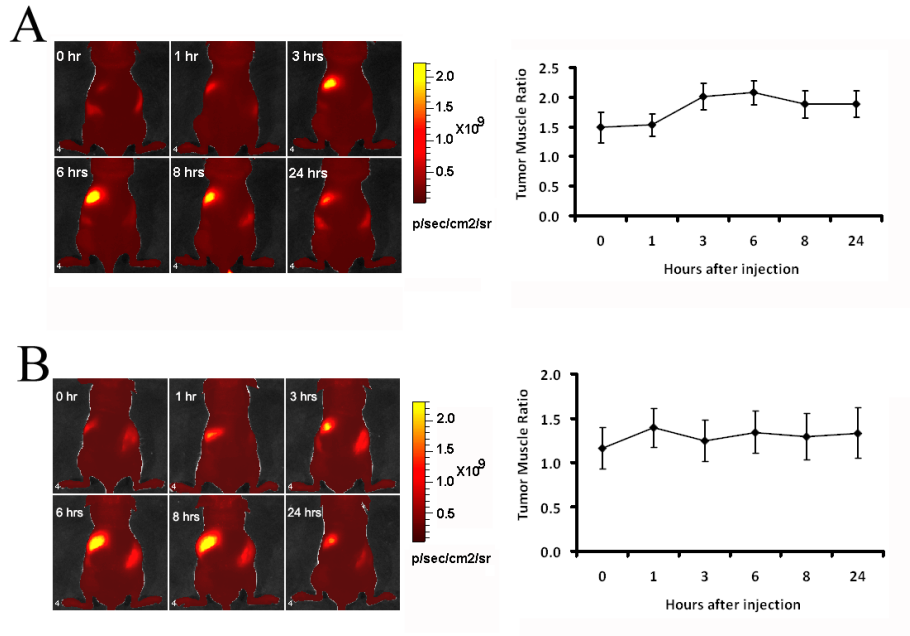


Figure S3. Whole-animal imaging following intravenous injection of Alexa Fluor 680 –labeled A-dmDT90(390)-scfbDb(PSMA) into PC-3 tumor bearing mice. (A) Images were acquired after injection of Alexa Fluor 680 -labeled A-dmDT90(390)-scfbDb(PSMA) (100 μl) into mice. (B) Images were acquired after injection of Alexa Fluor 680 dye (100 μl) into mice. Images were taken at 0, 1, 3, 6, 8 and 24 hours, separately. The chart on the right shows change in the ratio of tumor to muscle fluorescence intensities over time.